Curso 2012/13
CIENCIAS Y TECNOLOGÍAS/13
I.S.B.N.: 978-84-15910-71-8

AMADA LORENA MONTESDEOCA SANTANA

Texturization processes of monocrystalline silicon with Na2CO3/NaHCO3 solutions for solar cells

Directores
RICARDO L. GUERRERO LEMUS
DIETMAR BORCHERT

SOPORTES AUDIOVISUALES E INFORMÁTICOS
Serie Tesis Doctorales

A mi familia

Contents

1 Introduction ... 1
1.1 Motivation ... 1
1.2 Thesis outline ... 3
2 Solar cell principles ... 5
2.1 Brief introduction ... 5
2.2 The p-n junction under dark conditions ... 6
2.3 The p-n junction under illumination conditions ... 8
2.4 Current-Voltage characteristic ... 8
2.5 Quantum efficiency ... 11
2.6 Recombination in solar cells ... 12
3 Fundamentals of silicon texturization ... 17
3.1 Introduction ... 17
3.2 Optical benefits of textured silicon ... 18
3.3 Silicon texturization techniques ... 23
3.3.1 Dry etching processes ... 23
3.3.2 Wet chemical processes ... 25
3.4 Anisotropic etching of silicon ... 27
3.5 Previous work on $Na_2CO_3/NaHCO_3$ texturization ... 30
4 Experimental methods ... 33
4.1 Production processes ... 33
4.1.1 Texturization process ... 33
4.1.2 Solar cell processing ... 35
4.2 Characterization techniques ... 43
4.2.1 Materials characterization ... 43
4.2.2 Solar cell characterization ... 51
5 Optimization of the $Na_2CO_3/NaHCO_3$ process for texturization of (100) silicon ... 53
5.1 Influence of chemicals concentration. Towards an ultra-low concentration $Na_2CO_3/NaHCO_3$ solution for silicon texturization. ... 53
5.2 Influence of the initial surface roughness of the silicon wafers ... 59
5.3 Temperature dependency and activation energy of the silicon texturization ... 64

5.4 Scale-up of the process ... 65
5.5 Conclusions ... 67
6 Microscopic analysis of pyramid formation and its mechanism ... 69
6.1 Literature survey on the mechanism of pyramidal formation by alkaline solutions ... 69
6.2 SEM analysis of pyramidal formation ... 71
6.2.1 SEM analysis on different wafers treated at different texturization times ... 71
6.2.2 SEM analysis on multiple-step textured sample ... 76
6.3 AFM analysis of pyramidal formation ... 79
6.3.1 AFM analysis on different wafers treated at different texturization times ... 79
6.3.2 AFM analysis on multiple-step textured wafer ... 80
6.4 Conclusions ... 83
7 Na_2CO_3/$NaHCO_3$ textured solar cells. Influence of the textured surface on solar cell parameters ... 85
7.1 Influence of Na_2CO_3/$NaHCO_3$ texturization on surface recombination ... 85
7.2 Deposition of layers and emitter formation on textured surfaces. Influence of Na_2CO_3/$NaHCO_3$ textured surfaces on solar cell processing ... 89
7.2.1 Emitter formation ... 89
7.2.2 SiN_x deposition ... 93
7.2.3 a-Si:H deposition ... 94
7.3 Ultra-low concentration Na_2CO_3/$NaHCO_3$ textured solar cells ... 96
7.4 Conclusions ... 104
8 Summary and conclusions ... 107
Resumen y conclusiones ... 111
References ... 115
List of symbols and abbreviations ... 127
List of peer-reviewed publications ... 131
Agradecimientos / Danksagung ... 133

1 Introduction

1.1 Motivation

The need to fulfil the growing demand of energy in our planet and to use clean energy sources in order to mitigate the global warming caused by the emission of greenhouse gases due to fossil fuel consumption [1], have allowed the development of various systems that exploit the renewable energy sources over the past decades. Among these renewable sources, solar energy, in particular its direct conversion into electricity through the photovoltaic effect has experienced an important growth. Photovoltaic (PV) energy is the third most important renewable energy for electricity production after hydropower and wind power, having a total cumulative installed capacity over 69 GW worldwide [2]. In Europe, PV supplies 2 % of the electricity demand, with an installed total capacity of 51 GW [2]. The target aimed by the European Union is to reach a renewable energy share of 20 % by 2020, producing 12 % of the electricity by PV [3]. The prices of PV systems have experienced a strong decrease (an EPIA report from 2011 estimated 50 % decrease in prices over the period of the previous five years) [4]. The cost per kWh of PV energy is expected to decrease by a 50 % until 2020 from its price in 2010 [4]. These facts together with the increasing costs of conventional electricity make possible a scenario in which PV would be competitive in Europe before 2020 [4].

To achieve these objectives, efforts are primarily aimed at making efficient photovoltaic modules at lower cost, since a big part of the cost of photovoltaic energy is given by the price of the module. Therefore, in solar cell manufacturing research, increasing efficiency and reducing production costs are the two main engines that drive it nowadays. Some authors [5] point to the greater importance of reducing costs against the efficiency gains, given the evolution of the technology, and going deeply into fundamental research related to manufacturing on an industrial scale.

Among the different types and concepts of solar cells that can be found, those based on crystalline silicon dominate over 85 % of the market in 2010 [3] due to the state of development they have achieved and the abundance of this material. Currently the production of crystalline silicon based cells, a technology which is able to deliver the efficiencies demanded by the market, is still predominant. Although there is a large increase in the development of thin film technology because of its lower cost, it is expected that crystalline silicon-based technology (which holds records in efficiency and is widely deployed in the industry) remains the dominant sector. Furthermore, the price decrease of the polysilicon during the last few years has supported this prevalence [6].

Because of the previously exposed facts, the potential development of crystalline silicon technology is not yet exhausted and increasing efficiency and decreasing costs is necessary to achieve the objectives.

Within the wafer-based manufacturing technology, basic steps are the elimination of surface saw damage defects and texturing of the substrate [7]. These processes have further potential to be optimized in order to improve cell efficiencies and reduce costs. The elimination of saw damage is important as these defects, generated by cutting the wafers, lead to recombination of photogenerated charge carriers. By means of chemical processes, the first microns of the wafer surface are eliminated, and with them these surface defects. Texturing, on the other hand, is important to decrease the front reflectance of the cell and to improve the light trapping in order to increase the generated current. Depending on the used process, the texturization can also contribute to the elimination of saw defects by simultaneously etching the first layers of the silicon wafer. These texturization processes are applied to the silicon wafers used in manufacturing conventional diffused solar cells, as well as to heterojunction solar cells with amorphous silicon emitter.

In a recently published review article about the status of the photovoltaic industry, the "advanced photon management" was proposed as an area of research investment. In this research area we might include texturing silicon substrates [5], since it aims to increase the proportion of absorbed photons impinging on the cell. Texturization processes aimed to enhance light trapping become more important as the thickness of the wafers used in solar cell production decreases in order to save silicon. In thin wafers, long wavelength photons pass through the wafer without being absorbed. Light trapping schemes are able to increase the length of the optical path of these photons increasing their possibilities of being absorbed. The minimum as cut wafer thickness used in the industry at the end of 2011 was 180 μm, being predicted a further decrease to 120 μm in 2020 [6].

Among the several techniques employed for silicon texturization, wet chemical texturization is the most extended in the industry. Alkaline (e.g. NaOH or KOH aqueous solutions with added isopropanol) and acidic solutions (e.g. HF/HNO_3 mixtures) are used for this purpose. Alkaline texturization systems produce micrometric pyramids on the surface of (100) silicon due to its anisotropic character. The formed pyramids decrease the front reflection and enhance light trapping.

This thesis is aimed at the study of single crystal silicon texturing with $Na_2CO_3/NaHCO_3$ aqueous solution, an alkaline texturization system. Alkaline solutions are more environmentally friendly than acidic solutions from the point of view of generated wastes [8]. In addition, compounds used for texturing silicon with acidic solutions such as HF or HNO_3 also have certain disadvantages with respect to the safety at work [7]. HF is toxic, and both HF and HNO_3 are irritating and corrosive [7]. If we consider the use of solutions based on $Na_2CO_3/NaHCO_3$, compared to other alkaline solutions as NaOH or KOH-based, texturing with $Na_2CO_3/NaHCO_3$ has the advantage

of requiring no additives such as isopropanol (IPA), which saves not only costs but waste [9, 10]. However, the concentration of the reactants of the $Na_2CO_3/NaHCO_3$ solutions described in the literature [10] is high compared to standard NaOH and KOH solutions, and the process should be optimized in order to be implemented at industrial level.

The objective of this thesis is to study in depth the anisotropic $Na_2CO_3/NaHCO_3$ texturization system through three main targets: (i) study of the process parameters and definition of an optimum process with potential to be industrially implemented; (ii) study of the evolution of surface morphology by the action of the $Na_2CO_3/NaHCO_3$ solution and determination of the mechanism of pyramid formation for a better understanding of the process; (iii) study of the influence of the $Na_2CO_3/NaHCO_3$ textured morphology on different solar cell processing steps and analysis and characterization of $Na_2CO_3/NaHCO_3$ textured silicon crystalline solar cells.

1.2 Thesis outline

The basic principles of crystalline silicon solar cells are described in **chapter 2**, the generation of electron-hole pairs in semiconductor materials by photon absorption, and the fundamentals of p-n junction and the current-voltage characteristic of solar cells are briefly exposed.

Chapter 3 constitutes a review about fundamentals of silicon texturization. The optical benefits of textured surfaces are explained and the main techniques for silicon texturization are listed and described. The theories about the chemical reaction mechanism of anisotropic etching existing in the bibliography are reviewed. Also the previous works about silicon texturization with $Na_2CO_3/NaHCO_3$ solutions which can be found in the literature are summarized.

The experimental methods used in this thesis are summarized in **chapter 4**. The laboratory texturization process and the processes employed to produce the solar cells, as well as the characterization techniques used for materials and solar cell analysis are described.

In **chapter 5**, the results of the study of the parameters influencing silicon texturization with $Na_2CO_3/NaHCO_3$ solutions are presented. The problems derived from silicon texturization with the high concentration solutions of $Na_2CO_3/NaHCO_3$ encountered in the literature are exposed, and a novel ultra-low concentration $Na_2CO_3/NaHCO_3$ solution for anisotropic texturization of silicon is proposed and studied from the operation and resulting surface morphology and characteristics points of view.

Chapter 6 aims to contribute to the better understanding of the microstructuring of (100) silicon surfaces to pyramidal morphology by alkaline etching solutions. A bibliographic review about the topic is presented. The mechanism of pyramidal

formation and the evolution of the structures formed with $Na_2CO_3/NaHCO_3$ solutions is analysed and discussed in comparison with the bibliography.

In **chapter 7**, the $Na_2CO_3/NaHCO_3$ anisotropic etching is introduced as texturization step in a crystalline silicon solar cell production process. The influence of the textured surface, especially, the surface resulting from the novel proposed ultra-low concentration $Na_2CO_3/NaHCO_3$ texturization method on different solar cell processing steps as emitter formation or deposition of passivating and antireflecting layers is studied. Solar cells with the new ultra-low $Na_2CO_3/NaHCO_3$ and the high concentration $Na_2CO_3/NaHCO_3$ texturizations are produced, analysed and compared in order to prove the feasibility of the novel proposed ultra-low concentration $Na_2CO_3/NaHCO_3$ texturization process.

Finally, the main conclusions of this work are summarized in **chapter 8**.

2 Solar cell principles

2.1 Brief introduction

When a semiconductor material absorbs a photon of certain energy E higher than its bandgap energy (E_g), an electron-hole pair is generated. This is the photovoltaic effect. In the case of silicon, as it is an indirect semiconductor, the process consisting of the excitation of an electron to the conduction band leaving a hole in the valence band is assisted by phonons to ensure momentum conservation (Figure 2.1).

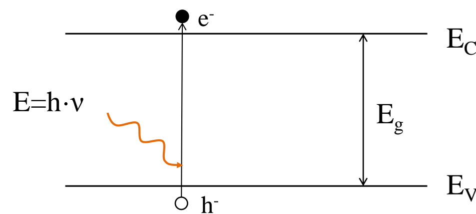

Figure 2.1. Electron-hole pair photogeneration.

In opposition to this generation, there exists the process called *recombination*, which can be produced not only by radiative process but by some other mechanisms as well, which will be discussed in Section 2.6. Before the electrons and holes recombine in a semiconductor they diffuse through the semiconductor. The characteristic parameters for this diffusion process are the *lifetime* τ, i.e. the time between the generation and the recombination of the electron-hole pair; and the *diffusion length* L_D, i.e. the distance between the points of generation and recombination within the semiconductor.

The operating principle of crystalline solar cells lies in the p-n junction, i.e. the junction of a p-type doped semiconductor with an n-doped semiconductor, which generates an electrical field that enables the charge carriers photoconverted in the semiconductor to be collected by the metallic contacts as electrical current. The basic scheme of a crystalline solar cell is depicted in Figure 2.2.

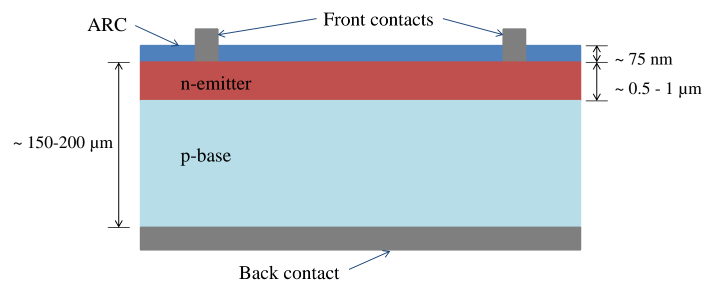

Figure 2.2. Basic scheme of a crystalline solar cell with a p-Si base and a diffused n-emitter on the front side.

The aim of this chapter is to give a general overview of solar cell physic principles. Deeper explanations and details can be found in the literature [11, 12].

2.2 The p-n junction under dark conditions

In the p-n junction, the majority charge carriers from both doped sides (holes in the p-region and electrons in the n-region) diffuse from the high concentration area to the low concentration area. The holes from the p-region diffuse towards the n-region and the electrons from the n-region diffuse towards the p-region leaving ionized the acceptor and donor atoms as fix charges, which built up an electrical field in opposite direction to the diffusion current. At equilibrium, the diffusion and the field current are compensated. The transition region between the p- and n- type regions is the called space charge region or depletion region. On both sides of the space charge region the p- and n- semiconductor remains *quasi-neutral*.

The Fermi level (E_F) of p and n-region equals at thermal equilibrium. This produces a band bending of conduction and valence band-edge energies (E_C and E_V), and a potential difference called built-in voltage or diffusion voltage (V_D), as represented in Figure 2.3.

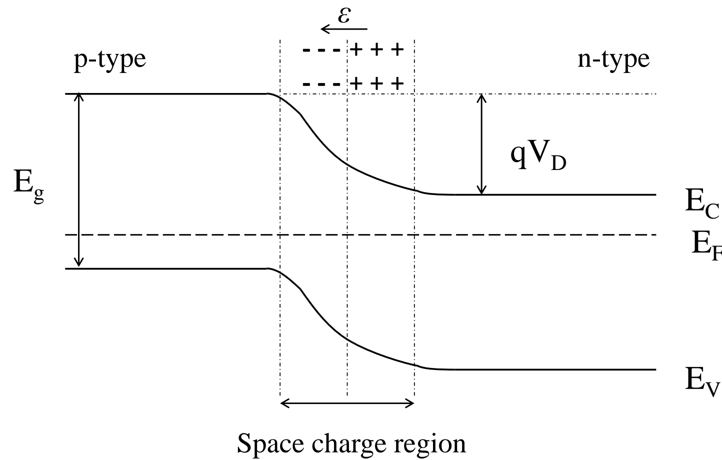

Figure 2.3. Energy band structure of the p-n junction, where q is the elementary electron charge and ε the electrical field.

The diffusion voltage is given by the band gap energy of the semiconductor (E_g) and the acceptor and donor concentrations (N_A and N_D) in p- and n-regions, and can be expressed as follows:

$$V_D = \frac{kT}{q} \ln \frac{N_A N_D}{n_i^2} \tag{2.1}$$

where k is the Boltzmann constant, T is the temperature and n_i is the intrinsic carrier density.

At thermal equilibrium generation and recombination are compensated. The intrinsic carrier density is:

$$n_i^2 = np = N_c N_V exp\left(-E_g/kT\right) \tag{2.2}$$

N_C and N_V are the effective density of states in the conduction and valence bands respectively.

The p-n junction is a diode. The current density in the diode is the sum of the hole current density J_p plus the electron current density J_n.

$$J_{total} = J_p + J_n \tag{2.3}$$

After some considerations that can be found elsewhere [11], the hole and electron current density can be expressed as:

$$J_\mathrm{p} = \frac{qD_p n_i^2}{L_p N_D}\left(exp\frac{qV}{kT} - 1\right) \tag{2.4}$$

$$J_\mathrm{n} = \frac{qD_n n_i^2}{L_n N_A}\left(exp\frac{qV}{kT} - 1\right) \tag{2.5}$$

The current-voltage characteristics of the p-n junction in the dark and with an applied voltage V can be described thus as follows:

$$J = \left(\frac{qD_p n_i^2}{L_p N_D} + \frac{qD_n n_i^2}{L_n N_A}\right)\left(exp\frac{qV}{kT} - 1\right) = J_0\left(exp\frac{qV}{kT} - 1\right) \tag{2.6}$$

This is the diode equation, where J_0 is the saturation current density:

$$J_0 = \left(\frac{qD_p n_i^2}{L_p N_D} + \frac{qD_n n_i^2}{L_n N_A}\right) \tag{2.7}$$

D_n and D_p are the diffusion coefficient of electrons and holes respectively, and L_p and L_n the diffusion lengths of holes and electrons.

$$L_p = \sqrt{D_p \tau_p} \tag{2.8}$$

$$L_n = \sqrt{D_n \tau_n} \tag{2.9}$$

τ_p and τ_n are the lifetime of holes and electrons, respectively.

2.3 The p-n junction under illumination conditions

Under illumination, electron-hole pairs are generated with a generation rate *G*. The current density corresponding to the generation of carriers is the illumination current density J_L. The charge carriers are generated in the p-region, the n-region and in the space charge region. Only the charge carriers generated at the space charge region or at a distance to the space charge region equal or smaller than their corresponding diffusion length contribute to it.

$$J_L = qG\left(L_n + L_p + w\right) \tag{2.10}$$

where *w* is the space charge region width.

Then, the current density in the solar cell can be expressed as follows:

$$J = J_0\left(exp\frac{qV}{kT} - 1\right) - J_L \tag{2.11}$$

To obtain the expressions exposed above a constant illumination in the crystal has been considered and recombination in the space charge region disregarded [11].

2.4 Current-Voltage characteristic

The current-voltage curve of a solar cell under dark and illumination conditions is shown in Figure 2.4.

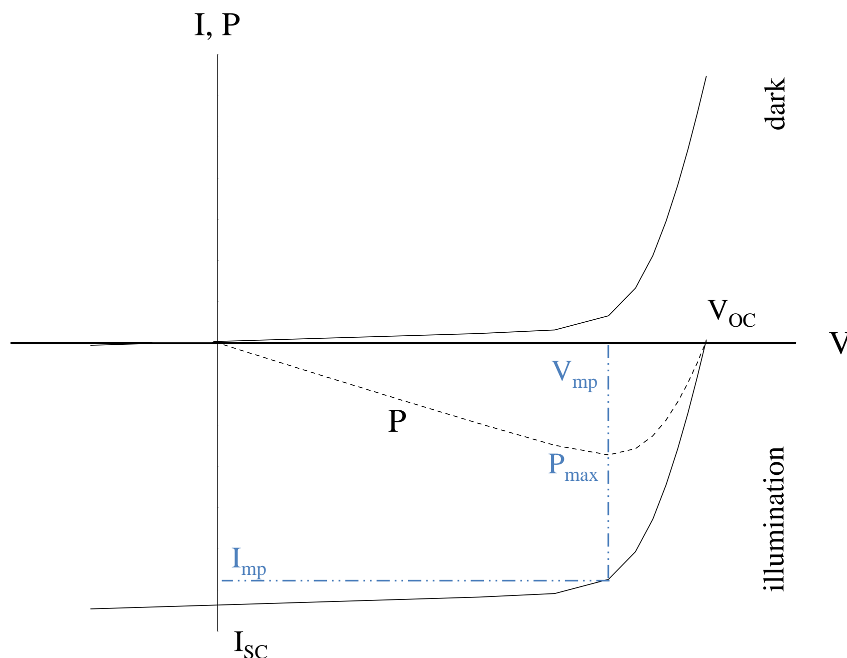

Figure 2.4. I-V curve of a solar cell in dark and illumination conditions and power-voltage (P-V) curve.

Under illumination the generated current appears opposed to the saturation current of the diode. The analysis of the current-voltage curve measured in standard conditions[1] leads to the characteristic parameters of a solar cell:

- Short circuit current I_{SC}: it is the current at short-circuit conditions, i.e. at zero voltage. The short circuit current corresponds to the illumination current I_L in an ideal case, following Equation 2.11.

- Open circuit voltage V_{OC}: it is the voltage obtained when no current flows in the solar cell and it can be expressed as follows by setting the current density in Equation 2.11 to zero:

$$V_{OC} = \frac{kT}{q} ln\left(\frac{J_L}{J_0} + 1\right) \quad (2.12)$$

  Assuming $J_L/J_0 >> 1$ and $J_L \approx J_{SC}$ the expression for V_{OC} can be simplified to:

$$V_{OC} = \frac{kT}{q} ln\left(\frac{J_{SC}}{J_0}\right) \quad (2.13)$$

  which shows the role of saturation current in solar cells. This parameter should be reduced in order to obtain high V_{OC}.

- Maximum power point: it is the point of the curve where the power, i.e. the product of current and voltage $P = IV$ reaches its maximum value. At this point I_{mp} and V_{mp} are the corresponding current and voltage values.

- Fill factor FF: the fill factor is defined as the ratio between the maximum power and the product $I_{SC} \cdot V_{OC}$.

$$FF = \frac{I_{mp}V_{mp}}{I_{SC}V_{OC}} \quad (2.14)$$

- Efficiency Eff: the efficiency is the relation between of the photoconversion power obtained and the incident light power P_i.

$$Eff = \frac{I_{mp}V_{mp}}{P_i} = \frac{FF\ I_{SC}V_{OC}}{P_i} \quad (2.15)$$

In real solar cells other factors that influence the characteristic *I-V* curve should be taken into account, as the ohmic resistances and the current corresponding to the recombination in the space charge region.

[1] i. e. under AM1.5G illumination at 25°C.

The ohmic resistances of the solar cell are a series resistance and a parallel resistance. The series resistance R_S is given by the ohmic resistance between the metallization and the semiconductor, and the semiconductor and the contact resistivities. The parallel or shunt resistance R_P corresponds to the current lost at the edges of the cell or defects or inhomogeneities in the p-n junction.

The current corresponding to recombination in the space charge region J_r, after some considerations and taking into account Schockley-Read-Hall recombination [13] via impurity level placed at the middle of the ban-gap, can be expressed as:

$$J_r = \frac{kT\pi n_i}{\tau_0 \varepsilon_{max}} exp\left(\frac{qV}{2kT}\right) \tag{2.16}$$

where ε_{max} is the electric field at the p-n junction and τ_0 the lifetime of electrons and holes which are assumed as equal [11].

The term $\frac{kT\pi n_i}{\tau_0 \varepsilon_{max}}$ is called J_{02} and is added to the diode equation, resulting in:

$$J = J_{01}\exp\left(\frac{qV}{kT}\right) + J_{02}exp\left(\frac{qV}{2kT}\right) \tag{2.17}$$

where J_{01} is equivalent to the already mentioned before saturation current density J_0.

Figure 2.5 shows the equivalent electrical circuit diagram of a solar cell following the two diode model.

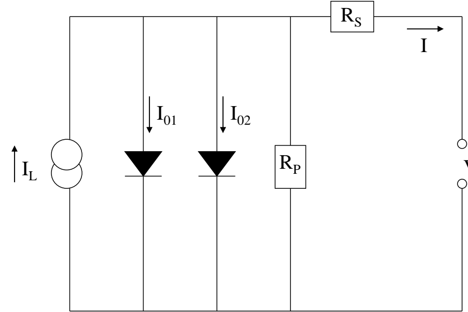

Figure 2.5. Equivalent circuit diagram of a solar cell.

The illuminated solar cell behaviour can thus be modelled as an electrical equivalent circuit that follows the relation:

$$I(V,I) = I_{01}\left(exp\frac{V - IR_S}{n_1\, kT/q} - 1\right) + I_{02}\left(exp\frac{V - IR_S}{n_2\, kT/q} - 1\right) + \frac{V - IR_S}{R_P} - I_L \tag{2.18}$$

This is the *two diode* model. n_1 and n_2 are the ideality factor and correspond to the values 1 and 2 from the theory, but in real solar cells can slightly deviate from these values.

2.5 Quantum efficiency

Solar cells can be also characterized through their external quantum efficiency *EQE* as a function of the wavelength of the incident light. The *EQE* is defined as the ratio of electrons collected per incident photon. The *EQE* is related to the short circuit current density of the solar cell:

$$J_{sc} = q\int_0^{\infty} EQE\,(\lambda)SE(\lambda)d\lambda \qquad (2.19)$$

where $SE(\lambda)$ is the solar spectrum intensity.

If the effect of the front reflectance *R* is subtracted, the internal quantum efficiency *IQE* can be defined:

$$IQE(\lambda) = \frac{EQE(\lambda)}{1 - R(\lambda)} \qquad (2.20)$$

From Equations 2.19 and 2.20 it can be understood that given an internal quantum efficiency (determined by the quality of the base material and its surface, the p-n junction and the metallization), a decrease in the front reflection is important in order to have a higher *EQE* and therefore a higher J_{sc} and higher efficiency.

Figure 2.6 shows the *EQE* and *IQE* measured on a real solar cell. The interpretation of the *EQE* and *IQE* curves can give useful information about the different parts of a solar cell and help to identify problems. Short wavelength photons are absorbed within the first micrometres of the solar cell. Thus the *IQE* at these short wavelengths can give information about front surface and emitter recombination or absorption on the front layers. The highest *IQE* in silicon diffused solar cells is in the range of approximately 500 to 850 nm wavelength, corresponding to the silicon bulk crystal, where the carriers are not so affected by recombination processes. There, the quality of the base material is reflected. The long wavelength photons are absorbed at the back side of the solar cell. The *IQE* could give in this case information about back surface recombination and back internal reflection.

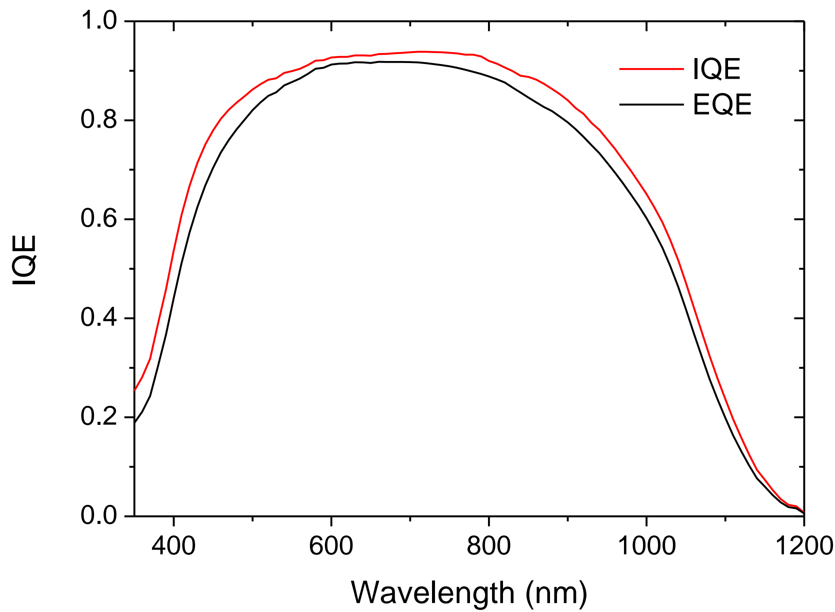

Figure 2.6. EQE and IQE curves of a real solar cell.

2.6 Recombination in solar cells

Contrary to generation, recombination is the relaxation of electrons from conduction to valence band, and emitting the excess energy as photons or phonons. The recombination processes affects negatively the obtained current, and the voltage of the cell, which will decrease the final efficiency. Therefore recombination should be avoided or mitigated.

The recombination rate U is defined as follows:

$$U = \frac{\Delta n}{\tau} \tag{2.21}$$

where Δn is the excess electron density and τ their lifetime. Assuming no carrier trapping (non-recombinative traps for electrons or holes), the excess concentrations of electrons (Δn) and holes (Δp) are equal.

A high recombination rate or low lifetime would decrease the diffusion length of the carriers, and this would increase the saturation current density J_0 (see Equation 2.7) and therefore the voltage would be diminished (Equation 2.13).

There are different recombination mechanisms depending on how the excess energy is released. The recombination mechanisms (Figure 2.7) are the following:

- Radiative or direct recombination
- Auger recombination
- Shockley-Read-Hall (SRH) recombination

The effective lifetime τ_{eff} of the carriers is the result of the three mechanisms:

$$\frac{1}{\tau_{eff}} = \frac{1}{\tau_{Rad}} + \frac{1}{\tau_{Auger}} + \frac{1}{\tau_{SRH}} \tag{2.22}$$

These mechanisms are shortly explained here, but their fundamentals are described in more detail in the literature [14].

Radiative recombination

In the radiative recombination process an electron from the conduction band relaxes to an unoccupied state level in the valence band, emitting a photon with energy near the bandgap energy. While this process is of crucial importance in direct semiconductors, in silicon it has a small effect, as a phonon should assist the process, decreasing its occurrence probability.

Auger recombination

The energy released by the electron relaxation is in this recombination mechanism transferred to another charge carrier, which returns to its initial energy state by emitting phonons. Auger lifetime depends on the doping level of the wafers and the injection level. An increase in the doping concentration or the injection level decreases the Auger lifetime.

Shockley-Read-Hall recombination

Existing impurities, dislocations and defects in silicon induce energy states within the bandgap. In the description of the Shockley-Read-Hall recombination [13] an electron from the conduction band can decay to this defect induced energy states, and from there to the valence band to recombine with a hole in two steps, releasing energy as phonons.

In solar cells the Shockley-Read-Hall recombination centres are produced by defects and impurities in the bulk and in the silicon surface where dangling bonds or chemical residues and particles from processing generate surface states within the bandgap. The SRH recombination is proportional to the defect density.

In the case of the surface, the density of defects generates a continuum of surface states within the bandgap. The surface recombination is expressed rather as surface recombination velocity. The surface recombination velocity at the semiconductor surface is defined as follows:

$$S = \frac{\Delta n_S}{U_s} \tag{2.23}$$

where Δn_s is the excess carrier concentration at the surface and U_s is the surface recombination rate per unit area.

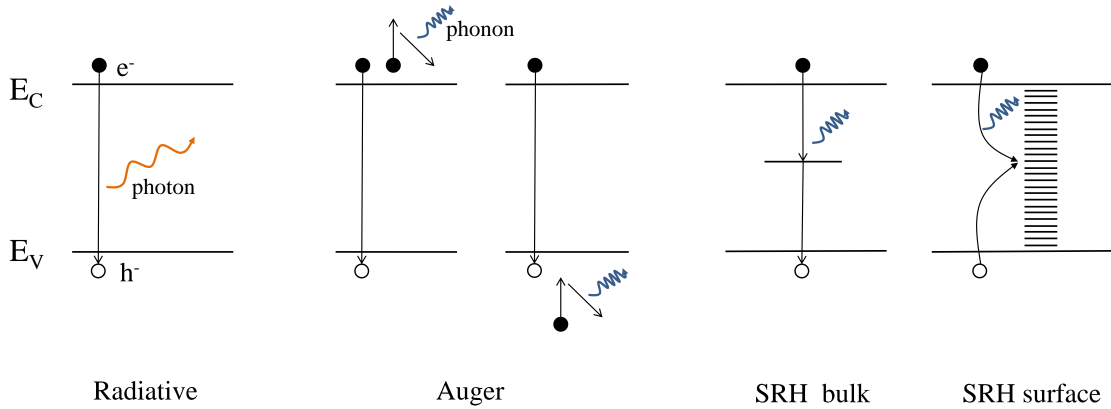

Figure 2.7. Recombination mechanisms in silicon.

Recombination reduction: passivation and gettering

Silicon passivation aims to mitigate the carrier recombination that takes place in the silicon bulk and silicon surface.

Surface passivation can be achieved through two different technological strategies: surface state density reduction and surface carrier concentration reduction.

The recombination rate is proportional to the density of surface states; therefore reducing the state density can enhance the lifetime. For this, despite of avoiding surface damage and particle and impurity contamination during the processing of solar cells, and performing exhaustive cleanings of the wafers, passivation layers are used. Examples of passivation layers are silicon nitride, silicon oxide [14], or amorphous silicon [15]. Chemical surface passivation by saturation of the dangling bonds with atoms like hydrogen or oxygen can also be done with wet chemical solutions. One example is the -H termination that results from silicon immersions in HF or NH_4F, or the wet chemical growth of silicon oxide [16, 17].

The reduction of the carrier concentration at the silicon surface decreases the surface recombination, as at equal concentration of electron and holes the recombination reaches its highest rates. In order to achieve a reduction of carrier concentration, an internal electrical field under the surface can be induced. To introduce a field effect there exist two options:

(i) The creation of a doping profile below the silicon surface. This is the case of the back surface field (BSF) formed in the back side of conventional p-type solar cells by annealing the backside metallization at a temperature higher than the aluminium-silicon eutectic point. A p-p^+ junction is formed by the aluminium atoms which diffuse in the silicon backside, generating an electrical field.

(ii) The introduction of stable electrostatic charges by depositing an insulator layer with fixed charges as silicon nitride or silicon oxide.

Bulk passivation is also performed by means of silicon nitride deposition, by effusion of hydrogen inside of the silicon bulk, which passivates defects [18]. There exists another method to decrease recombination in the silicon bulk: the gettering process. Gettering consists in reducing recombination centres by moving impurities and defects to regions away from the device active regions [19]. Two common methods are the phosphorous gettering which occurs during phosphorous diffusion of the emitter, and the aluminium gettering which is produced by the aluminium diffusion on the back side of the cell by aluminium metallization and annealing. These two methods of extrinsic gettering (i.e. external impurities are introduced to perform the gettering process) are based in the higher solubility of impurities in the rich doped layers to which they segregate [20]. The gettering processes are of special importance for multicrystalline silicon, where the concentration of defects and impurities is higher.

3 Fundamentals of silicon texturization

3.1 Introduction

Silicon chemical texturization is one of several uses of silicon etching, which comprises also other processes as polishing, chemical cleaning, saw damage removal, etc. In an etching process Si atoms are removed from the wafer surface by chemical or electrochemical reactions, as well as by physic-chemical processes. Regarding to texturing processes, the aim is to produce a specific morphology on silicon surface able to redirect reflected light inside the device to be absorbed.

By means of texturization processes an amount of silicon is etched from the surface, being the strength of this attack defined by the etching rate, or amount of silicon removed per unit of time, normally expressed in µm/min.

Regarding to how silicon is etched and to the mechanism of formation of the microstructures on the silicon surface, etching of silicon can be classified into anisotropic, if the etching rate differs depending on crystal orientation (an example is the preferential etching of (100) planes by alkaline solutions, while (111) planes are etched very slowly) or isotropic, so called when the etching rate have similar values independently of crystal orientation. A detailed description of the underlying processes is given in sections 3.3 and 3.4. Isotropic processes are of great importance when multicrystalline substrates are used for the fabrication of solar cells, due to the different crystal orientations present in the wafers.

Wet chemical texturization of silicon started in the 1950s with the work of Uhlir [21] at Bell Telephone Laboratories, who introduced the porous semiconductors concept in microelectronic industry. This was the birth of porous silicon, which is generally achieved by isotropic electrochemical etching of silicon in an acid medium with mixtures based on HF.

In the 1960s, anisotropic processes, in which alkaline solutions are used to etch silicon with different results depending on the crystal orientations, were studied for the first time [22, 23, 24], mainly applied to microelectronics.

The application of textured silicon surfaces to solar cell dates from 1961 [25], but in that case the texturization was achieved by mechanical methods. The first wet chemically, anisotropically textured solar cell was developed in 1974 at COMSAT Laboratories and named after “black cell” by Haynos et al. [26]. In 1976 Restrepo and Backus published their results about a KOH textured solar cell [27].

3.2 Optical benefits of textured silicon

Front reflectance reduction

The wavelength dependent reflectance of normal incident light on the silicon surface is determined by the complex refractive index $n_c = (n - ik)$ of silicon and air:

$$R = \frac{(n_{c0} - n_{c1})^2}{(n_{c0} + n_{c1})^2} \qquad (3.1)$$

being in this case the subscripts *0* and *1* for silicon and air respectively, and *n* and *k* the real and imaginary part of the refractive index, dependent on the wavelength. For air, as convention *n* and *k* take the fix values of 1 and 0 respectively, thus:

$$R = \frac{(n_0 - 1)^2 + k_0^2}{(n_0 + 1)^2 + k_0^2} \qquad (3.2)$$

In Figure 3.1 the wavelength dependency of the calculated front surface silicon reflectance is depicted, in the case of a sufficiently thick wafer for which back reflection can be neglected. The values of *n* and *k* for silicon at 300 K have been obtained from reference [28].

Taking this data and the solar spectrum (AM1.5G) into account, it can be calculated[2] that 35 % of solar light in the range of 400 to 1100 nm, which could contribute to photogenerated current, is lost by front reflection.

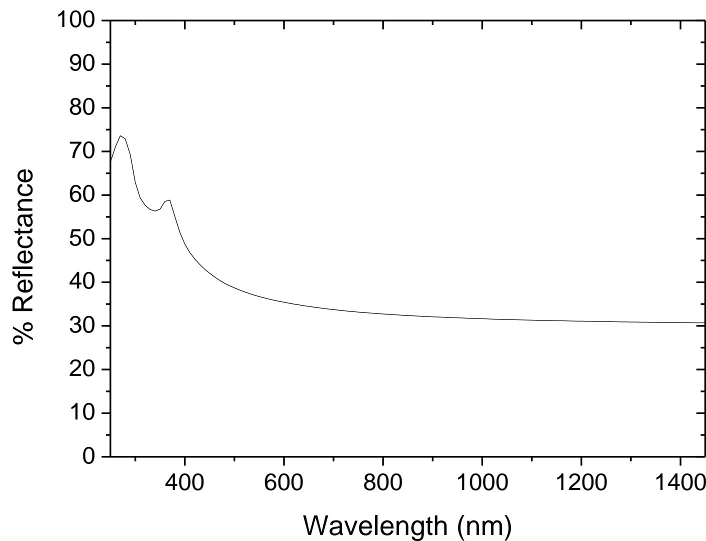

Figure 3.1. Reflectance curve of silicon.

[2] See Equation 4.5.

There are two main solutions to reduce these front reflection losses in the solar cell: by means of an antireflection coating (ARC) or by texturing the silicon surface which in most cases will be also coated with an ARC to further reduce front reflection.

In the case of texturization, silicon microstructures are formed on the silicon surface. These structures are able to redirect reflected light rays with the appropriate angle, impinging again the silicon surface. A schematic view of the underlying geometrical considerations is shown in Figure 3.2, which represents a two dimensional simplification of the profile of a pyramid textured surface.

The angle and the height of the structures will influence the number of bounces on the front surface. The angle of the pyramid walls to the wafer surface α is 54.7º for the case of random pyramids produced by anisotropic alkaline etching, as determined by the angle of {100} and {111} Si planes. It has been calculated by other authors that 30 % of normally incident light impinges three times the front silicon surface textured with random upright pyramids [29].

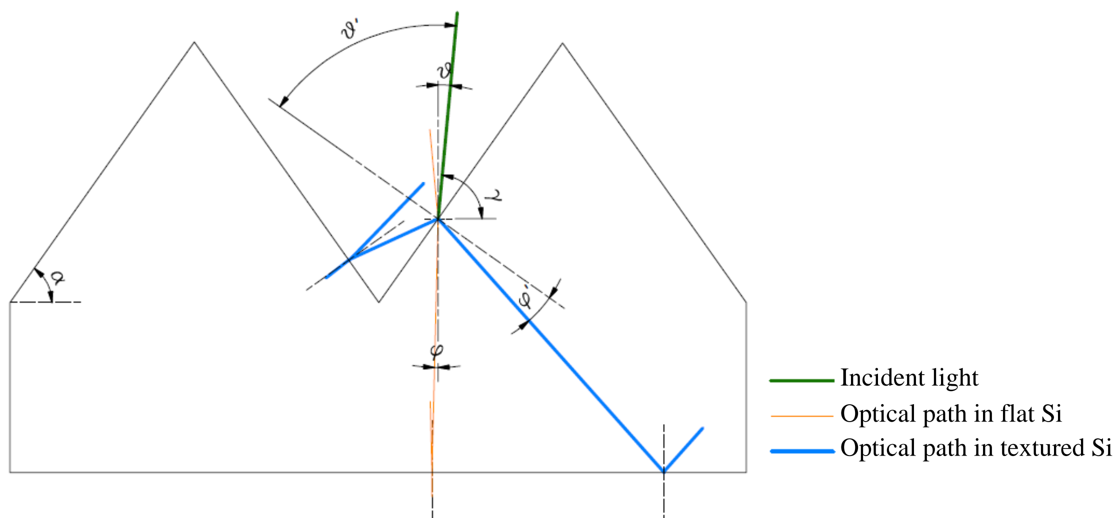

Figure 3.2. Scheme of the optical path of incident light in silicon depending on the angle of incidence.

In Figure 3.2 it can be observed how an incident ray with angle γ with respect to the wafer horizontal is reflected with a higher angle θ' to the surface normal, impinging again in the neighbour pyramid wall. The entire incident light that reaches the surface with an angle γ to the wafer horizontal between α and $\alpha + 90°$ will experience at least a second bounce. Therefore normally incident light (which is the light that accounts for standard characterization of solar cells) suffers lower reflection in textured solar cells.

In the following table, the measured front reflection light losses for polished and textured (with $Na_2CO_3/NaHCO_3$ solution) FZ silicon samples, produced in the context of this thesis, with and without SiN_x antireflection coating are compared. The losses are expressed as standard weighted reflectance *SWR* (see Equation 4.5 for definition) in

percentage. The expected J_{sc} and efficiency calculated with PC1D[3] [30], introducing in the program the measured reflectance curves for every front surface, is also shown in the table.

Table 3.1. Front reflection losses in FZ silicon with different surfaces and its influence on J_{sc} and efficiency.

Front surface	% $SWR_{400\text{-}900}$	J_{sc} (mA/cm^2)	% *Eff.*
Shiny etched Si	37.6	24.4	13.6
Textured Si	11.8	34.3	19.5
Shiny etched Si + ARC	8.1	35.1	20.0
Textured Si + ARC	2.1	37.6	21.3

The texturization process and the deposition of an antireflection coating clearly reduce the front reflection, and this increases short circuit current and therefore the efficiency. Here, the higher surface recombination, which can be introduced by surface texturization (and will be discussed in chapter 7.1) has not been taken into account, as the aim was merely to illustrate the influence of the optical effect.

Light trapping

Some attention should be also paid to the light that escapes by the back surface of the wafer due to transmission. With the purpose of redirecting it again to the silicon bulk, back reflectors are used. This can be achieved by coating the back surface with a metal that acts also as back contact, which reflects the light back towards the front surface, improving the so called light trapping effect. The path length of the weakly absorbed light inside the silicon will be then increased, giving to the photons more probabilities of being absorbed.

Figure 3.2 shows how the angle of the light refracted in the silicon has a higher angle φ' for the textured surface (following Snell law of refraction[4]), and this effect increases the path length through the silicon substrate. Because of the same reason, in textured wafers the light has more probabilities of striking the back surface with an angle higher than the

[3] Parameters used: Thickness: 200 μm. p-type background doping: 10^{16} cm^{-3}. Front diffusion: 50 Ω·sq, 0.55 μm junction depth. Bulk recombination: 1000 μs. The files from the program have been used for wavelength dependent absorption coefficient, refractive index and light excitation. The rest of the parameters have been kept as default.

[4] $n_1 \sin\theta = n_0 \sin\varphi$, where n_0 and n_1 would be in this case the refraction index of silicon and air respectively, θ the angle of incident light to the wafer normal and ϕ the angle of refracted light to the wafer normal.

critical angle θ_c for Si-air interface[5] (fact that produces total internal reflection) than in flat wafers. Both effects improve the light trapping of normally incident rays in textured wafers compared to flat ones.

The light trapping enhancement is of special importance in the case of thin wafers. Crystalline silicon solar cells tend to be produced with thinner wafers because of two reasons: one is the obvious cost reduction and saving of materials when thinner wafers are used, and another reason is the reduction, by thinning the wafer, of Auger recombination, which results in a higher open-circuit voltage of the cell [31]. But in a thinner silicon wafer the short light path would decrease the probability of absorption of long wavelength photons and subsequently the short-circuit current. Thus, the improvement of light trapping is needed.

Influence of textured surface in solar cell parameters

The main parameters affected in the solar cell by a textured surface are the short circuit current and the open circuit voltage. Roedel and Holm [32] described the change in these parameters depending on the decrease of reflectance for the short circuit current increase, and on the increase of the surface area (and subsequent increase of the dark current) for the open circuit voltage decrease, as shown below.

The short circuit current density J_{sc} increases with reflection reduction:

$$\frac{\Delta J_{sc}}{J_{sc}} = \frac{(1 - R_T) - (1 - R_0)}{1 - R_0} = \frac{1 - R_T}{1 - R_0} - 1 \tag{3.3}$$

where R_T is the reflectance of the textured surface and R_0 is the reflectance of the flat surface.

On the other hand, the dark current density J_0 experiences an increase due to a higher surface area in the textured surface:

$$\frac{\Delta J_0}{J_0} = \frac{A_T - A_0}{A_0} \tag{3.4}$$

where A_T is the surface area of the textured surface and A_0 the surface area of the flat surface.

Therefore, the open circuit voltage V_{oc} decreases as:

$$\Delta V_{oc} \approx \frac{kT}{q}\left[ln\left(\frac{Jsc + \Delta J_{sc}}{J_0 + \Delta J_0}\right) - ln\left(\frac{J_{sc}}{J_0}\right)\right] = \frac{kT}{q} ln\left[\frac{(1 - R_T)/(1 - R_0)}{A_T/A_0}\right] \tag{3.5}$$

[5] $\theta_c = 15.3°$ if we consider the value of $n_0 = 3.8$ for Si and $n_1 = 1.0$ for air.

The increase in J_{sc} has more weight than the V_{oc} decrease, leading finally to a gain in the efficiency. This is a simplified approximation, as many other factors play also a role, as the light trapping effect or the influence that the surface features have in the solar cell processing affecting series resistance, fill factor, etc., but this will be further discussed in this thesis with examples of real solar cells (chapter 7).

Types and comparison of geometrically textured surfaces

Several authors have analysed the front reflectance and light trapping performance of different texturing arranges by ray tracing. Below some of the findings about this aspect present in the current bibliography are summarized.

The most common examples of geometrical surface texture are slats or grooves, inverted pyramids and upright pyramids (both periodic and random). On the other hand, the Lambertian surface, which reflects light randomly in all directions is assumed as an ideal case for light scattering, and has been modelled, as a reference by several authors [33, 34], namely as an example of ideal surface for internal reflection aiming light trapping. The inverted and regular or periodical upright pyramids, as well as the grooves, present the disadvantage of needing a mask to be produced on the silicon surface, facing to the more simple formation of random pyramids by anisotropic chemical etching. This work will be focused in the latter type of texture.

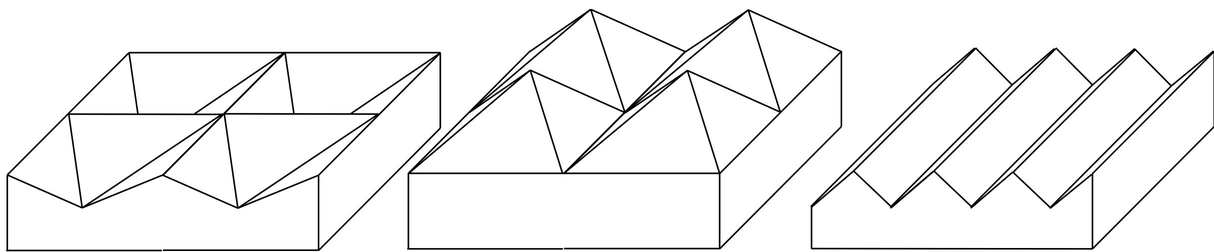

Figure 3.3. Examples of geometrical textures: inverted pyramids (left), upright pyramids (center), grooves (right).

Among the geometrical features, the inverted pyramid arrangement stands out regarding to light coupling enhancement [29, 33, 34]. Considering upright pyramids, random arrays give a better optical performance than regular ones [29, 33].

Recently, Baker-Finch and McIntosh [35] have developed an enhanced model to calculate the photogeneration profile in pyramidally textured solar cells, in order to compare more accurately the increase of the current obtained when pyramidal features are used as texture. They conclude, as in the previous studies, that inverted pyramid array presents reduced front reflection losses compared to upright pyramids or grooves, followed by random upright pyramid array. But regarding to light trapping, random upright pyramids have a similar behaviour to inverted ones. After calculating the current collection losses (due to recombination of the minority carriers before reaching the contacts), they state that inverted and random upright pyramids present similar

collection losses in the case of high efficiency solar cells (in which recombination is significantly low). Taking into account this aspect, the higher complexity and costs related to the formation of inverted pyramids would not be worth. This is not the case of standard screen printed cells, in which the high minority carrier recombination makes it important to generate the carriers near the p-n junction in order to avoid collection losses. Inverted pyramids or grooves present in this type of cells lower collection losses, but as mentioned above, the production costs would be higher.

3.3 Silicon texturization techniques

Texturization methods can be classified in mechanical methods, which shape the silicon surface by means of "cutting" it, or etching texturization methods, which have been defined previously. The latter can be carried out in chemical solutions, being known as *wet chemical processes*, or in contact with vapour or gases under certain vacuum conditions, known these techniques as *dry etching processes*.

In wet chemical processes the etching of silicon occurs via chemical or electrochemical routes while dry processes are based in physical or physic-chemical processes.

Laser based processes are also another option to texture silicon [36].

3.3.1 Dry etching processes

Dry processes can be seen in some cases as more advantageous due to the fact of handling chemical solutions is not needed and due to its fine control of the process. However, the vacuum conditions needed and the use of gases make these methods to require more sophisticated and expensive set-ups, and therefore to be more difficult to be implemented in the industry. Also, they present a lower throughput than wet chemical methods. On the other hand, some of the gases employed can be toxic, as for example, chlorine [37].

Dry etching processes produce higher contamination on the wafer than wet chemical processes as they occur in low pressure chambers where there is generation of particles due vacuum conditions, which are re-deposited on the wafer surface [38].

Another consideration is the damage that some of these methods can induce on the surface (due to the ion bombardment of the surface, for example) [39], which could affect electrical performance of the final device through an increase of minority carrier recombination.

The main isotropic nature (if we attend to the preferential etching rates of certain crystallographic planes) of many dry etching methods also requires the use of masks when special features like up-right or inverted pyramids or V-grooves are desired, complicating the process by adding steps like oxide deposition, photolithography,

alignment of the mask, etc. It is important to point out that the concept of anisotropy in dry etching technologies often refers to a high vertical/lateral etch ratio, as in many etching processes used in microelectronics the under-etching below the masks is an undesired phenomenon.

When no masks are used, the morphology obtained can go from crater-like structures, typical of isotropic processes, to needle-structures. The size of the structures obtained by dry etching processes tends to be smaller than the ones formed by wet chemical etching. Their isotropic behaviour makes these techniques devoted principally to multicrystalline substrates.

Despite of texturization, dry etching techniques can find application in the industry as processes to remove PSG (phosphorous silicate glass) or edge isolation [40], but wet chemical processes are widely more implemented in the industry due to their simplicity. Some of the more relevant techniques of dry etching are shortly summarized below. For a better understanding of dry etching technologies principles see references [41, 42].

Plasma-less dry etching

With this technique the silicon is etched by the action of gas molecules without need of any other supply of energy. The gases used for this purpose should be very reactive; because of this reason halogen vapours are used as $XeFe_2$, BrF_3, ClF_3. They mainly present vertical anisotropy [43]. The reactants are supplied directly as gas, or in some cases as liquids or solids that have a considerable equilibrium vapour pressure, and the reaction takes place normally in a vacuum chamber. An example of plasma-less dry etching applied to silicon texturization is the formation of honeycomb structures by means of ClF_3 etching using silicon oxide or photoresist films as masks [44].

Plasma etching

The plasma state is generated from a gas in a vacuum chamber. In the plasma state a gas is ionized, containing charged and neutral species at the same time. The ionized species and free radicals react chemically with the silicon surface. Gases are considerably more reactive in their plasma state, which supplies the needed activation energy to the etching to occur. The plasma state is excited by an electric field by means of radio frequency or microwave sources, for example. This technique is also called radical etching as ion bombardment is almost negligible and it is the chemical reaction between radicals and the substrate what plays the main role. Hydrogen plasma etching can be named as an example of this kind of processes [45].

Sputtering

Silicon can also be etched by means of bombarding its surface with ions. When inert gas ions with high energy impact the surface, Si atoms can be etched through this physical process. It is rarely used to texture silicon due to the slow rate of these processes and the induced damage.

Reactive ion etching

Reactive ion etching (RIE) is a mixture of both radical etching and ion bombardment, as in the created plasma both kind of species are present and able to attack silicon surface atoms. It is fairly the most extended among dry etching processes for silicon texturization as the etching rate is higher than in other techniques. A common gas mixture used in RIE for texturization in solar cells is SF_6/O_2 [37, 46].

Laser texturization

Laser processes for the solar cell manufacturing have been developed during the last years in order to perform edge isolation, buried contacts, doping of silicon, firing processes, etc., especially in order to be included in high efficiency solar cell concepts. Their still high costs have not allowed these techniques to be yet widely implemented in the industry. Regarding to texturization of the silicon surface it is not yet a representative technique neither in laboratory cells field. Laser processes induce defects on silicon, therefore in the case of laser texturizations a chemical etching is subsequently needed [47, 48].

Laser texturization is based in laser ablation, in which silicon is removed by subsequent melting and evaporation under radiation absorbed by the material and generated by a pulsed laser. Nd:YAG lasers (1064 nm) are commonly used for this purpose [47], but higher energy lasers are also used.

Recently, self-assembled micro or nanostructures produced by ultra-fast lasers (with a pulse in the order of femtoseconds to nanoseconds) to enhance light trapping are also being studied [49].

3.3.2 Wet chemical processes

Wet chemical etching consists on the etching of the silicon surface mostly by immersion of the wafers in a solution containing etchants. According to the nature of the etching agents, the wet chemical etching processes could be classified in acidic etching and basic etching (generally designated as alkaline etching). This difference in nature influence the etching mechanism of Si and the end result of the surface morphology.

While acidic solutions present in general an isotropic etching behaviour, alkaline etching (depending on the etchant, and its concentration) can be used, but not only, to etch anisotropically a silicon surface with the appropriate crystallographic orientation.

Wet chemical etching processes can be combined with the use of etching masks or assisted by additional current and performed in an electrochemical cell.

Acidic etching is widely used in the solar cell industry to etch multicrystalline silicon, as in this material anisotropic etchants would not be suitable due to the different crystal

orientation of the grains. It is used with the aim of polishing or texturing silicon surface, depending in the reactives and proportions used.

Some acidic etchants, as for example HF, are able to dissolve silicon oxide. Therefore, several acidic mixtures contain HF and oxidation agents in order to oxidize the silicon surface atoms, which will be subsequently dissolved by HF. This is the principle of the so called *stain* etching. Among the isotropic etching methods, wet chemical etching methods as stain etching with acidic solutions are quite adequate to be implemented in the industry due to its suitability and simplicity, and lower cost [50, 51].

The stain etching with acidic solutions has been firstly studied by H. Robbins and B. Schwartz [52] who determined the global chemical reaction of the HF/HNO_3 system with the silicon surface as following:

$$3Si + 12HF + 4HNO_3 \rightarrow SiF_4 + 4NO + 8H_2O \quad (3.6)$$

In this redox reaction the nitric acid oxidizes the silicon surface and the hydrofluoric acid dissolves the silicon oxide formed. Acetic acid can be added as diluent [53]. Other oxidation agents as H_2SO_4 or H_2O_2 can be used.

Stain etching, when used to texture silicon, produces pores on the surface. Figure 3.4 shows a SEM image of a multicrystalline silicon surface treated with HF/HNO_3.

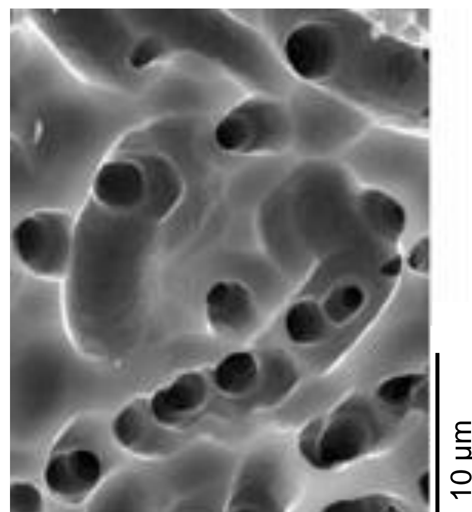

Figure 3.4. SEM image of HF/HNO_3 textured mc-Si.

Among the basic etchants, we can find organic compounds as ethylenediamine/pyrocatechol (EDP), hydrazine or tetramethylammonium hydroxide (TMAH); or inorganic compounds as sodium hydroxide, potassium hydroxide or ammonium hydroxide [54]. The carcinogen character of the EDP [54] and hydrazine [55] systems make more convenient the use of the cited hydroxides. The aqueous solution Na_2CO_3/ $NAHCO_3$ studied in this thesis is also a basic etching system for Si

[9]. The common characteristic of all these solutions is their high pH and therefore high content of OH^- ions, crucial for the etching reaction that will be discussed below.

In solar cell processing, KOH and NaOH solutions are the most employed from the alkaline etching systems [56]. Normally the solutions contain IPA (isopropyl alcohol) as surfactant. The alcohol limits the etching rate of the silicon dissolution. The behaviour of these hydroxide solutions differs depending on their concentration. For example, KOH etching with concentrations of above 30 wt% results in a *smooth* surface, while below this concentration pyramids are formed on (100) Si [57]. Thus, NAOH and KOH can be used to etch Si both anisotropically and isotropically. The latter is the case of the use of KOH and NAOH for the process named saw damage etching, used to remove the damage induced in the Si wafers by the sawing process. The etching rate is notably higher in the case of high concentration alkaline solutions with isotropic behaviour.

In the case of solar cells, when monocrystalline Si is used as substrate, the alkaline anisotropic etching is preferred as texturization procedure rather than the acidic etching due to high roughness induced by the latter, which would affect in a higher grade the surface recombination. Another advantage of alkaline solutions is that they avoid the use of HF in the texturization step, decreasing environmental and safety problems derived from its high toxicity.

3.4 Anisotropic etching of silicon

The different behaviour of distinct crystal orientation of silicon under certain etching conditions has been already mentioned. In alkaline medium, the higher etching rate of (100) Si compared to other crystalline orientations leads to the formation of pyramids or hillocks in this oriented silicon surface. The resulting pyramids have facets with {111} orientation and an angle of 54.7° to the surface, given by the intersection angles between {100} and {111} planes (Figure 3.5). The pyramids have a rectangular base limited by <110> ridges.

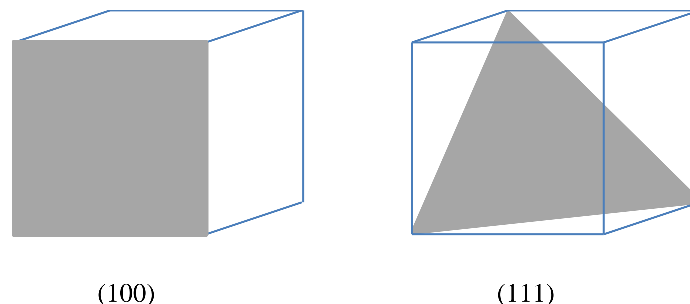

(100) (111)

Figure 3.5. (100) and (111) crystallographic planes.

In Figure 3.6, the structure of the surfaces of Si (100) and (111) are depicted. It can be observed that while the (100) structure has two bonds attaching the surface atoms to the Si crystal bulk, (111) Si has three bonds. Therefore, in (111) Si, three bonds should be broken to detach the Si surface atom from the lattice instead of the only two bonds needed for dissolving (100) Si. This fact explains the higher etching rate of (100) Si.

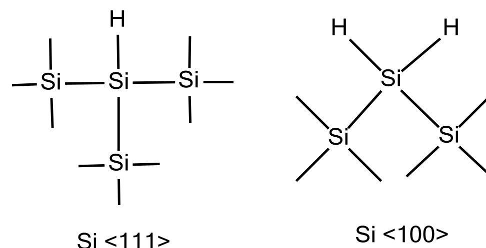

Figure 3.6. Chemical bonds of (111) and (100) Si.

Despite of the pyramids formed in the (100) oriented Si surface, in (111) surfaces, terraces are formed. The resulting surfaces of (100) and (111) p-FZ Si wafers after the reaction with the Na_2CO_3/$NaHCO_3$ solution studied in this thesis are shown in Figure 3.7. The etching rate in this case was approximately 10 times higher for (100) Si compared to (111) Si at the same process temperature.

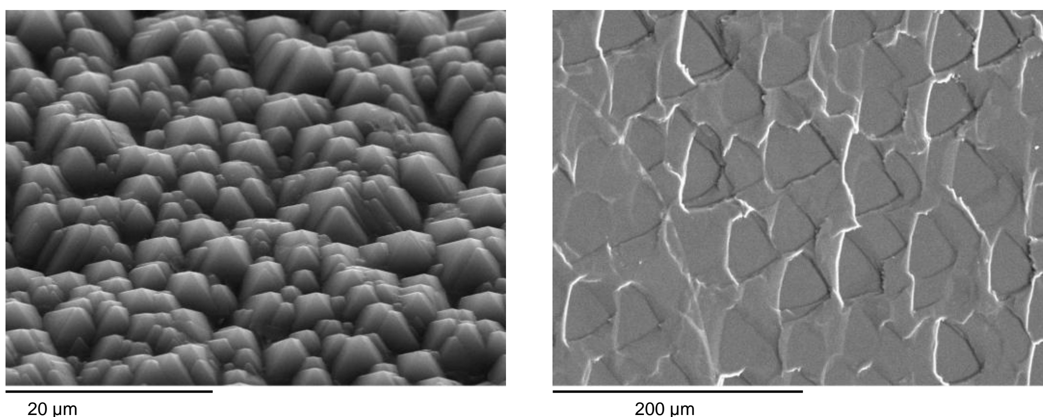

Figure 3.7. SEM images of alkaline textured (100) Si (left) and (111) Si (right).

In the dissolution of silicon with alkaline solutions, the species involved in the reaction are water molecules and hydroxide ions (OH^-), with H_2 and $Si(OH)_4$ (or its product $SiO_2(OH)_2^{2-}$ at pH>12) as reaction products [57, 58]. Cations and additives like IPA do not participate directly in the reaction [57, 58]. Different authors propose different reaction mechanisms that are described below.

Palik et al. identified, by Raman spectroscopy, the OH^- ions as a reactant since they observed a decrease of the intensity of the corresponding line in the spectra [58]. Later,

they suggested an etching mechanism based in the sequential attack of Si-Si bonds by water molecules and OH^- ions [59], described by the reaction:

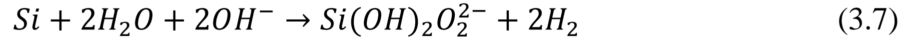

$$Si + 2H_2O + 2OH^- \rightarrow Si(OH)_2O_2^{2-} + 2H_2 \tag{3.7}$$

Seidel et al. [57] have modelled the anisotropic etching of silicon by alkaline solutions as an oxidation/reduction process where the oxidation reaction is:

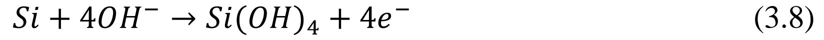

$$Si + 4OH^- \rightarrow Si(OH)_4 + 4e^- \tag{3.8}$$

The reduction reaction is:

$$4H_2O + 4e^- \rightarrow 4OH^- + 2H_2 \tag{3.9}$$

In this electrochemical model, they identify the water content in the solution as an active and necessary component [57], and the important role of the water concentration in the reaction, as it can be deduced from the equations above. Water provides hydroxide ions that shift the oxidation reaction to the right. In surface Si atoms, dangling- and backbonds introduce surface states within the gap. Electrons from hydroxide ions are transferred to the conduction band in the oxidation step, binding the OH radical to the Si. The high electronegativity of O atoms will weaken the Si-Si backbonds. The alkaline solution supplies the necessary activation energy to break these bonds and form a silicon complex which will react with hydroxide ions to produce $Si(OH)_4$. In the reduction step, the excess electrons in the conduction band are transferred to the water, which is reduced to hydroxide ions and hydrogen. The authors assume in their model that these hydroxide ions from water reduction are the ones that oxidize the silicon, and not the hydroxide from the bulk of the solution, which are supposed to play a minor role in the reaction itself [57]. After Seidel et al. the different behaviour of (100) Si with respect to (111) Si is explained through the different surface states located within the band gap in the different oriented surface Si atoms.

Allongue et al. [60], on the other hand, propose a model in which both chemical and electrochemical reaction take place, with predominance of the chemical reaction at OCP (open circuit potential). The purely chemical reaction of silicon etching can be described following one of the chemical routes proposed by Allongue et al., as it is depicted in Figure 3.8.

In this model, the only reactant is the water, which hydrolyses Si-H and Si-Si bonds of Si surface atoms. The resulting surface is -H terminated due to the positive charge induced in the kink site atom by the polarization of the kink site atom-ligands bond. This make that OH^- ions substitute the free bond of the kink site atom while the *bulk* Si atom is -H terminated. The authors explain that, even when water molecules are the reactants, hydroxide ions play also an important role, as they catalyse the hydrolysis of

the bonds, and form soluble etching products. At lower pH, the remaining Si surface would be passivated by an oxide layer [60].

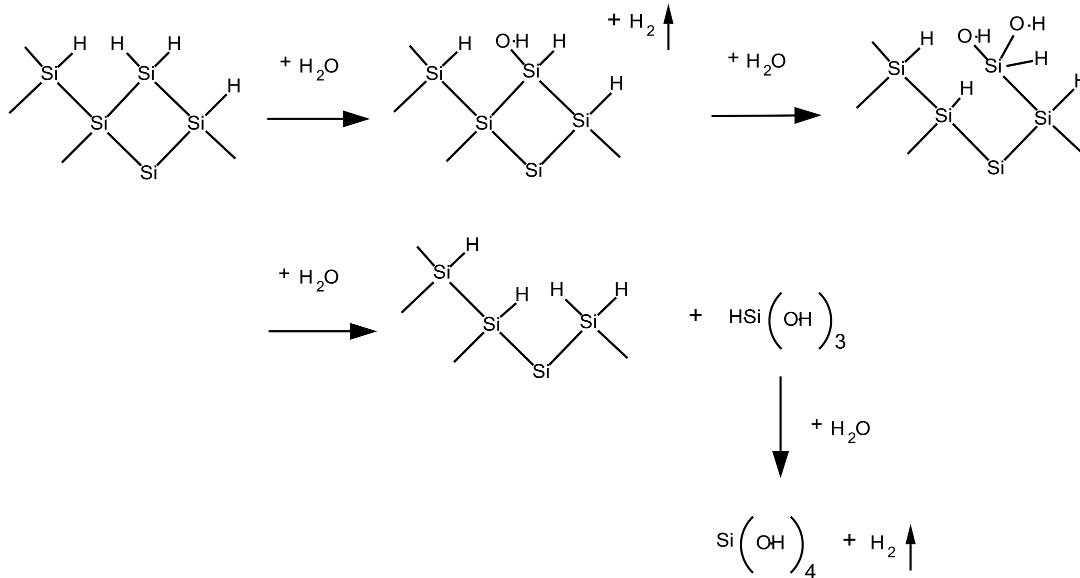

Figure 3.8. Chemical dissolution of Si (100) according to Allongue [60].

3.5 Previous work on Na_2CO_3/$NaHCO_3$ texturization

In 1999, Nishimomoto and Namba [9] presented for the first time a Na_2CO_3 solution as an alternative to the hydroxides/IPA mixtures used in the industry. They proposed an optimum concentration of sodium carbonate of 20 wt% to texture (100) Si, and proved that when sodium bicarbonate is added the size of the pyramids is smaller and the reflectance reduced within the same etching time compared to the Na_2CO_3 solution.

W. Sparber et al. [61] modified the recipes of Nishimoto and Namba and found optimum concentrations of 12 wt% Na_2CO_3 and 1.5 wt% $NaHCO_3$ during 40 minutes at 90 °C.

In 2007 Marrero et al. [10] used Na_2CO_3/$NaHCO_3$ textured (100) Cz substrates to fabricate phosphorous diffused solar cells, proving that the process is compatible with the production of solar cells. The parameters of the reaction in this case were found optimum as following: 20 wt% Na_2CO_3 and 4 wt% $NaHCO_3$ at 95 °C, and 20 minutes of etching to achieve minimum reflection.

Other works about Na_2CO_3 /$NaHCO_3$ texturing can be found in the references [62, 63, 64] but the ones exposed above can be considered the most relevant.

In this thesis the work of Marrero et al. is considered as starting point to further investigate: (i) which parameters really influence the texturization and how the

pyramids are formed, (ii) the possibility of reducing the high amount of reactants proposed by the existing bibliography in order to design an appropriate process to implement this texturization step in the industry, and (iii) how the electrical parameters of solar cells are affected by the Na_2CO_3 /$NaHCO_3$ texturization.

4 Experimental methods

4.1 Production processes

4.1.1 Texturization process

The alkaline texturization of silicon wafers has been carried out mainly in the Laboratory- and Servicecenter Gelsenkirchen of Fraunhofer ISE. Some of the texturization experiments have been also performed in the laboratories of the Departamento de Física Básica of the University of La Laguna.

The texturization experiments are done in a wet chemical bench with exhaust system, which is located in a technology laboratory with controlled atmosphere in order to avoid contamination of the silicon substrates. Inside of the wet chemical bench the controlled atmosphere reaches the class 100. The material of the wet chemical bench is polypropylene.

After laser marking and cutting the wafers, they are rinsed in deionised water in the wet chemical bench, provided of watering basins with automatic rinsing programs to remove particles and water soluble impurities. Afterwards, the wafers are immersed in 1 vol% HF solution and rinsed in deionised water again prior to the texturization. The HF step is done in order to remove the native silicon oxide of the surface, which would negatively affect the alkaline etching.

The alkaline texturization solutions are mixtures of Na_2CO_3/$NaHCO_3$ in deionised water. During the texturization process the silicon samples are vertically hold by a Teflon sample carrier, designed to avoid the floating of the wafers inside the solution. The floating of the wafers is produced by the H_2 bubbles which result from the silicon etching reaction. No agitation or recirculation of the solution is applied.

After the texturization process the wafers are directly rinsed in deionised water and subsequently dried in N_2.

In order to control the etching rate of the texturing solution the wafers are weighted before and after the texturization.

Set-up description

- Laboratory scale:

  Part of the texturization experiments were carried out in an opened glass vessel containing 4 litres of the texturing solution. To reach the desired temperatures, a hot plate was used and the temperature was controlled with a thermometer. A number of 4 to 6 wafers are textured in every batch.

- Semi-industrial scale:

  The wet chemical bench is provided with PTFE (polytetrafluorethylen) Teflon closed basin heated by a PTFE coated resistance heater placed on its bottom and with temperature control. This basin was filled with 12 litres of texturing solution to carry out the experiments, and can be closed with a lid to avoid the evaporation of the solution. Up to 25 wafers per batch can be processed.

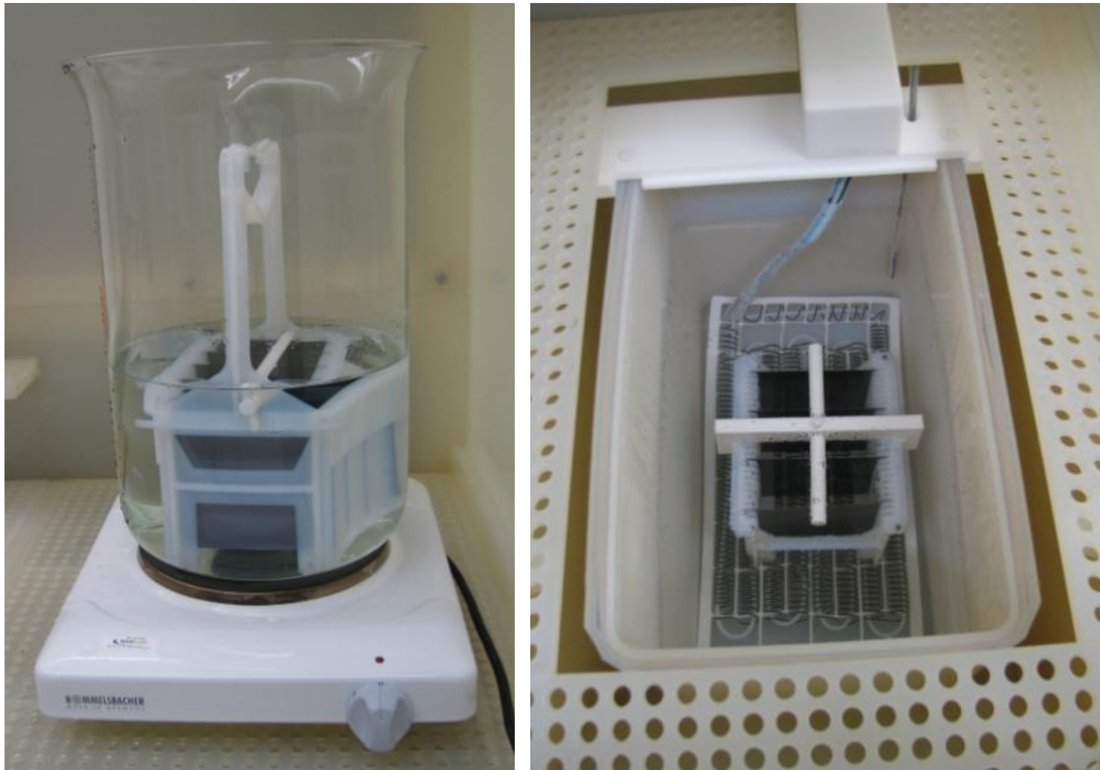

Figure 4.1. Laboratory-scale (left) and semi-industrial-scale (right) texturization set-ups.

Chemicals

The chemicals used for the pyramidal texturization are sodium carbonate anhydrous (Na_2CO_3 Assay 99.8) and sodium bicarbonate ($NaHCO_3$ Assay 99.5-100.5).

For the sodium hydroxide based processes sodium hydroxide with a purity ≥ 99% in pellets is used.

It should be noticed that the chemicals used in solar cell production should be of high purity in order to avoid contamination which could introduce defect states in the bandgap and decrease the solar cell performance. The chemicals are solved in 18 MΩ·cm deionised water.

Substrates

Different types of commercial silicon wafers with different properties have been textured in this work in order to verify the applicability of the texturing process. The silicon substrates employed in this thesis were Czochralski (Cz) and Float-Zone (FZ) grown wafers, and their specifications are listed in Table 4.1.

Table 4.1. Specifications of the initial silicon substrates used in this work to perform the texturization and the solar cells experiments.

Silicon	Orientation	Surface	Doping type	Resistivity (Ω·cm)	Thickness (µm)
Czochralski 125 x 125 mm pseudo-squared	(100)	As cut	p (Boron)	1.0-3.0	210
Czochralski 125 x 125 mm pseudo-squared	(100)	As cut	n (Phosphorous)	1.0-3.0	240
Czochralski 4 inch	(111)	Polished	n (Phosphorous)	1.0-2.0	250
Float Zone 4 inch	(100)	Shiny etched	p (Boron)	0.8-1.2	250
Float Zone 4 inch	(100)	Shiny etched	n (Phosphorous)	0.8-1.2	250

The 125 x 125 mm pseudo-squared wafers are cut in 100 x 100 mm to be used in the solar cell fabrication process or texturization experiments. Some texturization experiments have been realised using cut pieces of silicon of approximately 16 cm^2 area.

4.1.2 Solar cell processing

The solar cells have been produced in the Laboratory- and Servicecenter Gelsenkirchen of Fraunhofer ISE, following its standard process for diffused crystalline solar cells. The

laboratory is equipped with a clean room class 1000 with a pilot solar cell production line.

An overview of the solar cell fabrication process is shown in Figure 4.2. The solar cells studied in this work are alkaline textured by means of $Na_2CO_3/NaHCO_3$ solutions. Some samples have been submitted to the standard saw damage etching step. This etching process, contrary to texturization, produces an approximately flat silicon surface with higher reflection than a pyramidally textured surface. The material used for the diffused solar cell fabrication described in this section is p-type Cz silicon.

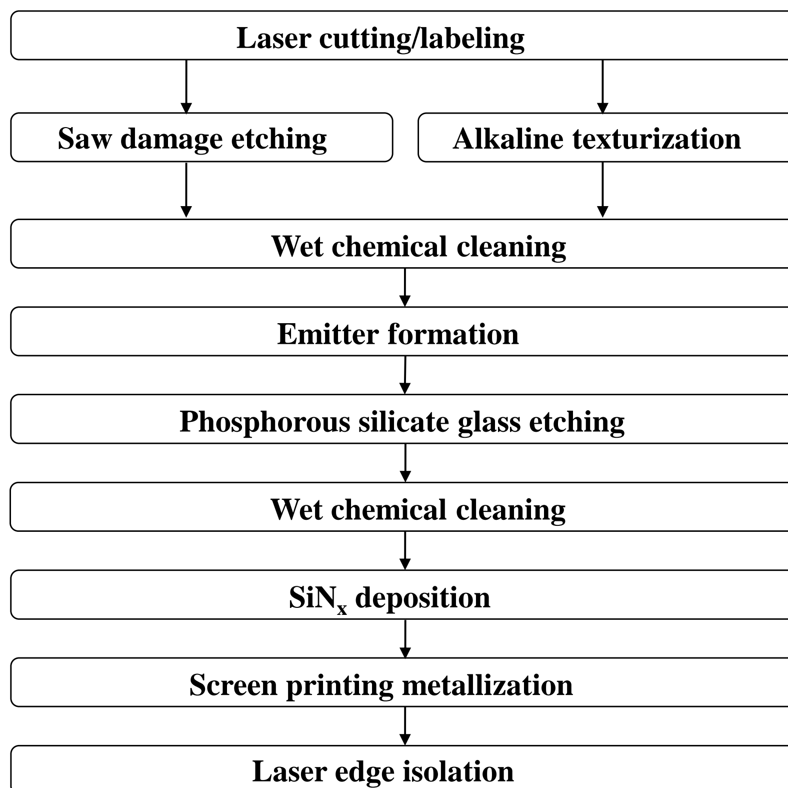

Figure 4.2. Scheme of the crystalline silicon solar cell fabrication process.

Saw damage etching

The aim of a saw damage etching step in a solar cell production process is to remove the first micrometres of the wafer surface. The damage is produced by the saw while cutting the silicon ingot into wafers. This surface damage affects the surface recombination of the cells, and should be removed to reach an adequately low surface recombination velocity. Furthermore, particles and impurities that are in the surface are also removed, avoiding further possible contamination which may occur during the high temperature steps of the process by diffusion of these impurities. For this purpose of damage removal, acidic or alkaline solutions can be used. In Section 3.3.2 it is already mentioned the use of alkaline solutions at high concentrations (> 30 %) without

surfactants (which would decrease the etching rate) in order to obtain an isotropic etching of the silicon surface with high etching rates.

A solution of 30 wt% NaOH in deionised water at 83 °C was used in this case. The wafers are etched in a Teflon basin like the one described in Section 4.1.1 containing the NaOH solution. The wafers are hold in a Teflon wafer carrier with capacity for 25 100 x 100 mm wafers. After the etching, the wafers are immersed in HCl solution to stop the chemical reaction and subsequently rinsed in deionised water and dried in N_2. Etching rates of 2-4 µm/min are obtained depending on the silicon surface characteristics, etching around 15 µm per side from the wafers.

Wet chemical cleanings

The wet chemical cleaning applied through the solar cell process is of crucial importance, as it avoids impurity contamination of the wafers which would decrease the lifetime of the charge carriers and finally the efficiency of the cells. In this cleaning, the first nanometres of the silicon surface are etched, and the impurities and particles removed. The impurities and particles present on the wafer surface come from the handling of the wafers, the processes they are submitted to, or simply deposited from the environment [38]. The cleaning should be carried out after chemical steps which could induce contamination, before high temperature steps that can induce diffusion of impurities, or before deposition of layers in order to maintain a clean interface. In the process described in this section, the cleaning plays a special role before the phosphorous diffusion and before the antireflection coating deposition.

Another important aspect is the surface termination and the nanoroughness resulting from the surface cleaning [65, 66].

There exist several cleaning methods [38], but the main principle commonly lies on the removal of the surface by oxidation of the silicon and subsequent oxide etching. The latter can be achieved by immersion in HF aqueous solutions. Examples of cleaning processes are the *RCA* process [67], or *Piranha* process among others [38]. In this work the cleaning has been performed by the following sequence based on HNO_3 oxidation and HF oxide removal at room temperature, unless the contrary is indicated:

- Deionised water rinse
- Oxidation in 69 %v/v HNO_3 (10 min)
- Deionised water rinse
- Oxide removal in 1 %v/v HF (1 min)
- Deionised water rinse
- Oxidation in 69 %v/v HNO_3 (10 min)
- Deionised water rinse

The cleaning process is carried out in the wet chemical bench described in Section 4.1.1, in Teflon basins. The wafers are hold in a Teflon wafer carrier with capacity for 25 100 x 100 mm^2 wafers. The wafers are dried in N_2 directly after the wet chemical cleaning process.

Emitter formation

The crystalline diffused solar cells produced in this work are p-type cells, i.e. realised on a p-type substrate with an n-type emitter. Therefore a phosphorous emitter is formed on the front side of the solar cells. The emitter formation consist, in this case, of a spin-on deposition of the phosphorous source on the wafers after a careful wet chemical cleaning, and subsequent thermal diffusion in an in-line furnace.

The phosphorous source is an aqueous solution containing H_3PO_4. In the spin-on process a few millilitres of this phosphorous source is deposited on the wafer, placed on a rotatory platform which holds the wafer by vacuum and rotates at up to 4000 rpm in the vertical axe. The phosphorous source drop deposited on the centre of the wafer spreads covering the wafer with a homogeneous thin layer.

After the spin-on coating the wafers are introduced in the in-line diffusion furnace. The diffusion furnace is equipped with a quartz channel and an optical tungsten halogen lamps heating system. The transport band of the furnace is made of ceramic strings to avoid contamination. The diffusion occurs in a controlled atmosphere, oxygen and nitrogen gases are introduced in the diffusion area of the furnace.

The diffusion process used in this work is a CFP (conventional furnace process) and is carried out at plateau temperatures from 800 to 900°C.

During the phosphorous diffusion a phosphorous silicate glass (PSG) is formed on the surface of the silicon wafers. The phosphoric acid, dried in the wafer surface lead to the formation of P_2O_5. This compound is reduced by silicon to SiO_2 and P, which is released and diffused into the silicon substrate [68]. The chemical reactions are shown below:

$$2H_3\mathrm{P}O_4 \leftrightarrow P_2\mathrm{O}_5 + 3H_2\mathrm{O} \quad (4.1)$$

$$2P_2\mathrm{O}_5 + 5Si \rightarrow 5Si\mathrm{O}_2 + 4\mathrm{P} \quad (4.2)$$

After the phosphorous diffusion the formed PSG should be removed from the silicon surface by means of 5 % v/v HF.

The phosphorous concentration profile in the emitter and its depth can be controlled by varying the temperature and time of the diffusion process. In this work the resulting emitter has in most of the cases a thickness of approximately 500 to 700 nm (as shown in Figure 4.3) and a sheet resistance about 50 Ω/sq.

In the literature, wide knowledge about diffusion processes and its mechanisms can be found [68, 69, 70].

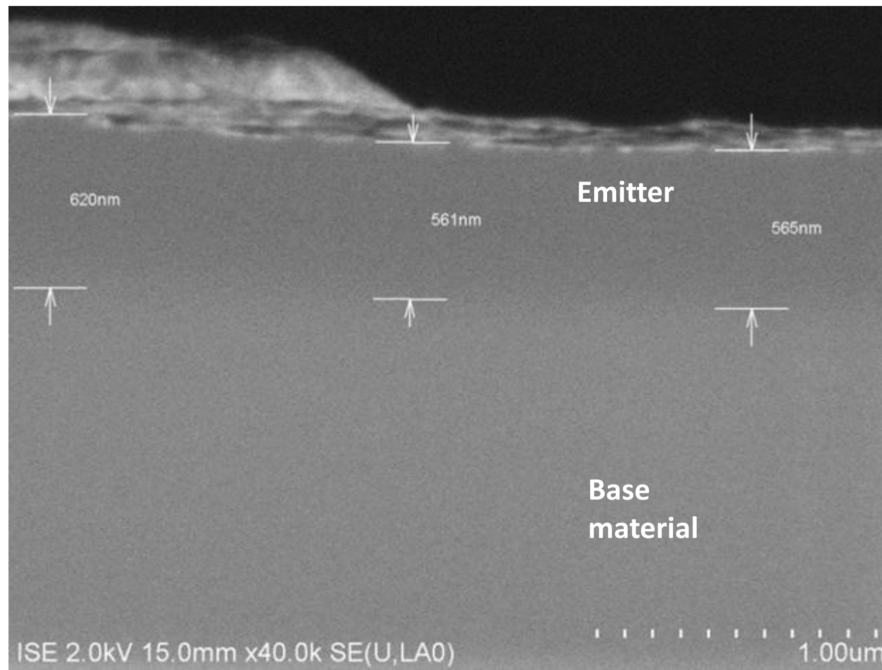

Figure 4.3. Doping contrast SEM image of the cross section of a saw damage etched wafer with phosphorous diffused emitter formed following the process described above. The emitter appears darker on the top part of the wafer.

Antireflection and passivation coating deposition

The most commonly used antireflection coatings (ARC) for solar cells are those based on thin dielectric layers which decrease reflectance by destructive interference. A minimum of reflectance at a given wavelength λ is achieved with odd multiple values of thickness:

$$d_{min} = \frac{\lambda}{4n_{ARC}} \tag{4.3}$$

In the case of solar cells, the ARC is designed to present the minimum of reflectance at 600 nm, as this is the wavelength at which the solar spectrum shows the higher photon intensity [8]. The refraction index of the ARC is also a parameter to be controlled. For solar cell production a refraction index of approximately 2.0 is the most appropriate taking into account the added effect of the encapsulation and the increase of absorption in the layer which would take place at higher refractive indexes [18]. Refraction indexes around 2.0 lead to antireflection layer thicknesses of 75-80 nm.

The most used ARC in crystalline silicon solar cell industry is hydrogenated amorphous silicon nitride (SiN_x). This material can be deposited on the silicon surface by several

methods, but the most common is the plasma enhanced chemical vapour deposition (PECVD) due to the following advantages over other chemical vapour deposition techniques: (i) lower deposition temperatures (under 500°C), (ii) higher deposition rate, (iii) possibility of varying the refractive index, and (iv) high concentration of hydrogen in the layers [18]. The principles of the PECVD technique can be found in the bibliography [41].

SiN_x presents not only adequate optical properties to be used as antireflection coating in solar cells but also appropriate passivation properties [71, 72]. Then, two main goals can be achieved in a single process step.

Regarding to the passivation features of SiN_x, it is able to perform both surface and bulk passivation [73, 74]. Due to a surface state defects decrease and the fix charges which induce a field passivation effect, surface passivation can be achieved by SiNx deposition. A bulk passivation is produced due to the hydrogen release from the layer to the silicon bulk [18] during the contact firing process.

In this work, the silicon nitride has been deposited using a one chamber direct PECVD system. The system consists on a parallel plate reactor which operates at 13.56 MHz. The plasma is generated by a radio frequency generator. An optical heating system allows temperatures up to 450°C. A base vacuum level of $3 \cdot 10^{-6}$ mbar is reached with a turbomolecular pump. The precursor gases are SiH_4, NH_3 and H_2. Details about the PECVD system employed to deposit the SiN_x layers and optical and passivation characteristics of the layers can be found elsewhere [75].

In the case of PECVD deposition on pyramidally textured silicon wafers, the deposition time has to be increased compared to standard non-textured surfaces due to the higher surface area of textured silicon, which result in a thinner thickness of the deposited layer. The deposition times in this work has been adjusted for textured cells by measuring the reflection wavelength dependent curve after the SiN_x deposition, until reaching the minimum reflection between 600 to 610 nm. It has been opted by this method as measurements by ellipsometry of the thickness and refraction index of the layers implies higher difficulties in textured surfaces compared to flat ones.

The PECVD deposition technique has been used in this work not only in the solar cell processing, but as well for the fabrication of *lifetime samples* with the aim of studying the surface recombination processes of the textured silicon. The lifetime samples are both side passivated FZ wafers after being submitted to a wet chemical cleaning. As passivation layer SiN_x and a-Si:H have been employed. For the a-Si:H intrinsic layer deposition SiH_4 is injected as precursor gas, in the same PECVD system described in this section, after a cleaning and conditioning of the system to avoid contamination of the layers. More details about the parameters of the amorphous silicon deposition can be found elsewhere [76].

Contact formation

After the SiN_x deposition, the ohmic contacts of the solar cell are performed. For this purpose a metal grid is placed on the front side and a continuous metal layer is deposited on the back side, as for industrial front emitter solar cells. The metallization can be manufactured by several techniques, but the most extended in the industry is the screen printing technology [8, 77]. The screen printing method is a thick film technique in which a metal *paste* is pressed and printed through a grid with the desired pattern. The paste contains micrometric metal particles, and additives as organic solvents and binders, and glass frit. The screen consists of a mesh of wires of steel or polyvinyl supported in a metallic frame. There is a micrometric film below the mesh which has opened areas that correspond to the desired pattern to print. The paste is deposited on the screen and pressed with a squeegee which passes with appropriate pressure from one side to the other of the screen. After the printing, a thermal process is carried out in order to dry the paste and to form the silicon-metal contact.

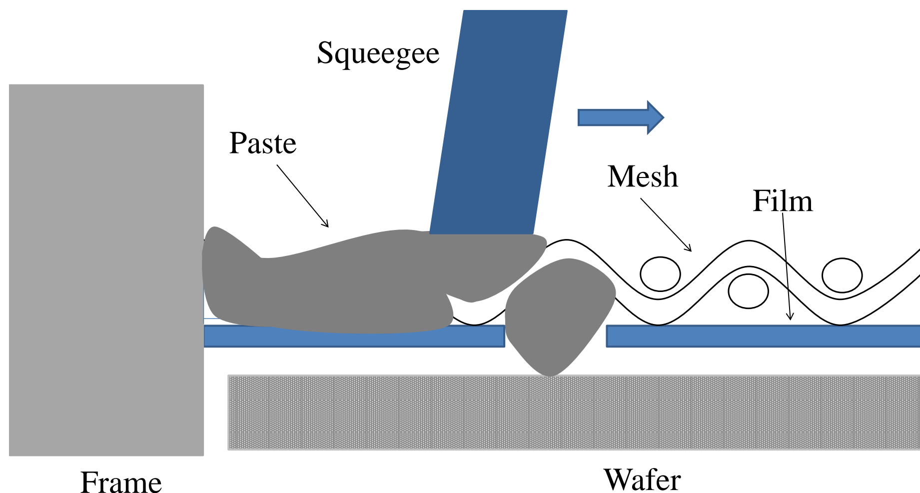

Figure 4.4. Schematic view of the screen printing working principle.

In p-type solar cells a silver paste is screen printed on the front side. The silver paste should form an ohmic contact with the n-emitter. The glass frit (commonly PbO_{Glass}) inside the paste etches the antireflection SiN_x coating to establish the contact of the silver conductor particles with the emitter [77]. This is the firing process, which takes place at maximum temperatures over 800°C to penetrate the ARC [8]. A model of the firing process is given in [78]: the solvents and organic components are burnt below 550°C, from 550 to 700°C the silver particles sinter, silver is dissolved in the glass and penetrates through the SiN_x layer over 625°C. Between 700 and 800°C the PbO_{Glass} etches the silicon by reduction and the epitaxial growth of silver crystals in silicon starts. During the cooling down, the silver and lead separate and the silver recrystallizes producing inverted pyramid crystallites.

The front side Ag-Si metallization occurs under the silver-silicon eutectic point (836°C) [77]. This is not the case of the formation of the backside Al-Si contact, which is formed by alloying at temperatures above the eutectic point 577°C [79]. Over this temperature an Al-Si alloy is formed. This occurs during the firing process. When the wafer temperature decreases, the silicon recrystallizes and the result is an Al doped silicon layer. In the aluminium back side metallization three important processes take place:

- Back contact formation
- Gettering of impurities in the Al rich layer, enhancing the bulk lifetime of the charge carriers
- Formation of a p+ layer which establishes a back surface field (BSF), reducing surface recombination

Furthermore the back metallization acts as a reflecting surface to enhance internal reflection and light trapping.

In this work a belt furnace with an optical heating system has been employed for the firing process. The sequence followed for the metallization process is the following:

- Silver screen printing of the front grid
- Drying in the belt furnace at 200-250 °C
- Back side screen printing with aluminium paste
- Firing process in the belt furnace at temperatures between 800 and 850°C

Edge isolation

During the phosphorous diffusion the dopant can diffuse over the edges of the wafer and reach the back side, which can produce short circuits. To avoid this problem the edges are cut away at the end of the solar cell process. The edge isolation can be carried out by etching processes, or by laser cutting. In this work, a laser beam is applied on the silicon edges at the rear side of the cell. Due to the high energy absorbed by the silicon the wafer melts locally. The laser penetrates in approximately a third of the wafer. After the laser process the wedges can be mechanically broken and, subsequently, the front and rear edges of the wafers remain electrically isolated from each other.

4.2 Characterization techniques

4.2.1 Materials characterization

Reflectance measurement and interpretation

Regarding to the purpose of silicon texturization, it is obvious that reflectance is one of the most important parameters to be evaluated, although it is not the only important parameter. Therefore, reflectance measurements can be considered as an appropriate method to test the performance of a texturization method or texturization step integrated on a process chain.

For measuring the reflectance of the textured silicon surface, a spectrophotometer with an integrating sphere has been used. The integrating sphere allows us not only to detect specular reflection but also diffuse reflection resulting from a microscopically rough surface. The result of this measurement is the wavelength dependent reflection of the silicon wafer.

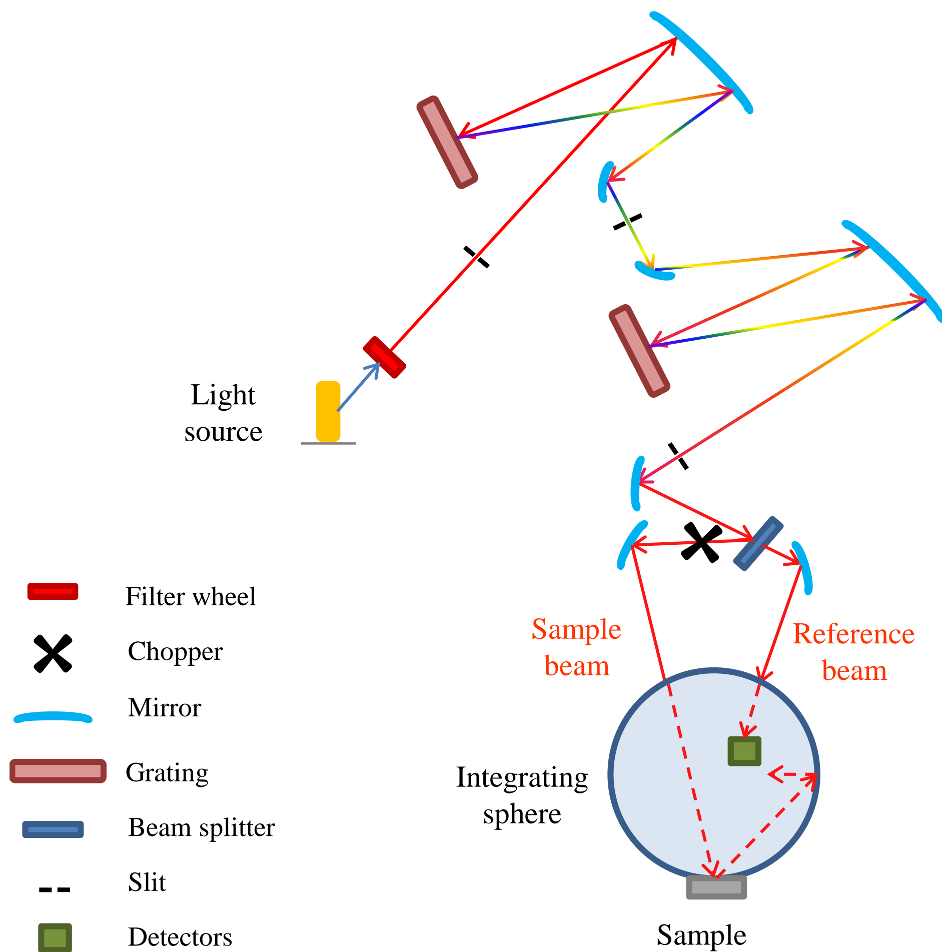

Figure 4.5. Basic scheme of the spectrophotometer.

The device used is a commercial spectrophotometer model Cary 500 from Varian Inc. able to operate in the UV-VIS-IR spectra. The dual beam device has a deuterium arc lamp for the UV range (up to 350 nm) and a tungsten halogen lamp for the VIS-IR range as light sources. A double monochromator system allows to measure reflectance and transmittance in the range from 175 to 3300 nm.

The system is equipped with an integrating sphere accessory model DRA-CA-50 from Labsphere, coated with Spectralon ™. The diameter of the sphere is 150 mm. The integrating sphere works in the range of 250 - 2500 nm. This accessory has two detectors placed inside of the sphere: a Si photodetector for the UV-VIS range and a PbS detector for the IR range. In Figure 4.5 the general scheme and the optical path of the device is depicted.

A splitter divides the main beam in the reference and the sample beams which, with the aid of a chopper, alternatively impinge on the detector. Then, the reflectance at certain wavelength is given by:

$$R\ (\lambda) = \frac{I_S(\lambda)}{I_R(\lambda)} \tag{4.4}$$

where $I_S(\lambda)$ is the intensity on the detector of the light reflected by the sample and $I_R(\lambda)$ the intensity of the reference beam.

In Figure 4.6 the result of the reflectance measurements of different initial substrates used in this thesis with the spectrophotometer are exposed. The error of the reflexion measurement is of the order of 1 % relative.

At about 360 nm a peak in the reflectance can be observed. This peak corresponds to the direct silicon transition at 3.4 eV [80]. However, the peaks observed at about 880 nm does not correspond to any physical feature in silicon absorption, but to noise in the detection due to the changeover of the silicon detector to the PbS detector.

Despite of the expected continuous decrease of reflectance with wavelength increase for silicon (Figure 3.1), it is observed a reflectance increase near 1000 nm. This is an effect of the back internal reflection of the silicon substrate. The photons with lower energies transmit the bulk silicon and are reflected backwards by the silicon back surface and transmitted again through the bulk silicon. A percentage of these photons will be able to exit the wafer without being absorbed or reflected once reached the front surface, and they will be detected. Depending on the wafer thickness and characteristics of the back and front surfaces this inflexion point will shift, and the slope of the raising curve will change. A thinner wafer with a back surface with higher internal reflectance will present a higher total reflectance at these long wavelengths.

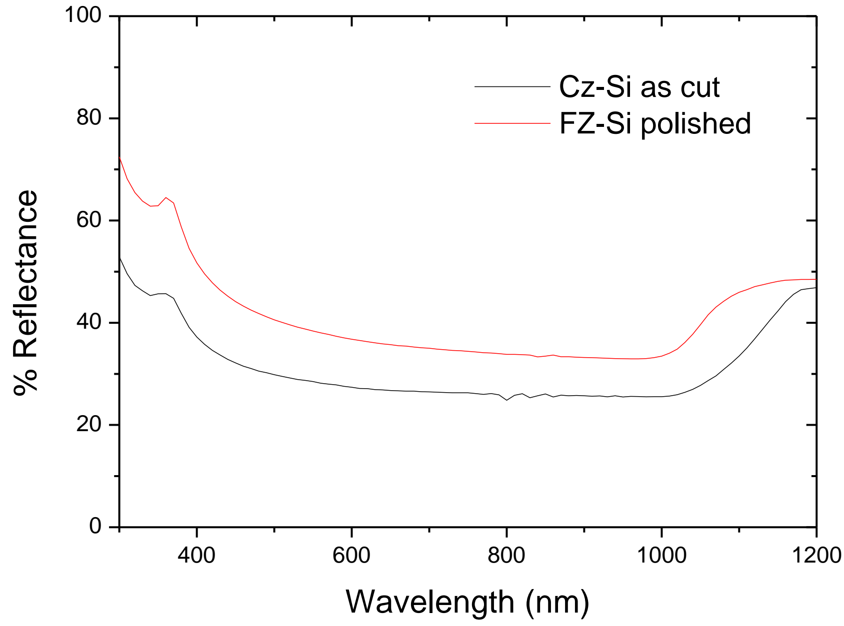

Figure 4.6. Reflectance measurement of different silicon substrates.

To evaluate the reflectance numerically, the standard weighted reflectance (*SWR*) in percentage is defined as:

$$SWR_{\lambda_1-\lambda_2} = \frac{\int_{\lambda_1}^{\lambda_2} R(\lambda)SE(\lambda)d\lambda}{\int_{\lambda_1}^{\lambda_2} SE(\lambda)d\lambda} \tag{4.5}$$

where $R(\lambda)$ is the measured reflectance in percentage and $SE(\lambda)$ is the wavelength dependent intensity of the solar spectrum AM 1.5G. Thus, in a given wavelength range, the reflectance is evaluated weighting itself with the solar spectrum intensity at every wavelength, which describes more properly the available solar photons that can be absorbed in solar cells, and offers a single reflectance value that can be used for comparing different substrates.

The *SWR* is calculated in this thesis over two different wavelength ranges, which gives the values $SWR_{400\text{-}900}$ and $SWR_{400\text{-}1100}$.

The lower limit of the chosen wavelength range (400 nm) is selected attending to the highest photon energy typically converted (above this photon energy the spectral response of silicon based diffused solar cells decrease due to thermalization losses and high recombination in the emitter). The upper limit of 1100 nm corresponds to the lower photon energy able to be absorbed by silicon, giving the value $SWR_{400\text{-}1100}$ a general idea of total reflectance. The limit of 900 nm is chosen as the upper limit of the range in which the front surface reflectance is dominant and the back reflectance is playing a second role (i.e. for the case of silicon wafers with commercial thicknesses between

150- 250 μm). Thus, this value represents the surface front reflectance of the wafer or cell.

If the opposite is not indicated, the textured wafers described in this thesis are measured without any coating or back reflector.

Scanning electron microscopy

The scanning electron microscopy (SEM) is a technique that allows determining the surface morphology and elemental composition of solid samples. A focused electron beam (primary electrons) scans the sample surface and secondary electrons are detected in order to project a topographic image of the sample surface. The yield of secondary electrons at each scanned position determines the spot brightness in a cathode ray display tube. Backscattered and Auger electrons, and X-ray emission are also produced and can be detected with the appropriate detection system, and give also chemical information. Detailed information about SEM principles can be found elsewhere [81].

In this work we have analysed the topography of most of the samples by means of secondary electron detection with a SEM device JEOL JSM 6300 with 3.5 nm spatial resolution. The images where obtained at 45° in most of the cases, or at 0° tilt angle of the sample surface. As well, the EDX technique (energy-dispersive X-ray spectroscopy) has being applied with an Oxford Instruments Microanalysis Group 6699 ATW in order to determine the elemental composition of the sample surfaces.

The cross section images of chapter 7 have been achieved by means of an ultra-high resolution FE-SEM (field emission scanning electron microscopy) model SU-70 from Hitachi with semi-in-lens technology. The FE-SEM provides higher resolution at lower acceleration voltages of the electron beam, avoiding charging effects. This technique is more appropriate than conventional SEM for analysis of semiconductors cross sections and thin layers. Principles of FE-SEM microscopy can be consulted elsewhere [82, 83].

Atomic force microscopy

To measure the surface roughness of the silicon samples studied in this thesis, an Atomic Force Microscopy (AFM) device has been used to obtain topographic maps where the heights of the morphologic features present on the silicon surface are scanned through x-y directions.

AFM is one of the multiple existing scanning probe methods, where a probe consisting in a sharp tip placed at some nanometres from the sample scan the surface of the latter. When the tip is sufficiently close to the sample surface, van der Waals attractive or repulsive forces act between them, making the cantilever in which the probe is attached to change its deflection angle or to oscillate. These variations in deflection angles or oscillations are recorded and computed to obtain images of the surfaces scanned. The size of the tip is of the order of micrometres. The principle of the AFM technique is illustrated below.

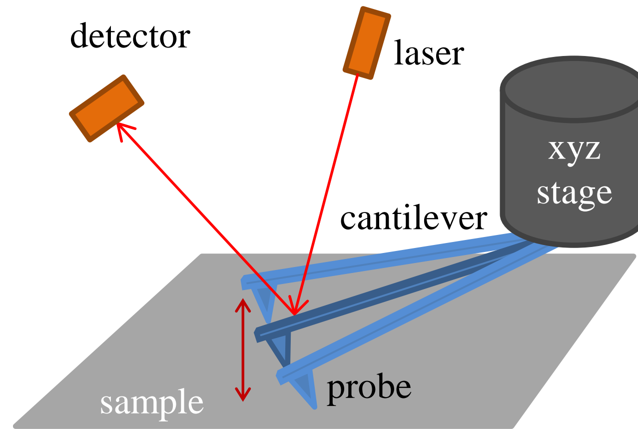

Figure 4.7. Basic scheme of AFM

The AFM can operate in contact or non-contact modes depending on whether the probe touches directly the surface of the sample or it is kept at a nanometric distance between them, oscillating the probe close to its resonance frequency. In the first case, the deflection of the cantilever caused by the morphology of the sample is detected and in the second the change in the oscillation frequency is detected.

The topographies shown in this work have been recorded in the Dynamic Force Mode (DFM) (unless the opposite is specified), also known as *tapping mode*, with a Digital Instruments Nanoscope IIIa device. In the tapping mode the probe oscillates, as in the non-contact mode, but with higher frequency and closer to the sample, intermittently touching the surface.

The AFM technique has been used in this thesis more for determining the surface nanoroughness, than as a technique for determining the microscopic morphology (e.g. to solve the pyramids images). The aspect ratio of pyramids shapes an abrupt morphology that makes the measurement difficult. Even it is easy that the tip probes break during the measurement. Therefore, for the resolution needed to solve the pyramids, the SEM technique is more appropriate, as it can be as well observed from the images shown in Figure 4.8, which shows the surface of the same textured sample imaged by AFM and SEM. The AFM has also been used in this work to analyse the pyramid formation at their very initial stage, in which they present still nanometric size, being more difficult to be observed by SEM, due to its lower resolution.

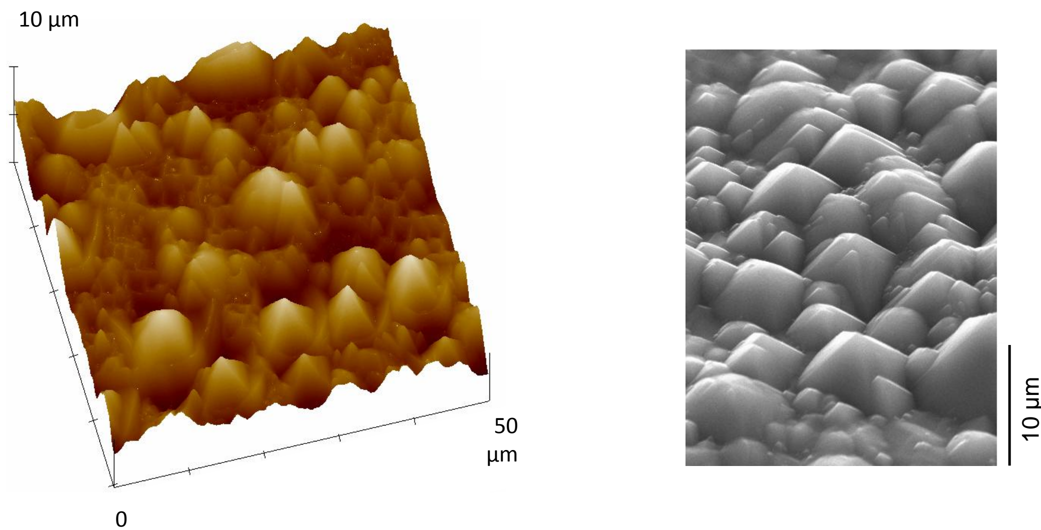

Figure 4.8. Comparison of microscopic images of pyramids obtained by AFM (left)[6] and SEM (right).

To determine the nanoroughness on the {111} oriented walls of the pyramids, the common procedure is to simulate the process performing a texturization on flat {111} wafers that are subsequently analysed by AFM. The high steps that pyramids present on a textured wafer, when a nanometric resolution by AFM is aimed, would not disturb the measurement. In this thesis, in contrast, it has been opted for measuring directly on the pyramid walls. This method is more accurate since the pyramid facets are not exact {111} but near {111} planes. The results of this measurement procedure can be consulted in chapters 5 and 7, and in reference [84].

The samples were cleaned from particles and dirtiness in an ultrasonic bath previously to the microscopic analysis to avoid interferences in the measurement. The AFM data have been analysed with the software WSXM [85] and the software NanoScope version 5.12 from Digital Instruments.

Lifetime measurement

The lifetime of the photogenerated minority carriers can be evaluated by means of transient photoconductance decay (PCD). In dark conditions, a semiconductor is in equilibrium, with a given concentration of charge carriers. Under illumination an excess of charge carriers is generated (minority and majority excess carriers), and when the illumination is ceased, and the photogeneration stopped, the charge carrier concentration decreases again to its equilibrium values through recombination. This process modifies the conductance of the sample on the time scale. This decay of the conductance with time is measured and from it, the lifetime of the excess charge carriers can be calculated [86].

[6] Image obtained in the contact mode.

There exists another approximation to calculate the carrier lifetime by measuring the photoconductance: the quasi-steady-state photoconductance (QSSPC) [87]. In the steady-state illumination conditions, the generation of charge carriers G and the recombination rate U are balanced, leading to:

$$G = \frac{\Delta n}{\tau} \tag{4.6}$$

where τ is the effective lifetime and Δn is the excess minority carrier density. Under quasi-steady-state illumination (the light pulse varies very slowly compared to the lifetime of the sample) and with a photodetector, the generation can be determined and the excess carrier density calculated from the photoconductance measured, in order to determine the lifetime [87].

In this thesis two devices/methods have been used in order to measure the minority carrier lifetime: microwave photoconductance decay (µW-PCD) and quasi-steady-state photoconductance (QSSPC).

The µW-PCD is a transient decay technique and it is based on the different reflection of microwaves depending on the conductivity of a given sample. In a µW-PCD set-up, microwaves are generated, directed to the sample through a circulator and the reflected waves are directed again through the circulator to a detector [86]. The µW-PCD device used in this work is the model WT-2000 from Semilab. The photogeneration of carriers is induced by a laser pulse of 904 nm. The sample wafer is scanned, and after the measurement a lifetime map is generated. The measurements of this work are performed with a laser intensity of $1.5 \cdot 10^{12}$ photons per laser pulse and under a bias light of 0.5 Sun in order to avoid injection-level dependency effects [88]. It should be taken into account that the effective lifetime measured by this technique is a differential lifetime [88], contrary to the QSSPC method, which displays an absolute value.

The used QSSPC device is a WTC-120 from Sinton Consulting Inc. in which a flash lamp is used as a light source to induce photogeneration. The conductivity is measured over the time by a RF coil inductively coupled to the sample and the light intensity measured by a calibrated photodiode. One of the advantages of this technique is that a plot of the effective minority carrier lifetime over the injection level is obtained within one measurement. This is not possible with the µW-PCD analysis.

The WCT-120 can operate in either transient or quasi-steady-state mode by varying the time of the flash pulse. The choice of the mode obeys to the expected lifetime of the samples [87]. The transient mode is accurate for effective minority carrier lifetimes above 100 µs, and for minority carrier lifetimes below 200 µs the QSS analysis would be the appropriate [89]. In the case of the QSS mode, as the generation should be known, a parameter called optical constant or absorption fraction f_{abs} should be introduced in the calculation [90]. Therefore the generation will be:

$$G = \frac{N_{ph} f_{abs}}{W} \tag{4.7}$$

where N_{ph} is the photon flux per unit area measured in the detector and W the wafer thickness.

Cuevas et al. propose the following approximated values shown in Table 4.2 for f_{abs}, and state an error under 5% associated to the determination of this value [90].

Table 4.2. Approximated f_{abs} values after Cuevas et al. [90].

Front surface	f_{abs}
Polished Si	0.6
Optimized ARC	0.9
Textured Si + Optimized ARC	1

Sheet resistance measurement

After the phosphorous diffusion sheet resistance measurements are performed to evaluate the quality of the emitter. The sheet resistance is an expression of resistance independent on the material thickness.

Given a rectangular layer of resistivity ρ, dimensions L_1 x L_2 and thickness W, the resistance is calculated as follows:

$$R = \frac{\rho}{W} \frac{L_1}{L_2} \tag{4.8}$$

And the sheet resistance is defined as:

$$R_{Sh} = \frac{\rho}{W} \tag{4.9}$$

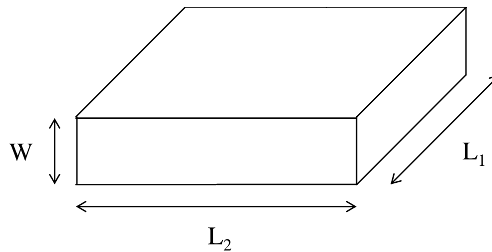

Figure 4.9. Dimensions implied in the calculation of sheet resistance in a sheet of resistivity ρ. The current flows parallel to the plane given by L_1 and L_2 dimensions.

The sheet resistance is expressed in ohm/square (ohm/sq).

The measurement of sheet resistance is performed by the four-point probe technique, in which four equidistant tips contact the sample (Figure 4.10). A current flows between the two outer tips and the voltage is measured between the other two inner tips.

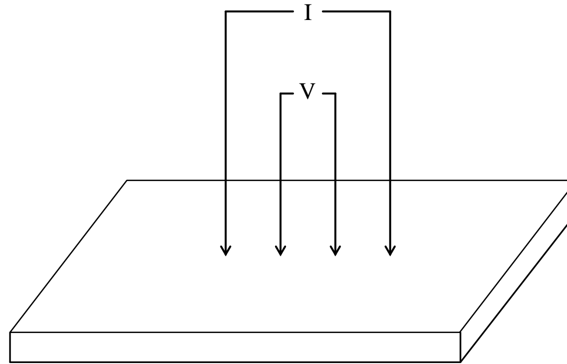

Figure 4.10. Four-point probe measurement scheme.

For the condition $s>>W$ (being s the distance between the tips), which is the case of shallow layers, as the diffused emitter:

$$R_{Sh} = \frac{\pi}{ln2}\frac{V}{I} = 4.532\frac{V}{I} \quad (4.10)$$

From the current density, the voltage and a geometric correction factor, the sheet resistance can be calculated [91].

In this work, automatized measurements have been performed by a four-point probe device which maps the wafer surface measuring at different points. After the measurement a map of the sheet resistance values over the wafer surface is obtained. This gives an idea of the homogeneity of the emitter, and the suitability of the sheet resistance average value for solar cell production.

4.2.2 Solar cell characterization

I-V measurement

The current-voltage curve has been measured in dark conditions and under illumination to extract the characteristic parameters of the solar cells I_{SC}, V_{OC}, R_P, R_S, FF, Eff, etc. (see Section 2.4). Current-voltage pairs of values are measured with the help of a power supply and two multimeters. The measurement is controlled by a computer equipped with a data acquisition system.

The measurements are performed under standard conditions: AM1.5G spectrum (light intensity of 1000W/m^2) and 25°C. The cell is placed in a temperature controlled block.

For the illuminated measurements, a Xe lamp solar simulator from Wacom model WXS-150S-10.AM1.5G which provides AM1.5G irradiance is used.

The measurements are calibrated by adjusting the irradiance and the temperature to reach the short circuit current and the open circuit voltage of a reference solar cell.

External quantum efficiency

To perform the wavelength dependent external quantum efficiency (*EQE*) measurements, light selected in different spectral ranges by a monochromator is chopped and focused on the samples. The current from the solar cell is converted to voltage and measured with a lock-in amplifier. From the value of *EQE* and the reflectance of the cells, the internal quantum efficiency (*IQE*) can be calculated (See Equation 2.20).

As a light source xenon and tungsten lamps are used. The sample can be illuminated by bias light during the measurements.

CELLO

The CELLO (Solar Cell Local Characterization) technique is a measurement technique based on the local measurement of electric parameters of a near one sun illuminated solar cell under local laser perturbations [92]. A potentiostat/galvanostat sets the voltage or the current of the solar cell at the desired working point and the response of the solar cell (intensity or voltage) to the sinusoidally modulated laser beam is measured by a lock-in amplifier. Fitting the measurement data to the model proposed by Carstensen et al. [92, 93], several parameters of the solar cell as the series [94] and shunt resistance, or local recombination characteristics can be determined.

5 Optimization of the $Na_2CO_3/NaHCO_3$ process for texturization of (100) silicon

In this chapter a new ultra-low concentration $Na_2CO_3/NaHCO_3$ solution for texturing (100) silicon is developed. After investigating the performance of the texturization based on this proposed solution, the process has been scaled up and the parameters of the reaction have been optimized. Fundamental aspects regarding to the texturization with the new ultra-low concentration solution, as the influence of silicon material and surface and the influence of temperature on the texturization result, have also been studied.

5.1 Influence of chemicals concentration. Towards an ultra-low concentration $Na_2CO_3/NaHCO_3$ solution for silicon texturization

The use of the $Na_2CO_3/NaHCO_3$ solution for silicon texturization with the optimum concentration which was previously established in the literature, presents certain disadvantages due to the high concentration of the solutes. The 20 wt% Na_2CO_3 / 4 wt% $NaHCO_3$ concentrated solution proposed by Marrero et al. [10] presents the following problems, which has been observed in the laboratory:

(i) Precipitation of the carbonate and bicarbonate salts in the reactor system has been observed, which could be a big disadvantage for industrial implementation of the process regarding to cleaning of the system and possible obstruction of valves and tubes by the precipitated salts. The solution is saturated at 20 °C, since the solubility of sodium carbonate in aqueous solution at 20 °C is 17.9 wt% [95] (the aqueous solubility is over 23 wt% at temperatures over 25°C, allowing the salt to be dissolved at the process temperature, 95 °C).

(ii) The high temperature of the process (95 °C) [10] produces a high evaporation rate of the solution, and the evaporated water also carries part of the solute. Both facts lead to inconstant concentration of the solution. The salts carried by the evaporated solution precipitates at the reactor walls and within the chemical bench. This would be also a disadvantage for industrial application, since the control of the process would be affected.

(iii) The two effects exposed above have a consequence: the solution cannot be used more than once. It has been observed that after performing a texturization of four to six 100 cm^2 Cz wafers with the 20 wt% Na_2CO_3 / 4 wt% $NaHCO_3$ solution at laboratory scale (4 l of reaction solution), the reuse of the same solution to texture new wafers produce different results,

regarding to the reflectance obtained. An experiment done with 100 cm^2 Cz wafers with the 20 wt% Na_2CO_3 / 4 wt% $NaHCO_3$ solution, at 95 °C during 20 minutes give as a result a value of 20.2 % $SWR_{400-900}$. After repeating the experiment in the same solution the result obtained is 22.5 % $SWR_{400-900}$, significantly higher.

Due to the above mentioned problems, a new approach to the process is needed. Therefore, in this work, the concentration of chemicals of the Na_2CO_3/$NaHCO_3$ solution has been decreased, which has also the advantage of decreasing costs.

The optimal concentration values encountered in the bibliography for carbonate-based solutions are in the range of 12 % [61] to 25 % [63] of sodium carbonate. Vallejo et al. have also proposed a 5 wt% carbonate solution [63], but they claim that the resulting homogeneity of the textured surface is not adequate and the required reaction time is long.

Based on the buffering nature[7] of carbonate/bicarbonate solutions, the concentration of the Na_2CO_3/$NaHCO_3$ pair has been lowered in this thesis and the effectiveness of the proposed and so called ultra-low concentration Na_2CO_3/$NaHCO_3$ solution has been proved. The proposed ultra-low concentration solution consists of 1% Na_2CO_3 and 0.2% $NaHCO_3$ in deionised water. The concentration of the chemicals in the solution is far below the saturation value mentioned before.

As discussed in chapter 3.4, not only OH^- ions but water molecules are of key importance in the etching reaction of silicon in alkaline solutions. After Seidel et al. [57], only the OH^- formed from water hydrolysis, and not the OH^- from the bulk solution react with the silicon. On the other hand, Allongue et al. [60] claim in their chemical model that water molecules are the only reactants while OH^- ions act only as catalysers. Taking this into account, the importance of initial concentration of OH^- ions in the solution, and therefore the pH, can be considered relative. Seidel mentions as an example of the higher importance of water concentration with respect to OH^- concentration the small difference of the silicon etch rates between EDP and KOH solutions, although OH^- ion concentration is more than 100 times higher for KOH solutions [96].

Furthermore, the buffering character of the Na_2CO_3/$NaHCO_3$ system allows us to drastically decrease the concentration without producing a high drop of the pH value. Thus, for a 20 wt% Na_2CO_3 / 4 wt% $NaHCO_3$ solution the calculated pH at 25 °C is 11.7 and for a 1 wt% Na_2CO_3 / 0.2 wt% $NaHCO_3$ solution the pH value is 10.5.

Another interesting fact is that Schnakenberg et al. [97] observed an increase in the anisotropy ratio (measured as the (100) plane etch rate/ (111) plane etch rate) when the

[7] A buffer solution is an aqueous mixture of a weak base with its conjugated acid (or a weak acid with its conjugated base) in equilibrium, showing no high changes in pH with small additions of acids or bases.

pH of TMAHW solutions was decreased, with a subsequent increase of pyramid formation, which support that a change in pH is not necessarily detrimental for pyramid formation in alkaline solutions.

All the facts mentioned above lead us to the conclusion that decreasing the Na_2CO_3 and $NaHCO_3$ concentration in the solution should be possible. In this work, this has been demonstrated and the morphological and optical results of the textured silicon surface with the proposed ultra-low concentration solution have been studied.

In order to prove the hypothesis, a texturing experiment has been carried out in the 4 l laboratory-scale system. The temperature of the experiment was set to 90 °C, since at 95 °C a high evaporation rate of the solution is observed and the control of the process is therefore affected. The Na_2CO_3/$NaHCO_3$ solutions compared in this chapter are named as follows:

- **Solution S20/4**: 20 wt% Na_2CO_3 / 4 wt% $NaHCO_3$ solution.
- **Solution S1/0.2**: 1 wt% Na_2CO_3 / 0.2 wt% $NaHCO_3$ solution.

A microscopic inspection of the wafers textured with the two solutions for 20 minutes reveals big differences in the morphology obtained (Figure 5.1). The surface of the wafer textured with the new ultra-low concentration solution presents smaller and more regular and sharpened pyramids compared to the S20/4 solution. Despite of the optical advantage of this fact, which leads to a lower reflectance (see Figure 5.2), a silicon surface with smaller pyramids is more suitable for the subsequent solar cell processing steps, as it is further discussed in chapter 7. The pyramids formed with the solution S20/4 have an average size of 10 µm width and 3 µm height, while the pyramids formed with the solution S1/0.2 are 4 µm wide and less than 2 µm high.

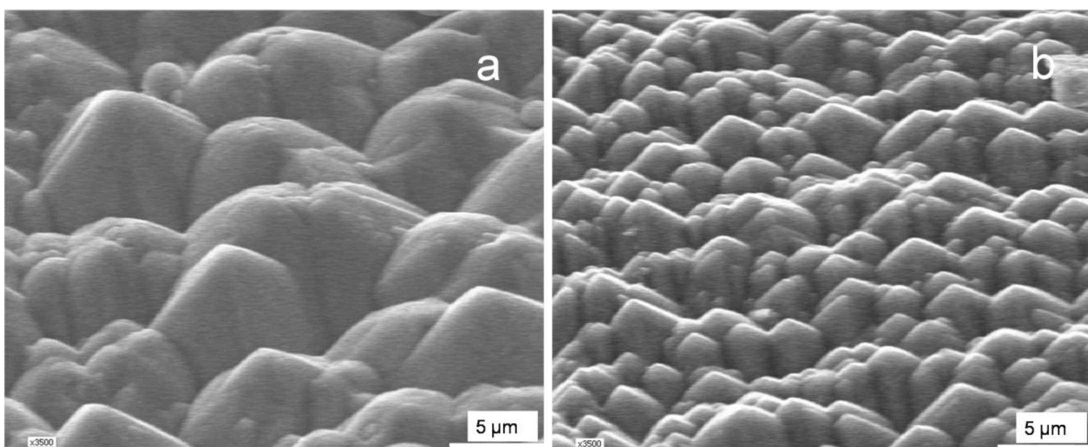

Figure 5.1. SEM images of p-Cz wafers textured during 20 minutes with a) solution S20/4; b) S1/0.2.

The average etching rates of the solutions for a reaction time of 20 min were 0.57 µm/min/side for the solution S20/4, and 0.39 µm/min/side for the solution S1/0.2.

In Figure 5.2 the reflectance spectra of as cut p-Cz wafers textured with the solutions S20/4 (20 minutes of reaction time) and S1/0.2 (20 and 30 minutes) are depicted.

For the same texturing time (20 minutes), the ultra-low concentration solution S1/0.2 results in a lower reflectance (19.5 % $SWR_{400\text{-}1100}$) than the concentrated solution S20/4 (23.0 % $SWR_{400\text{-}1100}$). A value of 11.6 % $SWR_{400\text{-}1100}$ can be achieved with the solution S1/0.2 after 30 minutes of texturing time. It should be noticed that for the 20 minutes processes, the difference in the reflectance spectra for the two different solutions (S1/0.2 and S20/4) is higher for the shorter wavelengths, while at long wavelengths the difference is very small. This means that the improvement is mainly due to the decrease of front reflection. However, for the 30 minutes process with solution S1/0.2 the back reflection is also significantly decreased, pointing in this case also to a light trapping enhancement.

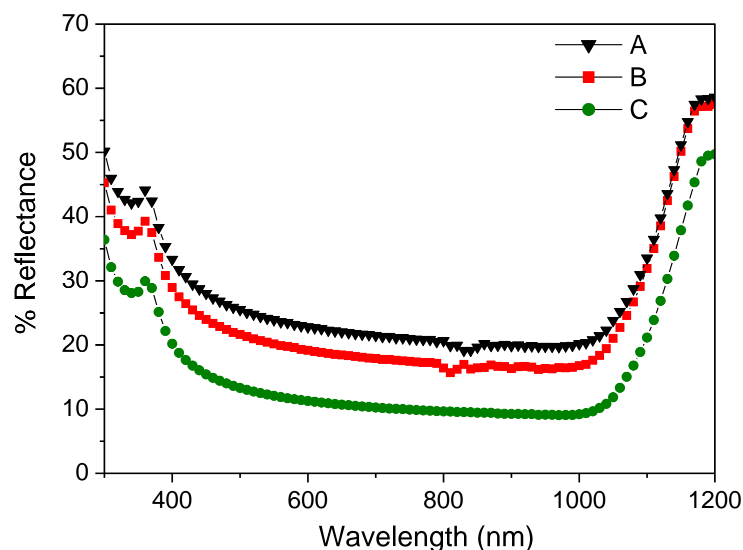

Figure 5.2. Reflectance spectra of p-Cz wafers textured at 90 °C with A) solution S20/4 for 20 min.; B) solution S1/0.2 for 20 min. and C) solution S1/0.2 for 30 min.

In order to prove the suitability of the S1/0.2 solution for the texturization of different (100) silicon materials, the solution was tested with silicon samples with different characteristics (growing method, doping type, surface pre-treatment). The reaction was carried out at 90°C in the 4 litres set-up, and the wafers were cut in samples of 16 cm^2. The characteristics of the wafers and the etching rate and reflectance results after the texturization process are summarized in Table 5.1. The reflectance in Table 5.1 is expressed as $SWR_{400\text{-}900}$, corresponding mainly to the front reflection, in order to compare the surfaces, since the different thickness of the wafers affects the back internal reflection, and therefore the value of $SWR_{400\text{-}1100}$. The front reflectance is significantly lowered for the 30 minutes reaction for all the silicon materials tested. For the n-type Cz as cut silicon the reflectance is higher than for the p-Cz and the FZ textured wafers. The etching rate for the n-Cz sample is lower than for the rest of the samples.

Table 5.1. Etching rate and $SWR_{400-900}$ for different Si (100) wafers textured with the S1/0.2 solution during 30 min.

Wafer type	Resistivity (Ω·cm)	Etching rate (µm/min/side)	% $SWR_{400-900}$
p-FZ shiny etched	0.8-1.2	0.26	12.1
n-FZ shiny etched	0.8-1.2	0.27	11.8
p-Cz as cut	1.0-3.0	0.32	11.7
n-Cz as cut	1.0-3.0	0.23	13.0

In Figure 5.3 the SEM images of the different wafer types textured with solution S1/0.2 with a reaction time of 30 minutes are shown. As observed, there is a good and homogeneous coverage of the surface by pyramids. The final morphology of the surface is very similar for FZ p- and n-type and for p-Cz (Figure 5.3 a, c and d), with pyramids with a base diameter of 2.5-7.5 µm and height of 1.5-5.0 µm approximately.

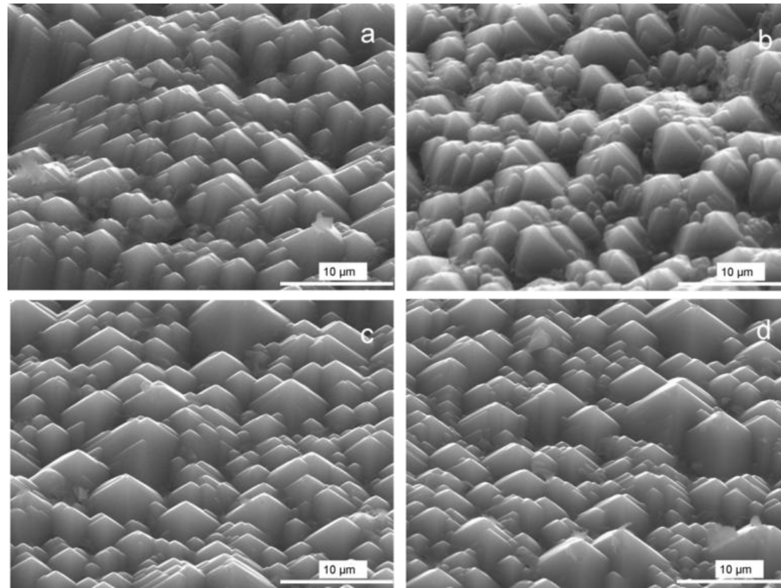

Figure 5.3. SEM images (3500x) of different silicon wafers textured during 30 min. with S1/0.2 solution. a) p-Cz; b) n-Cz; c) p-FZ and d) n-FZ.

The pyramids of the samples textured during 30 minutes are sharper than for the 20 minutes textured samples (see Figure 5.1), what can be the explanation for the lower reflection exhibited by the 30 minutes textured samples with the S1/0.2 solution. The surface morphology of the textured n-Cz wafer (Figure 5.3 b) differs from the morphology of the other wafers. The n-Cz silicon shows a more irregular morphology, with pyramids with less homogenously distributed sizes, resulting in a higher front

surface reflectance than the p-Cz and FZ samples. The parameters of the reaction should be adjusted for this type of substrate. The reason for this different result can be attributed to the different surface properties of this substrate (e.g. surface states, initial defects, etc.) which is supposed to influence the etching rate [54]. The influence of the initial surface conditions of the wafers is further discussed in section 5.2. In general, the results exposed above show that the proposed new ultra-low concentration S1/0.2 solution is suitable to texture different silicon wafer types with satisfactory results regarding to reflectance and surface morphology.

Another advantage of the new S1/0.2 solution compared to the S20/4 solution is the lower nanoroughness observed in the samples textured with the solution S1/0.2, as it is shown in Figure 5.4 a and b. The nanoroughness of the textured samples was determined by means of AFM direct measurements on the walls of the pyramids formed in p-Cz silicon with solutions S1/0.2 and S20/4. This is important to notice, as a common method is to apply the texturization process parallel on (111) wafers and measure the nanoroughness by AFM on these (111) wafers, but this is not exactly representative of what occurs on the pyramid facets as they are in fact near {111} planes, which responds to the anisotropic texturization processes differently than exact {111} surfaces. A lower nanoroughness of the surface is beneficial for solar cell performance, since a lower nanoroughness result in a lower surface recombination of minority charge carriers [66].

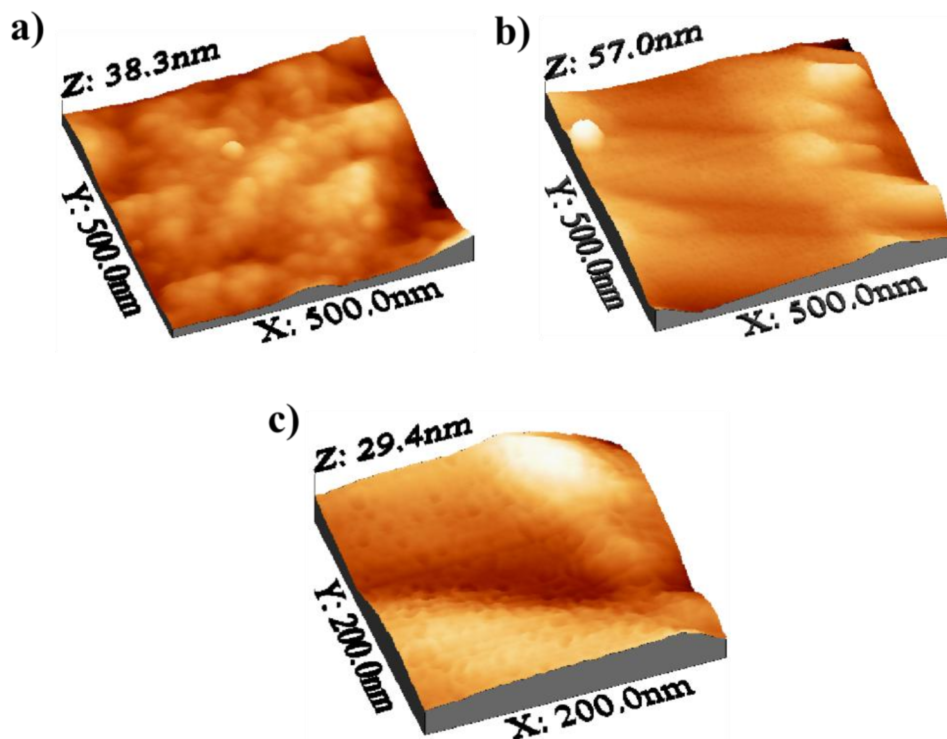

Figure 5.4. AFM images of the walls of the pyramids formed by texturization with a) S20/4 solution; b) and c) S1/0.2 solution. The proportion between the Z scale and the X-Y scale has been kept in order to show the surface with the real aspect ratio.

A closer inspection of the wafers textured with the S1/0.2 solution (Figure 5.4 c), shows that in the pyramid walls there exist nanometric pits with a diameter of about 5 nm and a depth of about 2 nm. The surface textured with the S1/0.2 solution shows features with anisotropic aspect at nanometric size on the walls of the pyramids. This can be caused by the lower etching rate at which the texturization occurs for the solution S1/0.2 compared to S20/4, since lower concentrations of OH^- ions and therefore lower etching rates are related to a higher anisotropic effect [57, 97].

In summary, the low reflectance and the morphology obtained in the different substrates show that the S1/0.2 solution is suitable to be implemented in the texturization process for solar cell production, having on the other hand benefits with respect to process implementation and costs due to the 20 times lower content of chemicals than the S20/4 solution [10] and 12 times lower content of chemical that the optimum found in the literature [61]. As the experiments have been realized in the 4 l set-up, the performance of the solution S1/0.2 for texturization must be proved in a texturing bath of bigger volume, and also the possibility of reusing the solution should be proved. These aspects are treated in section 5.4.

5.2 Influence of the initial surface roughness of the silicon wafers

Some authors have indicated the higher difficulty of texturing polished silicon surfaces compared to as cut surfaces and point out the role of the initial surface conditions of the silicon in texturization processes with alkaline solutions [98, 99]. For NaOH/IPA texturization a longer etching time is required, and the morphology obtained differs for polished wafers compared to as cut wafers [99].

To study the influence of the wafer initial surface on the texturization result with S1/0.2 solution, different substrates with different surfaces have been analysed by AFM to characterize the initial surface roughness. After being textured under the same conditions, the morphology and surface reflectance and the etching rate of the texturization process of these samples were analysed.

The silicon wafers analysed for this purpose were both n- and p-type as cut Cz Si and shiny etched FZ Si, cut into pieces of 16 cm^2. Two sets of four different wafers have been textured with the S1/0.2 solution during 30 minutes at 90 °C. One of the sets consisted on the mentioned above Cz and FZ samples submitted only to a HF dip previously to the texturization to remove the native oxide layer. The second set of the Cz and FZ samples was immersed in a 30 wt% NaOH aqueous solution at 83 °C during 1.5 minutes, and afterwards submitted to the HF dip before being textured. The aim of the NaOH pre-treatment is to modify the surface of the samples and etch the first micrometres of their original surface. By means of the NaOH pre-treatment, 2.3 µm/side were removed for p- and n- shiny etched FZ Si, and 3.1 µm/side for n-Cz Si and 3.8 for p-Cz Si. A resume of the characteristics of the samples processed are shown in Table 5.2. Both sets of samples were simultaneously textured in the 4 l laboratory-scale set-up.

Table 5.2. Characteristics and pre-treatment of the samples textured with the S1/0.2 solution to investigate the influence of the initial surface roughness.

Set 1 **No NaOH pre-treatment**	Set 2 **NaOH pre-treatment**
p-FZ Si shiny etched	p-FZ Si shiny etched
n-FZ Si shiny etched	n-FZ Si shiny etched
p-Cz Si as cut	p-Cz Si as cut
n-Cz Si as cut	n-Cz Si as cut

The initial surface of the samples with and without NaOH pre-treatment, characterized by AFM, and the SEM images of the final surface pyramidal morphology obtained by the texturization are shown in Figure 5.5 and Figure 5.6. Regarding to the initial surface of the wafers without NaOH pre-treatment (Figure 5.5) it can be observed that the FZ shiny etched wafers (Figure 5.5 e and g) are relatively flat while the as cut Cz wafers (Figure 5.5 a and c) present a rougher and more defected surface, as expected. After the NaOH pre-treatment (Figure 5.6), only the p-Cz as cut sample is smoothed (Figure 5.6 a), while in the as cut n-Cz sample (Figure 5.6 c) and in the shiny etched FZ samples (Figure 5.6 e and g) defects and steps are induced by the NaOH pre-treatment. The SEM images in Figure 5.5 and Figure 5.6 show that in all cases, with and without NaOH pre-treatment, the surface is totally covered by pyramids. There exists no difference for the final morphology of the FZ samples treated with (Figure 5.6) and without (Figure 5.5) NaOH. In the case of p-Cz the surface appear slightly more irregular with pyramids of different sizes for the NaOH pre-treated sample (Figure 5.6 a) than for the non-treated p-Cz sample (Figure 5.5 a). The opposite is observed for n-Cz, in which the homogeneity of pyramid size is enhanced by the NaOH pre-treatment (Figure 5.6 c).

The only significant changes in the final $SWR_{400\text{-}900}$ (Table 5.3) to be noticed are the reflection decrease of the textured n-Cz surface and the p-FZ surface when the wafers are treated previously with NaOH. The etching rate of the n-Cz sample is increased for the case of previous NaOH immersion compared to the non-NaOH treated sample. Furthermore, the n-Cz textured surface presents pyramids more homogenously distributed in size for the NaOH treated sample (Figure 5.6 d), which can be the reason for the lower reflectance compared to the n-Cz sample without NaOH treatment (Figure 5.5 d). In the case of the p-FZ, attending to the SEM images of the textured surfaces, almost no difference is appreciated with and without the NaOH pre-treatment, except the presence of some slightly larger pyramids in the p-FZ wafer without NaOH pre-treatment (see Figure 5.5 f and Figure 5.6 f).

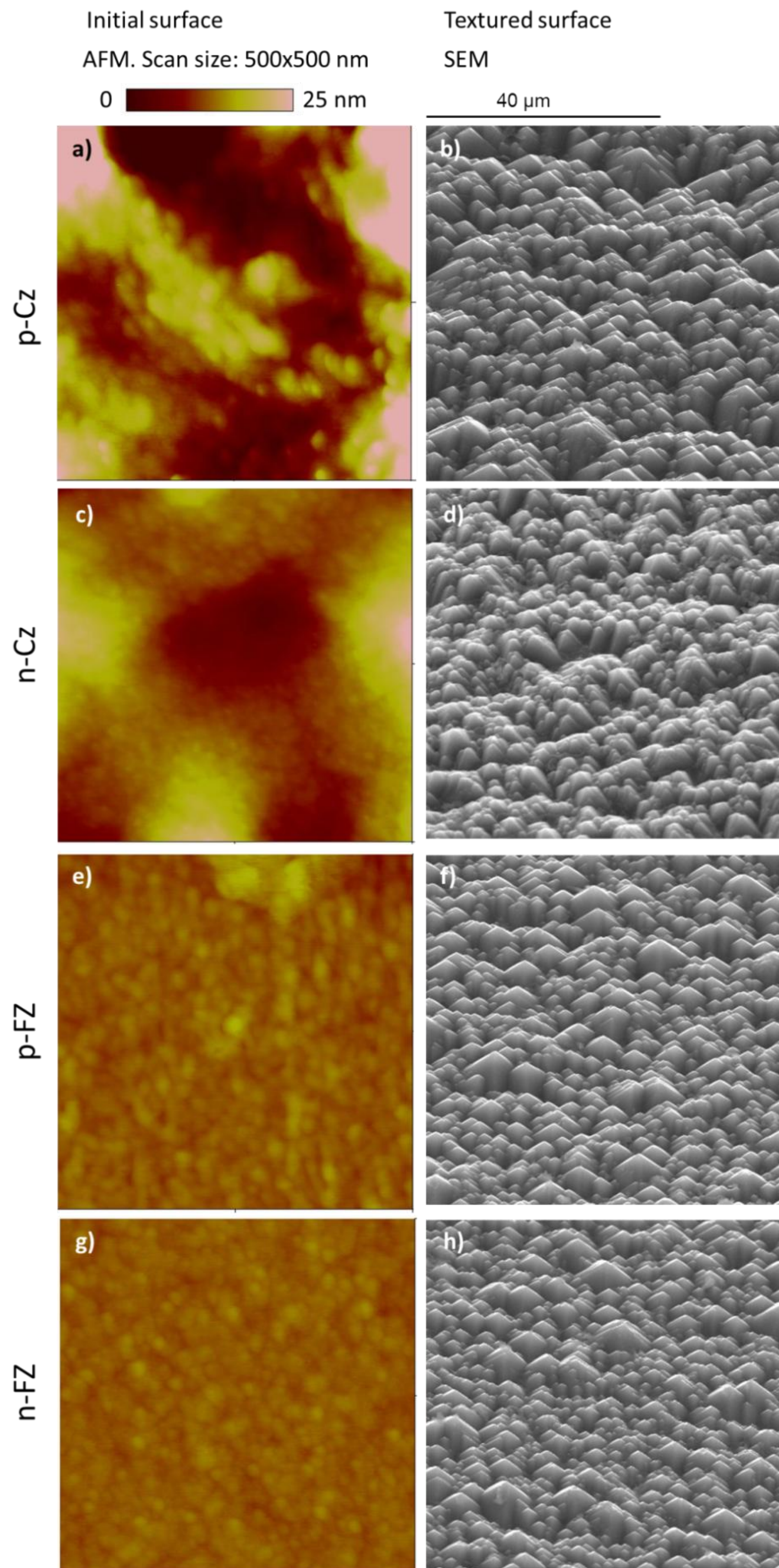

Figure 5.5. AFM images of the initial surface of different silicon samples (as cut Cz and shiny etched FZ) (left column) and SEM images (1500x) of surfaces after texturization with S1/0.2 solution during 30 minutes (right column).

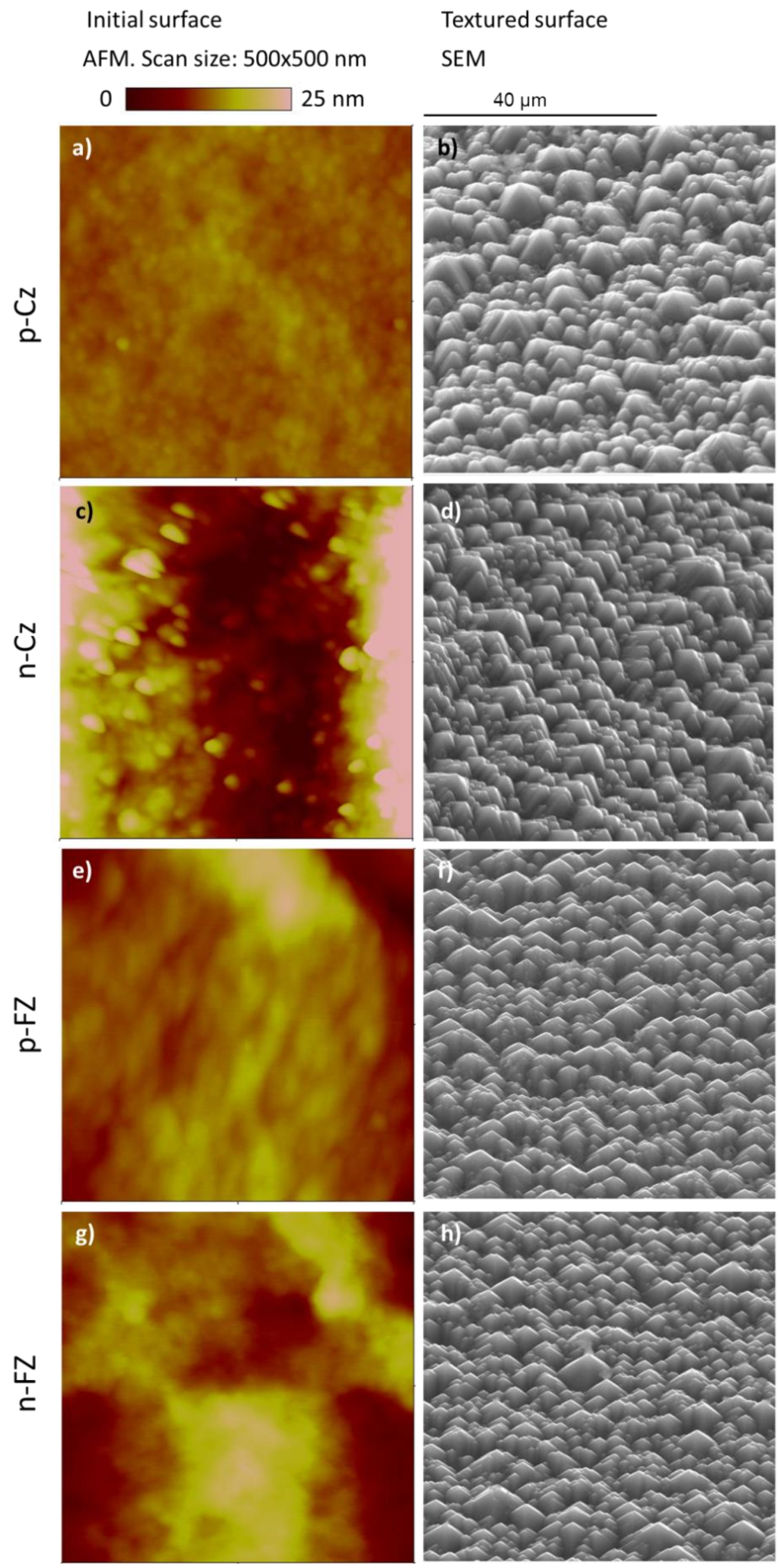

Figure 5.6. AFM images of the initial surface of different silicon samples (as cut Cz and shiny etched FZ) treated with a NaOH aqueous solution during 1.5 minutes (left column) and SEM images (1500x) of surfaces after texturization with S1/0.2 solution during 30 minutes (right column).

Table 5.3. Comparison of the etching rate and $SWR_{400\text{-}900}$ for different Si (100) wafers with and without NaOH pre-treatment, textured with the S1/0.2 solution during 30 min.

Wafer type	NaOH pre-treatment	Etching rate (µm/min/side)	% $SWR_{400\text{-}900}$
p-FZ shiny etched	No	0.26	12.1
p-FZ shiny etched	Yes	0.28	11.4
n-FZ shiny etched	No	0.27	11.8
n-FZ shiny etched	Yes	0.27	11.9
p-Cz as cut	No	0.32	11.7
p-Cz as cut	Yes	0.30	11.5
n-Cz as cut	No	0.23	13.0
n-Cz as cut	Yes	0.27	12.4

Except for the n-Cz, it can be concluded that the differences in the final morphology and *SWR* are negligible, taking into account that the different positions of the samples in the carrier inside of the 4 l vessel can lead to slight differences in the morphology due to local turbulences in the solution, etc. It should be mentioned that the NaOH treated p-Cz and p-FZ were positioned in the first and last position of the carrier (being the rest of the samples in the middle positions) and this could induce changes in the transport of chemicals from the solution to the surface. It can be concluded that a NaOH pre-treatment does not improve significantly surface morphology and reflectance, and that the initial surface roughness has no significant influence on the texturization with the new ultra-low concentration S1/0.2 solution.

A study of pre-cleaning treatments performed on different silicon materials prior their texturization with KOH/IPA [100], has shown no correlation between the texturing behaviour and the crystal growth method and conductivity type, concluding that the alkaline texturing behaviour and its result is not dependent on bulk material. However, the results show a dependence on the initial surface conditions. If we relate this study and its conclusion with the results exposed above, it could be inferred that after the long etching time (30 minutes) at the slow etching rate of the S1/0.2 solution there should not be essential differences in the textured surface, since once the first micrometres of the surface are etched the texturization should proceed through the silicon bulk in similar manner for the different silicon materials. Evidences for this assumption are given in chapter 6.

5.3 Temperature dependency and activation energy of the silicon texturization

The Arrhenius dependency of the silicon etching in alkaline solutions on the temperature is already well known [57]. The etching rate depending on the temperature takes the form:

$$r = r_0 exp[-(E_a/R_g T)] \tag{5.1}$$

where r is the etching rate, r_0 the pre-exponential factor, E_a the activation energy, R_g the gas constant and T the absolute temperature. From the slope of a linear fit of the logarithm of the etching rate versus the inverse of the temperature, the activation energy E_a can be determined.

The variation of the chemical concentration in the solution leads to different temperature dependent behaviour and activation energies. In some alkaline systems two regimes in the Arrhenius plot with two different activation energies of the process can be observed [24].

The temperature dependency of the etching rate of the S1/0.2 solution has been studied for the range between 50 ºC and 90 ºC. (100) p-type Cz as cut and FZ shiny etched samples have been textured during 15 minutes at different temperatures and their etching rates were determined gravimetrically. The Arrhenius plot of the etching rate dependence on temperature is shown in Figure 5.7.

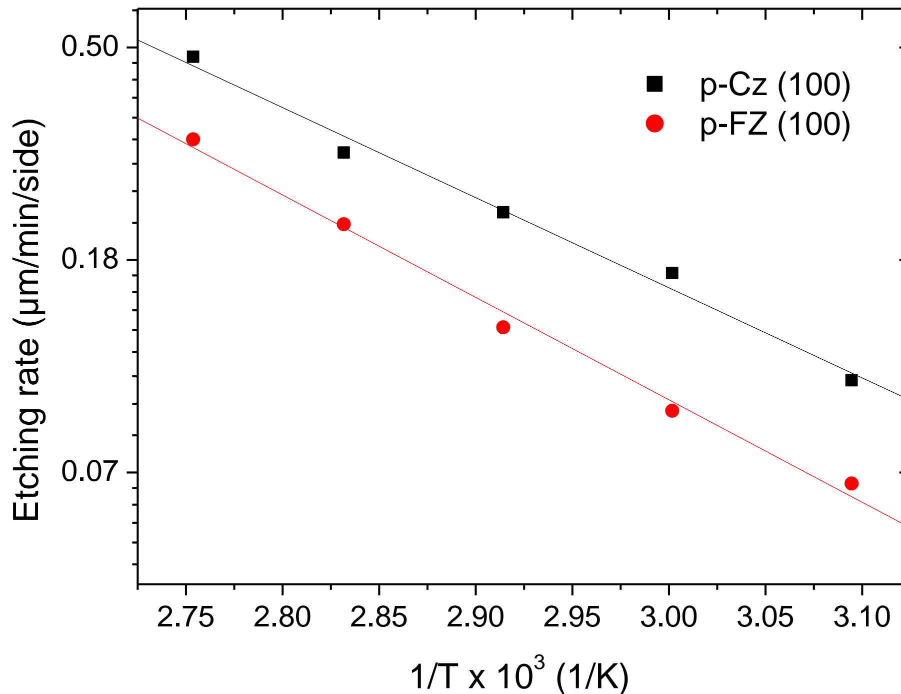

Figure 5.7. Arrhenius plot of the etching rate dependency on temperature of p-Cz and p-FZ (100) wafers.

The linear fit of the data shows that the temperature dependent behaviour of the etching rate follows the Arrhenius equation (the squared correlation coefficient is 0.988 for the Cz as cut material and 0.992 for the FZ shiny etched material). From this data, the activation energy of the texturization process in S1/0.2 solution is determined to be 0.36 eV for the (100) p-Cz as cut material, and 0.42 eV for the (100) p-FZ material. These values are in agreement with the values given in the literature for moderately-doped silicon etching in several alkaline solutions, which vary from 0.22 eV for 3.7 wt% NH_4OH solutions [101] to 0.62 eV for 20 wt% KOH solutions with added IPA, for example. An extended review of activation energies for silicon etching in different alkaline solutions can be found in [57]. The different activation energy for the as cut Cz and shiny etched FZ can be explained by their different initial surface. Even though it was shown in section 5.2 that the initial surface has no significant influence on the final morphology obtained, it can have an influence on the first stages of the etching process (see chapter 6.2).

5.4 Scale-up of the process

The experiments and results reported in the previous section have been carried out at laboratory scale. In order to make a first evaluation of the possible suitability of the process with the S1/0.2 solution to be applied in the industry, and the lifetime of the solution, a 12 l heated bath (semi-industrial scale, see description in section 4.1.1) has been filled with the low concentration S1/0.2 solution. It is possible to texture at least 46 wafers (100 cm^2 size) distributed in 8 charges (the number of etched wafers per charge varied depending on the charge). In this experiment p-Cz as cut wafers were used. The solution was cooled down to room temperature after every charge. For the texturization, the temperature of the bath was set-up to 90°C. The resulting values of $SWR_{400-1100}$ and etching rates can be seen in Table 5.4. The first batch of wafers was textured during 30 minutes, which was the optimum time found for the texturization with the S1/0.2 solution carried out with the laboratory scale set-up. As it can be observed in Table 5.4, the reflectance is higher than the one obtained with the 4 l set-up. Therefore the reaction time was decreased for the subsequent texturization batches. The value of the *SWR* is still not satisfactory, and the process for this higher volume should be optimized. However, the experiment resumed in Table 5.4 shows that it is possible to reuse the S1/0.2 solution after cooling it down to room temperature several times and that it is possible to texture at least 46 wafers with a volume of the solution of 12 l without large changes in the etching rate or the *SWR*.

Further experiments have been done to optimize the reflectance result of the textured wafers. For this purpose, the texturization with the S1/0.2 solution has been carried out in the semi-industrial scale set-up at different temperatures and times on p-Cz samples of 16 cm^2. The results are shown in Table 5.5.

Table 5.4. Global etching rates and $SWR_{400-1100}$ for different charges of Si (100) p-Cz wafers textured with the S1/0.2 solution in a 12 l bath at 90°C.

Batch No.	Quantity of wafers	Time (min.)	Etching rate (µm/min/side)	% $SWR_{400-1100}$
1	6	30	0.31	22.3
6	9	26	0.31	19.8
8	9	26	0.32	20.9

Table 5.5. Global etching rates and $SWR_{400-1100}$ of Si (100) p-Cz samples textured with the S1/0.2 solution in the semi-industrial scale set-up at different temperatures and times.

T (°C)	Time (min.)	Etching rate (µm/min/side)	% $SWR_{400-1100}$
70	25	0.20	14.7
75	25	0.23	13.4
80	20	0.25	13.1
80	25	0.24	11.7
85	20	0.32	11.7
85	25	0.30	11.9

The reflectance curves of the samples from Table 5.5 are shown in Figure 5.8.

The best reflectance results are for the process at 80 °C and 25 minutes, and for the process at 85 °C and 20 minutes, reaching $SWR_{400-1100}$ values under 12 %. It is worth mentioning that with the scale-up of the process the conditions of temperature and time are more advantageous (less time and lower temperature), reaching a similar result in reflectance compared to the laboratory-scale system. As seen in section 5.1, with the laboratory-scale set-up, a temperature of 90°C and a reaction time of 30 minutes were needed to obtain $SWR_{400-1100}$ under 12 %.

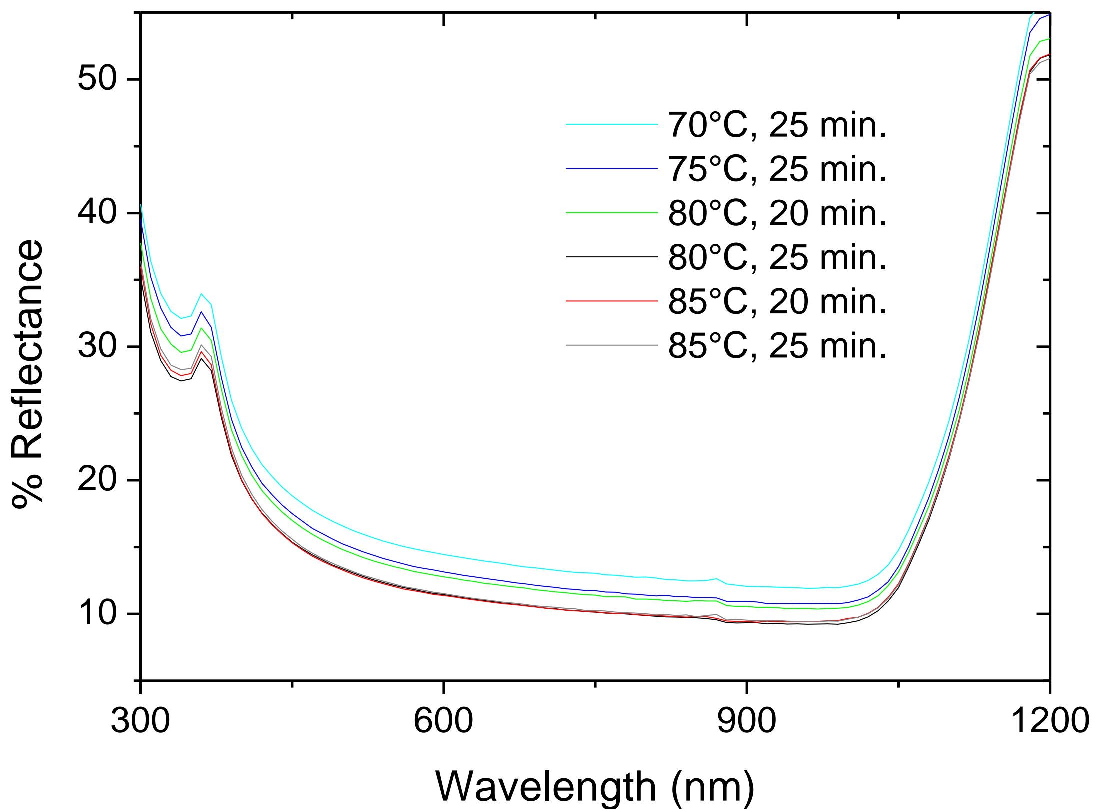

Figure 5.8. Reflectance spectra of Si (100) p-Cz samples textured at different temperatures and times textured with the S1/0.2 solution in the semi-industrial scale set-up.

5.5 Conclusions

A new ultra-low concentrated solution for texturization of monocrystalline (100) silicon for solar cell production has been proposed and studied. The novel ultra-low concentration solution consists of 1 wt% Na_2CO_3 / 0.2 wt% $NaHCO_3$ aqueous solution. The results of the experiments show that it is possible to use a 12 times more diluted solution compared to the minimum concentrations found in the bibliography, and 20 times more diluted compared to the optimum established previously by our group. The novel texturization process also improves the surface morphology and decreases the reflectance to values below 12 % $SWR_{400-1100}$. No additives as IPA are required for the texturization.

Some basic aspects of the texturization with the new ultra-low concentration solution have been studied. The ultra-low concentration solution is able to texture different silicon substrates (n- and p- type, FZ and Cz grown, shiny etched and as cut) achieving similar surfaces morphologies and reflectance values, except for the case of n-Cz as cut wafers, which show a higher reflectance. A NaOH pre-treatment has been introduced prior to the texturization to modify the surface, showing no influence of the initial surface on the texturization result with the ultra-low concentration solution except for

the n-Cz as cut silicon. For this material, the NaOH pre-treatment enhances the textured surface and slightly decrease the reflectance value. Also, the temperature dependent behaviour of the texturization process with the new ultra-low concentration solution has been studied, concluding that the system follows the Arrhenius law, and the activation energy of the process (0.36 eV for the (100) p-Cz Si and 0.42 eV for the (100) p-FZ Si) is in the same range of other alkaline solution systems for (100) silicon texturing encountered in the literature.

As a first estimation of the lifetime of the ultra-low concentrated solution, it has been observed that it can be cooled down to room temperature and be reused at least eight times, and at least 46 wafers can be textured with 12 l of solution. The parameters of the reaction for a semi-industrial scale process have been optimized. For $SWR_{400-1100}$ values under 12 %, 80 °C and 25 minutes, and 85 °C and 20 minutes were found to be the optimum process conditions. This ultra-low concentrated solution can be a promising candidate to be implemented in the photovoltaic industry due to its lower requirement of chemicals and lower temperature compared to the Na_2CO_3/$NaHCO_3$ texturization processes proposed in the existing literature [10, 61], leading to lower costs and optimum results.

6 Microscopic analysis of pyramid formation and its mechanism

The fact that the different texturization conditions lead to different pyramidal morphologies regarding to the pyramid shape, size and covering of the surface has been already demonstrated in chapter 5 and in the existing bibliography [10, 61, 102]. The evolution of the silicon surface morphology from the (100) surface towards the pyramidal topography is not completely understood up to now. There exist different models to explain how the formation of the pyramids is started and how the surface is shaped during the reaction time. This chapter tries to contribute to the clarifying of these aspects in the case of Na_2CO_3/$NaHCO_3$ texturization of silicon.

6.1 Literature survey on the mechanism of pyramidal formation by alkaline solutions

The chemical/electrochemical mechanism of silicon etching reactions by alkaline solutions is widely studied, as discussed in Section 3.4. The local different velocities of these etching reactions due to their selectivity depending in the crystal orientation lead to the formation of pyramids in (100) silicon. This is what here is referred as *formation mechanism of pyramids*. There are different theories which describe the nucleation and evolution of pyramidal texturing and the reason behind the final observed pyramidal profile, a topic very important for the micromachining industry, in which the suppression of the pyramid formation is normally desired. A review of the most relevant bibliography about this topic, related to different alkaline etching systems, is presented in this section. It should be noticed that in this section the concept of *roughness* refers also to the appearance of pyramids, as used in the cited bibliography.

In the existing literature about pyramid nucleation [102-112], the most coincident point is that there is a masking agent that locally prevents silicon from being etched, while not masked areas are etched until {111} planes are exposed. But also other possible reasons are given in the bibliography, as summarized below.

Palik et al. [103] proposed a pseudo masking model in which hydrogen bubbles and/or silicate etch products adsorbed on the surface act as a barrier to reactants attacking the silicon for the KOH etching system case. They disregarded native silicon oxide masking or defect nucleation as these barriers, and observed that stirring of the solution and increase of the temperature decrease the etching rate (which is associated with the presence of {111} planes [101]) and the roughness.

On the other hand, Schnakenberg et al. [97] observed higher formation of hillocks for pH values under 13 when no HF pre-treatment was done prior to the alkaline etching in

tetramethyl ammonium hydroxide (TMAH) and water. They also suggest that silicon etching products polymerize on the surface and this could have a masking effect. This is attributed to a poor transport of the etching product which is transported in a lower rate than its production rate. They conclude that the native oxide and the polymerized etching product should have similar masking effect.

The theory of pyramids being originated by bulk crystal defect nucleation is claimed by Bhatnagar et al. [104]. They argue as a reason for this that the pyramids appear aligned and that their density on the etched area depends on the previous thermal treatment, which affect the defect density. They state that also the masking of etching products plays a role together with the defect nucleation. Furthermore, they observed in ethylenediamine/pyrocatechol (EDP) etching experiments continuous appearance and disappearance of the pyramids caused by a layer by layer *peeling* due to etching at tip and edges of the pyramids. They exclude contamination from the solution as a nucleation agent.

Schröder et al. [105] supported the layer by layer peeling mechanism in KOH solutions and they observe some plateaus that they attribute to hydrogen bubbling.

A different approach is the one proposed by Tan et al. [106], who studied the KOH etching system and opted for a growth mechanism rather than for an etching mechanism, suggesting a re-deposition of the etched atoms. In their opinion, the pyramid formation by hydrogen bubbles or etch product polymerization masking is dismissed.

Elwenspoek [107] compared the dissolution of crystals to the kinetics of crystal growth. In this argumentation, in anisotropic etching systems (111) surfaces would be kinetically flat, having a higher step-free energy which would result in much slower etching rates compared to kinetically rough surfaces as (100) with lower step-free energy. However, in isotropic systems both surfaces (100) and (111) would be rough, and therefore etched in a highest similar rate. In atomically flat surfaces, steps, in which edge atoms have a smaller binding energy to the crystal, are not present. The etching rate is governed by the nucleation barrier, i.e. the creation of a cavity by the removal of an atom in a flat surface to propagate a step would costs certain energy. Elwenspoek also suggests that impurities can be adsorbed in steps, blocking their propagation and the etching at certain points of the surface. This last idea is in accordance with the experiments of Hein et al. [108], who observed a higher roughness when metallic impurities were added to the solution.

The addition of alcohols and other additives are related by some authors to pyramid nucleation and density. Vazsonyi et al. [102] attribute an enhanced nucleation and density of pyramids to additives which improve the wettability of the surface. On the other hand Rola et al. [109], in relation to their study of KOH/tertiary-butyl alcohol etching, propose that alcohol molecules adsorbed on silicon surface act as a micromask. If the case of Na_2CO_3/$NaHCO_3$ solutions, which does not contain any surface tension

modifier, is taken into account, it can be concluded that alcohol and additives are not the main pyramid initiators, even when they can play an important role.

Some authors have performed Monte Carlo simulations [110, 111] in order to model the anisotropic etching. Gosálvez et al. [111] base their simulation in an atomistic model. In their model, the probability of the removal of a Si atom of the crystal structure depends on the number of first and second neighbour Si atoms to it is bonded to, since a succession of thermally activated breakage of chemical backbonds of the structure is assumed. The energy of the bonds is weakened by hydroxide ions. Gosálvez and Nieminen [112] have also described the pyramidal formation and attributed it to impurity stabilization of surface atoms against removal of the etchant, according to the above mentioned theories. Their simulations are able to reproduce the nucleation and formation of the pyramidal hillocks. In this model the initial apex atom is stabilized by the attachment of two impurity atoms from the etching solution, causing the nucleation. Van Veenendaal et al. [110] modelled the pyramidal formation establishing a slower etching rate for atoms under a semipermeable mask. They suggest that not only the pyramid top, but the <110> ridges of the pyramid base are stabilized by silicate particles.

6.2 SEM analysis of pyramidal formation

The SEM analysis of silicon wafers submitted to different texturing times can give information at microscopic/mesoscopic scale about how pyramids are formed during the reaction time. For this purpose two different experiments have been carried out.

In the first experiment different samples cut from Cz and FZ wafers were textured at different reaction times corresponding to the early stages of the pyramid formation with the aim of observing the nucleation, density and size of the pyramids evolution.

In the second experiment a multiple-step texturization was carried out. Single FZ samples were textured, analysed and subsequently immersed again in the same texturing solution to continue the texturization process and analysed focusing in the same area to evaluate the formation mechanism of the pyramids, as the same concrete pyramids can be traced by this method.

6.2.1 SEM analysis on different wafers treated at different texturization times

In this experiment 16 cm^2 p-type Cz as cut and FZ shiny etched (100) Si samples were textured at different total texturization times. The wafers were dipped in 1 vol% HF and cleaned in deionised water prior to the texturization. The texturization solution used contained 1 wt% Na_2CO_3 and 0.2 wt% $NaHCO_3$. The samples were cleaned in deionised water and dried in nitrogen. Finally the sample surface was analysed by SEM.

Interestingly, despite of the results of chapter 5 showing no significant influence of the initial surface roughness of the wafers regarding to the final pyramidal morphology after several minutes of texturization, the analysis of the early stages of the etching process on the two different surfaces shows that in the first minutes the proceeding of the of reaction differs for the distinct surfaces, as seen in Figure 6.1 and Figure 6.2.

In the case of as cut Cz, which has an extremely rough and damaged surface due to the saw cutting of the wafers (Figure 6.1 a), a strong preferential etching is observed at certain defects or cavities present in the surface, and deep etched structures are formed (marker 1). After 3 minutes of reaction at 70 °C (Figure 6.1 c and d), nucleation of nanometric pyramids appears in some areas (marker 2), while other areas present flat surfaces. The pits and channels preferentially etched present anisotropic characteristics (marker 1). It seems to be that during the first stages of the surface texturization there exists certain isotropic component. The temperature of 70°C has been chosen in order to produce a lower etching rate and slower evolution of pyramid formation for enhanced observation.

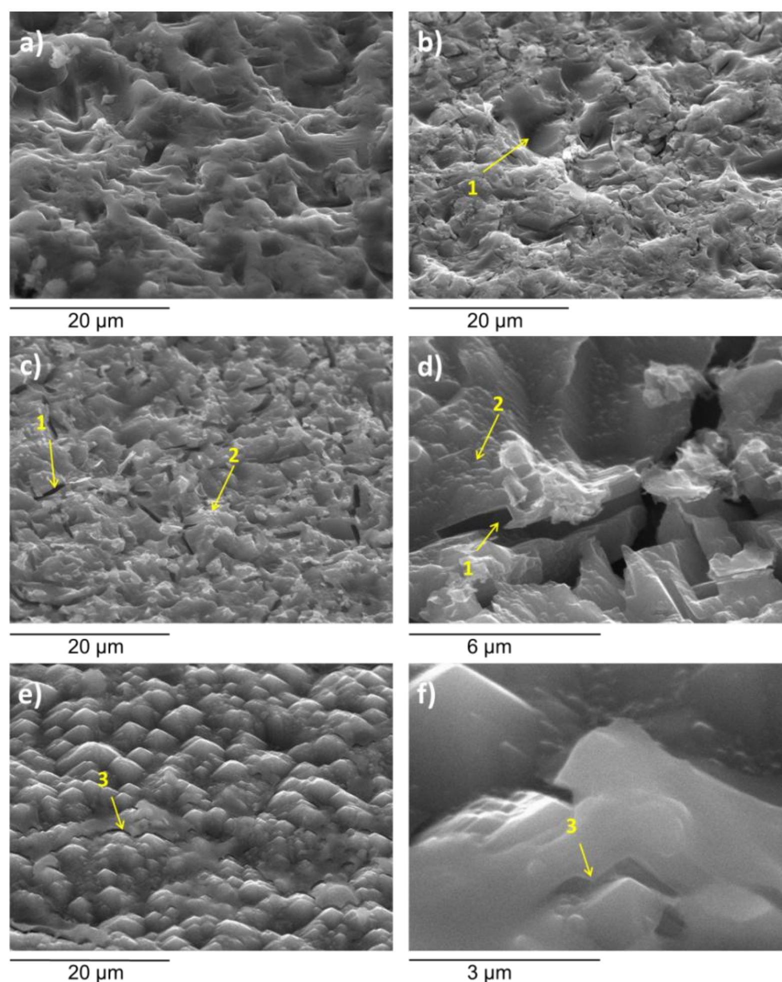

Figure 6.1. SEM images of Cz (100) as cut Si samples textured at 70 °C during: a) 0 min; b) 1 min; c) and d) 3 min; e) and f) 20 min.

At 70 °C and 20 minutes some smooth areas and deep grooves which underetch these areas with anisotropic shapes (Figure 6.1 e and f, marker 3) can be observed. It could be inferred from the images that these smoother layers could be detached by the underetching. But there is no concluding image for this, and it could also happen that the Si volume corresponding to these areas is dissolved.

The experiment on FZ Si has been carried out at 85 °C and etching times between 30 seconds and 5 minutes. The relatively flat initial surface of the shiny etched wafers allows easy observation of the pyramid nucleation at shorter reaction time. The deeply etched channels/pit micrometric structures which can be seen in the Cz as cut wafers are not observed.

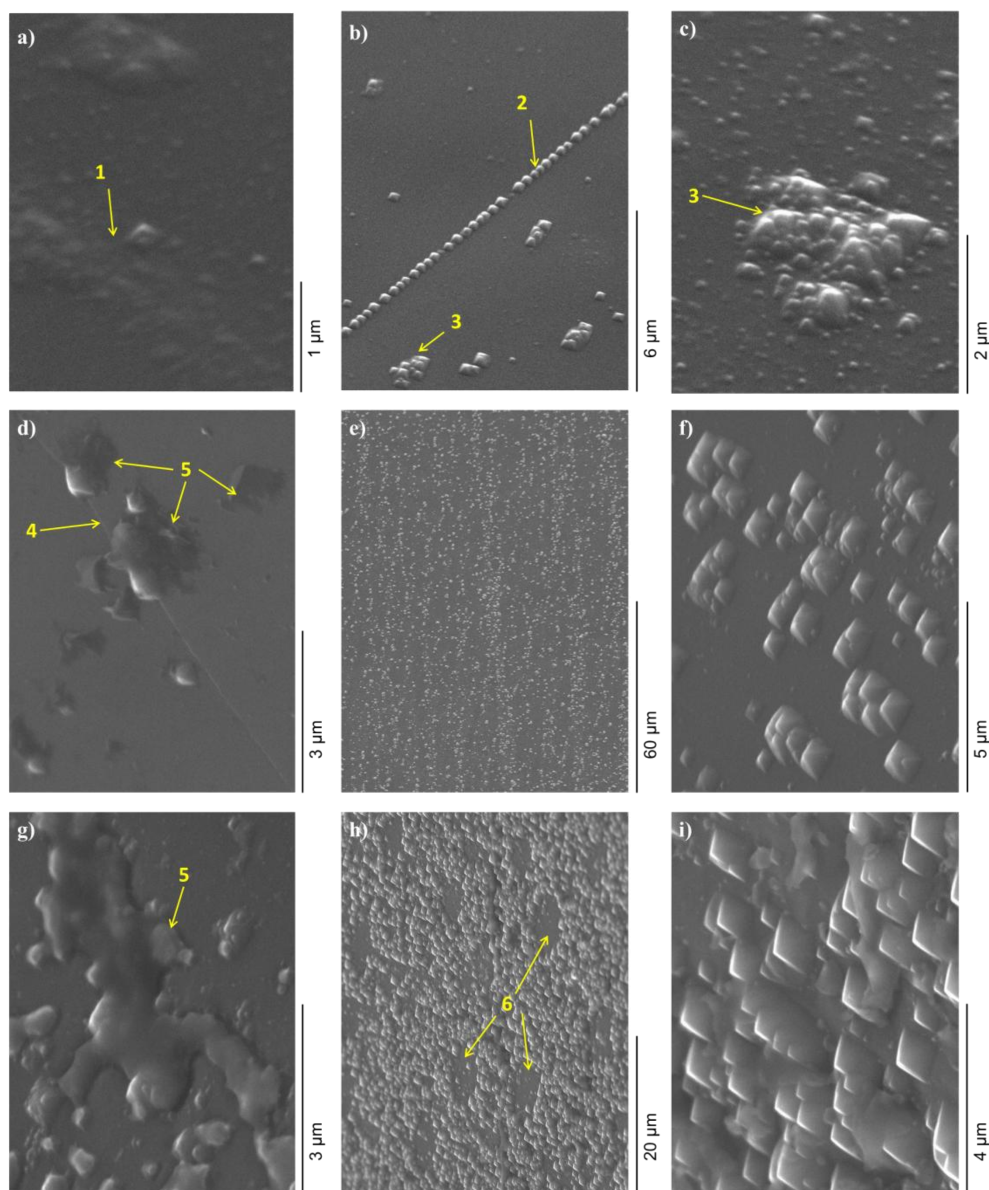

Figure 6.2. SEM images of FZ (100) shiny etched Si sample textured at 85 °C during: a) 30 s; b) and c) 1min; d) 2 min; e), f) and g) 3min; h) and i) 5min.

Figure 6.2 shows the resulting surface after the different reaction times. At 30 seconds of reaction time some *protopyramids* are already observed (marker 1). The hillocks are not well defined and have a size in the nanometer range. The resolution of the SEM device used is not sufficient enough to analyse this structure. Therefore this sample has been also analysed by AFM and the results will be shown in Section 6.3.

In Figure 6.2 b and c, the surface morphology after 1 minute is shown. Some pyramids of approximately 200 to 250 nm height have been formed. The height of the formed pyramids at this point is in coincidence with the calculated etching depth in the samples: 233 nm per side. This could suggest that the top of these first formed pyramids were initially near to the wafer surface, or in the first layers, while the rest of the sample is etched isotropically (if the theory of re-deposition or re-grown of the pyramids is dismissed). The formation of pyramids in a line which appears in Figure 6.2 b (marker 2) should be noticed. This perfect alignment of the pyramids can be due to a defect nucleation, in agreement with the work of Bhatnagar et al. [104]. In Figure 6.2 d a crystal defect (marker 4) and some pyramids nucleated along it can also be seen.

At 1 minute of texturization (Figure 6.2 b and c) it can also be observed that most of the larger and well defined pyramids are distributed in groups (marker 3), while the rest of the silicon surface is composed by smaller hillocks (at around 100 nm) starting to be formed. The size of the pyramids together with the well-defined shape suggests that they are either consecutively formed and re-dissolved or integrated in larger pyramids during the reaction time until forming the final pyramidal morphology.

Another interesting feature observed in Figure 6.2 h is the circular plains (marker 6) that appear smooth within pyramidally textured areas. The diameter of such structures is approximately 6 μm. This makes evident the possibility of micrometric hydrogen bubbles masking, according to Schröder et al. [105]. However the structures shown in Figure 6.2 h are not plateaus as in reference [105], but plains where the solution have acted in an isotropic manner. It could be proposed that the hydrogen bubbles first mask these areas, and once the bubbles are detached from the surface, the (100) surface is firstly etched isotropically, before the nucleation of pyramids occurs also in this area.

Figure 6.2 d and g show apparently amorphous structures (marker 5). It is not clear if these structures are deposits or not. An EDX (energy-dispersive X-ray spectroscopy) analysis of the sample textured for 3 minutes on the mentioned amorphous structures, on the flat etched area and in the pyramids gives the elemental composition spectra exposed in Figure 6.3. A qualitative evaluation of the spectra shows a dominant silicon content and higher content of oxygen in the amorphous structures than in the rest of the sample area. This could be attributed to the existence of silicon oxide or silicates at these points, which can be correlated to the proposed theory of masking by reaction products causing pyramid nucleation [103, 97].

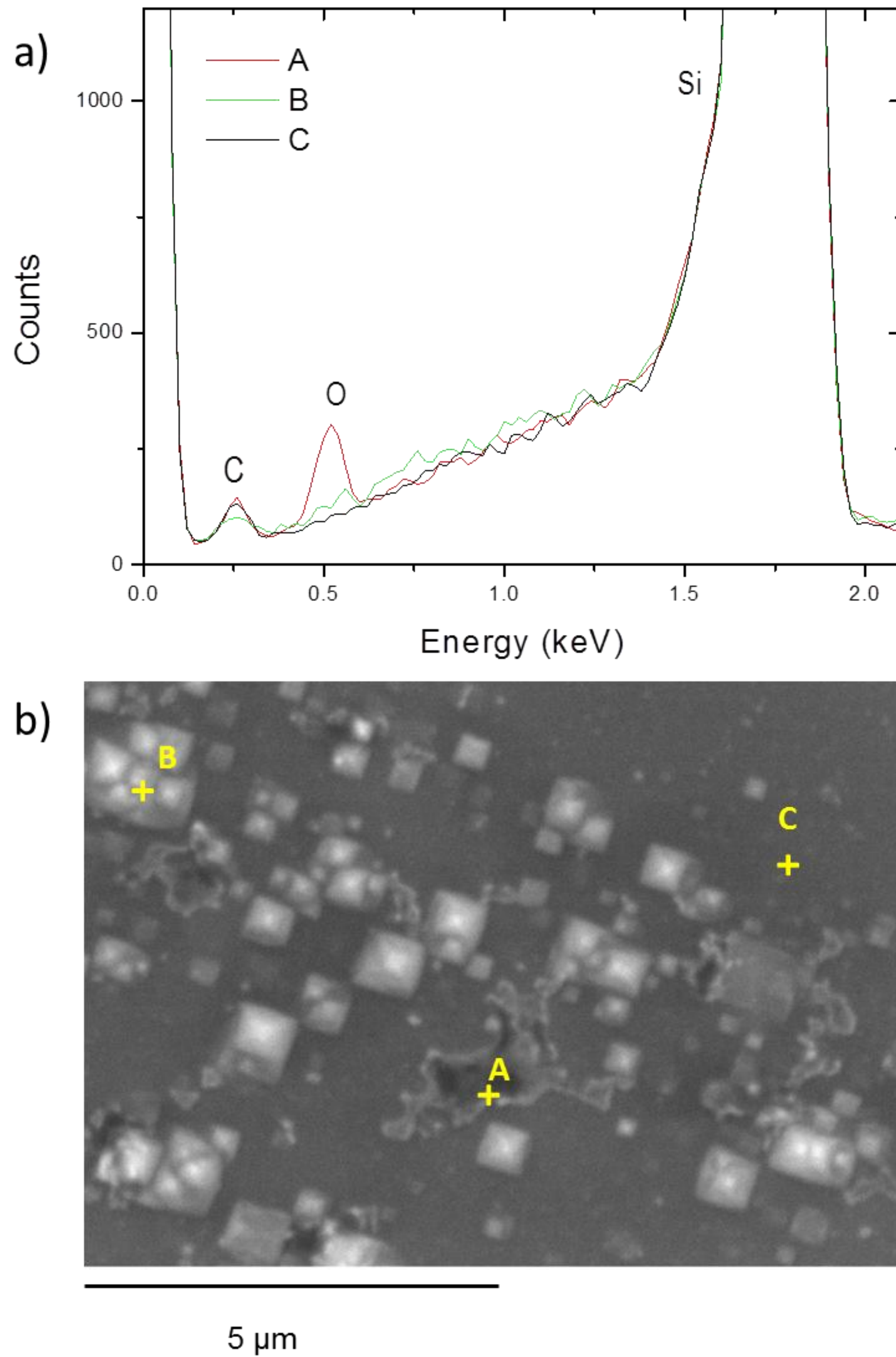

Figure 6.3. EDX spectra of a) 3 min textured sample and b) sample locations from where the EDX spectra were obtained.

The global etching rates measured for the different samples etched at different times are shown in Figure 6.4. Within the first seconds or minutes of reaction the etching rate increases, and then decreases again. For Cz as cut silicon this increase is higher than for FZ shiny etched silicon. For the 1 minute Cz textured sample the etching rate is more

than the double of the etching rate for the 20 minutes Cz textured sample. This high initial etching rate can be correlated with the strong preferential etching observed in the SEM images of Figure 6.1 for short reaction times.

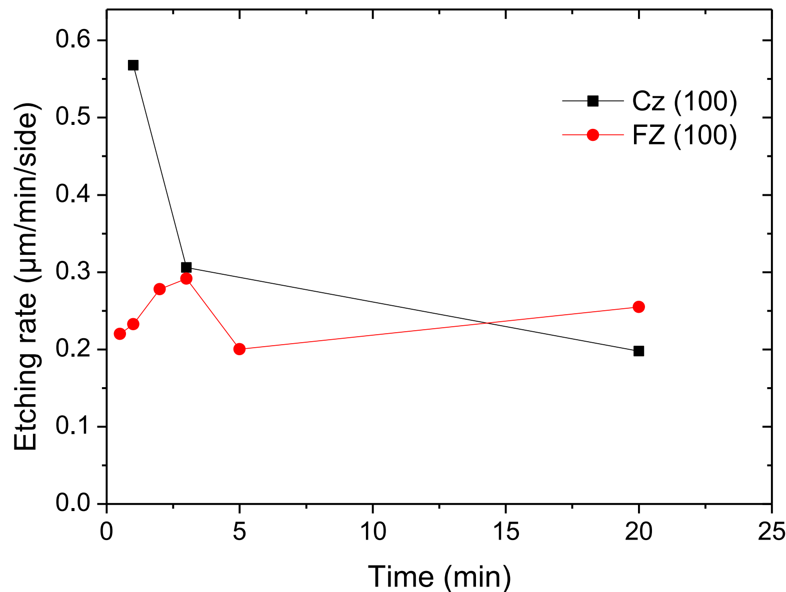

Figure 6.4. Global etching rate of the Cz and FZ (100) samples textured at 70 and 85°C respectively at different total times.

6.2.2 SEM analysis on multiple-step textured sample

In order to trace the formation of the pyramidal structures, 1x1 cm^2 p-type FZ shiny etched Si samples (100) oriented were submitted to texturization in 1 wt% Na_2CO_3 and 0.2 wt% $NaHCO_3$ solution at 85 °C. After a certain time of texturing the reaction was stopped and the samples washed in deionised water and dried in nitrogen prior to SEM analysis. After SEM analysis the samples were cleaned in deionised water and etched again in the same texturing solution, washed, dried and analysed by SEM. Due to the fact that some previous marks were done in the samples, SEM images could be obtained in the same areas of the samples to follow the evolution of individual microstructures. Subsequent steps of the texturing-analysis sequence were carried out.

The electron scanning produces a charge effect on the wafer surface which affects the texturing process as it can be observed in Figure 6.5 (marker 1). Therefore, the acceleration of the electron beam of the SEM device was decreased from 20 to 10 kV to partly avoid this effect. In particular, the small areas scanned at higher resolution suffer this effect. The frontiers limiting the previously area scanned at higher resolution can be clearly seen after texturing (marker 2). The aspect of the scanned surface change abruptly, the pyramids disappear resulting in squared pits. However at 10 kV the effect can also be observed at a lower degree in some scanned areas (see Figure 6.6, marker 6). An electron beam damage of the surface affecting the subsequent etching was also

observed by Nijdam [113] in a similar multiple-step etching experiment of silicon in KOH, who attributes the phenomenon to a deposition of products or residual gases present in the vacuum rather than to a charge effect on the surface.

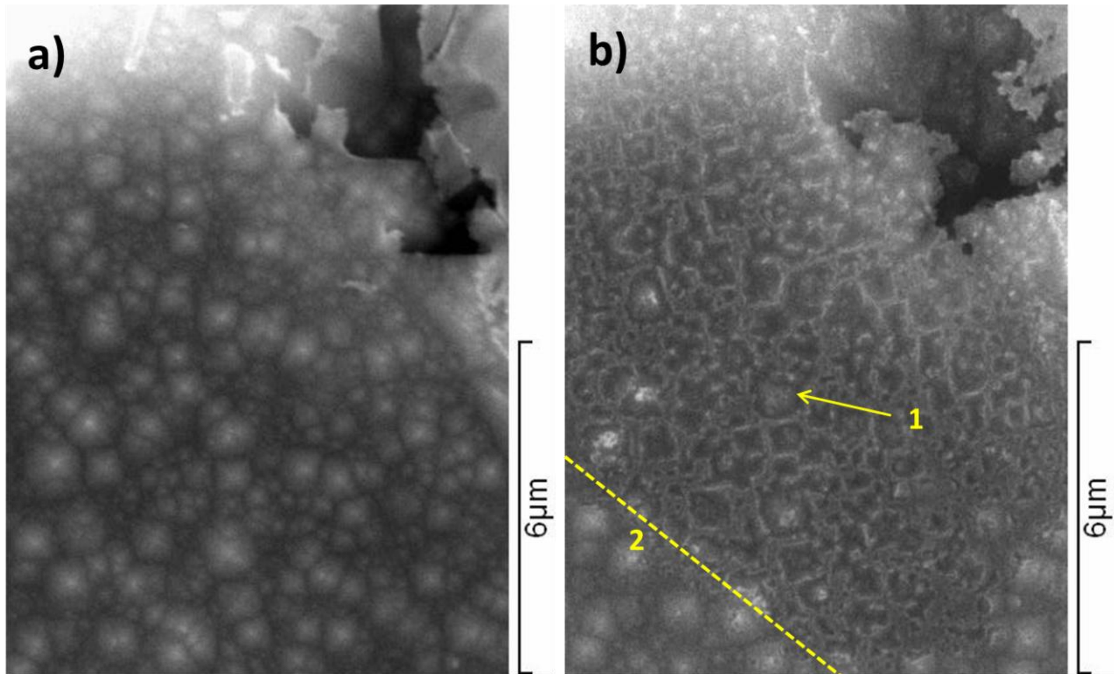

Figure 6.5. SEM images of the same area of a sample textured before (left) and after (right) electron scanning at 20 kV.

The multiple-step texturization of the samples presents the problem that the reaction is not continuously carried out, but stopped and re-started after the SEM measurement. Despite of the electron beam effect on the surface, the high proportion of exposed (111) surface, already present at the re-starting point of the reaction, decreases the etching rate, acting as a passivating surface regarding to the reaction velocity. On the other hand, this procedure has the advantage of allowing localizing exact areas on the sample to trace their evolution. Nevertheless, the experiment can be considered as an adequate approximation for describing the pyramid formation-disappearance mechanism.

In Figure 6.6 and Figure 6.7 the evolution of the pyramids formation on two different areas of the same sample is shown. The reaction times were set to values that allow enough nucleation and density of pyramids for the first SEM measurement and enough reaction time due to the slower activation for the multiple-step texturing. Therefore, the samples are analysed after 12 and 26 minutes of reaction. Some pyramids can be still identified after the second texturing step (marked in yellow and labelled with numbers in the images for their identification). Superposing the images, the numbered pyramids coincide in position in the scanned area.

It can be observed that while some pyramids have grown in size (Figure 6.6, markers 1, 2; Figure 6.7, markers 1, 2, 4, 5), at the expense of adjacent pyramids, others have been decreased (Figure 6.6, markers 3, 5). It can also be observed the splitting of one pyramid apex in two or more peaks (Figure 6.7, marker 3). On the other hand, some pyramids have completely disappeared and new small pyramids appear at their place (Figure 6.6, marker 4), in agreement with the peeling mechanism proposed in the bibliography [104].

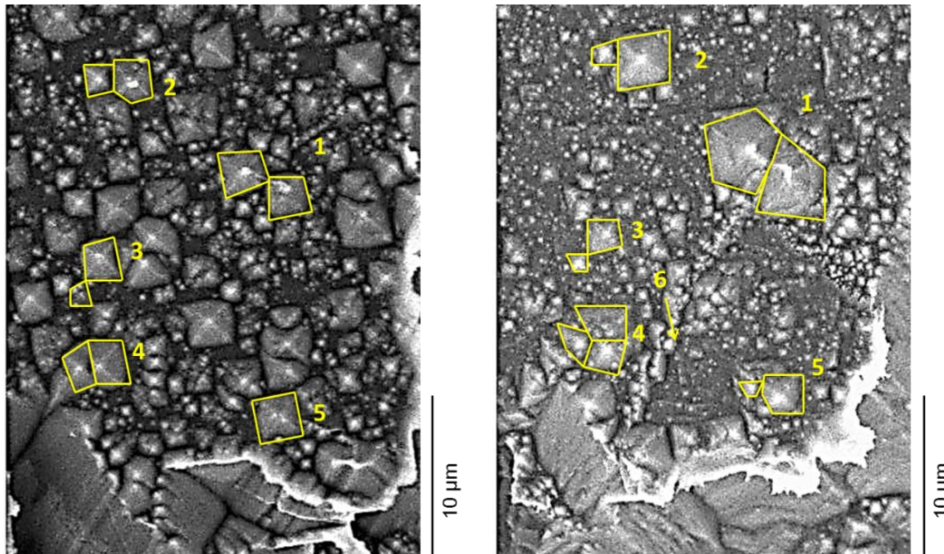

Figure 6.6. SEM images of the evolution of pyramid texturization obtained in the same area of a FZ (100) sample (area A) at cumulative texturization times of 12 min (left) and 26 min (right).[8]

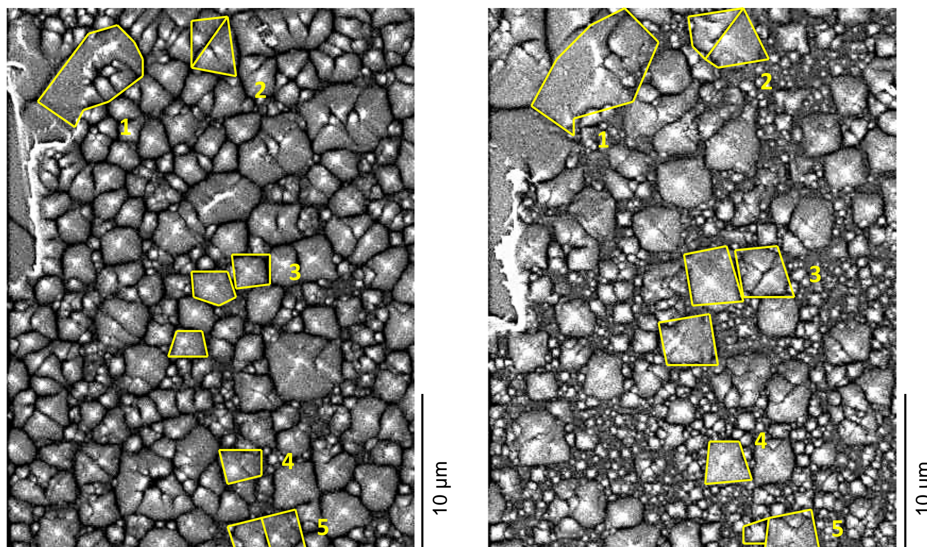

Figure 6.7. SEM images of the evolution of pyramid texturization obtained in the same area of a FZ (100) sample (area B) at cumulative texturization times of 12 min (left) and 26 min (right).[8]

[8] SEM images obtained at 10 kV of electron beam acceleration voltage.

From these results, it can be concluded that the stabilization of some pyramids to continue their growing coexists with the disappearance of pyramids by a layer by layer etching. Also a mixture of layer by layer etching and stabilization of new peaks formed from this etching could be suggested from the splitting of larger pyramids observed in the images.

6.3 AFM analysis of pyramidal formation

The aim of the AFM analysis is to trace the appearance of the anisotropic structures in their very initial stages, when their size is still in the nanometric range, as this cannot be observed by SEM, which has lower resolution.

The experiment for the AFM analysis has been divided in two parts. In the first part a set of different samples etched independently at different total reaction times are analysed.

In the second part a sample has been textured, analysed and re-textured for short reaction times in order to observe the roughness evolution of the sample.

6.3.1 AFM analysis on different wafers treated at different texturization times

The 16 cm^2 FZ shiny etched (100) Si samples analysed in this section has been submitted to a HF dip prior to the texturization process. They have been textured at 85 ºC in a 1 wt% Na_2CO_3 and 0.2 wt% $NaHCO_3$ solution during different total reaction times. The samples were afterwards rinsed in deionised water and dried in nitrogen.

Figure 6.8 shows scanned areas from approximately 1 µm x 1 µm and 2 µm x 2 µm of the textured samples. The *protopyramids* observed by SEM on the samples textured for 30 seconds are revealed by AFM to be hillocks with not totally defined pyramidal shape (Figure 6.8 a and b). The density of nucleation sites, which is already high at 30 seconds in a nanometric scale increases until the first minute of reaction. In Figure 6.8 d well defined pyramids can be observed, showing the anisotropic nature of the texturization from the very initial stages of the process. A pyramid with a base side of approximately 700 nm has been formed after 3 min of reaction, as shown in Figure 6.8 e. It should be noticed that the structure appears as a pyramid with stepped facets, suggesting that an original hillock has been peeled off revealing a smaller sharped pyramid. This conclusion agrees the above mentioned theories of layer by layer etching [105] and preferential removal of step atoms [107]. Square based pits are observed in Figure 6.8 f. A pyramid is observed inside of one of the etch pits. This can be explained as an effect of locally faster etching at pyramid ridges, together with a layer by layer etching from the top of the pyramid, and point to the importance of <110> ridge stabilization proposed by Van Veenendaal et al. [110]. Many of the features which can be observed at several minutes of reaction time, as splitting of a pyramid peak in two or more peaks, appearance of adjacent pyramids etc., and its coexistence (see Figure 6.6 y Figure 6.7),

are also observed in Figure 6.8 for short reaction times textured samples with nanometric pyramids. This suggest that pyramid formation is an equilibrium of appearance and etching of nanometric pyramids from the beginning of the process, resulting after several minutes of texturization time in bigger pyramid stabilization.

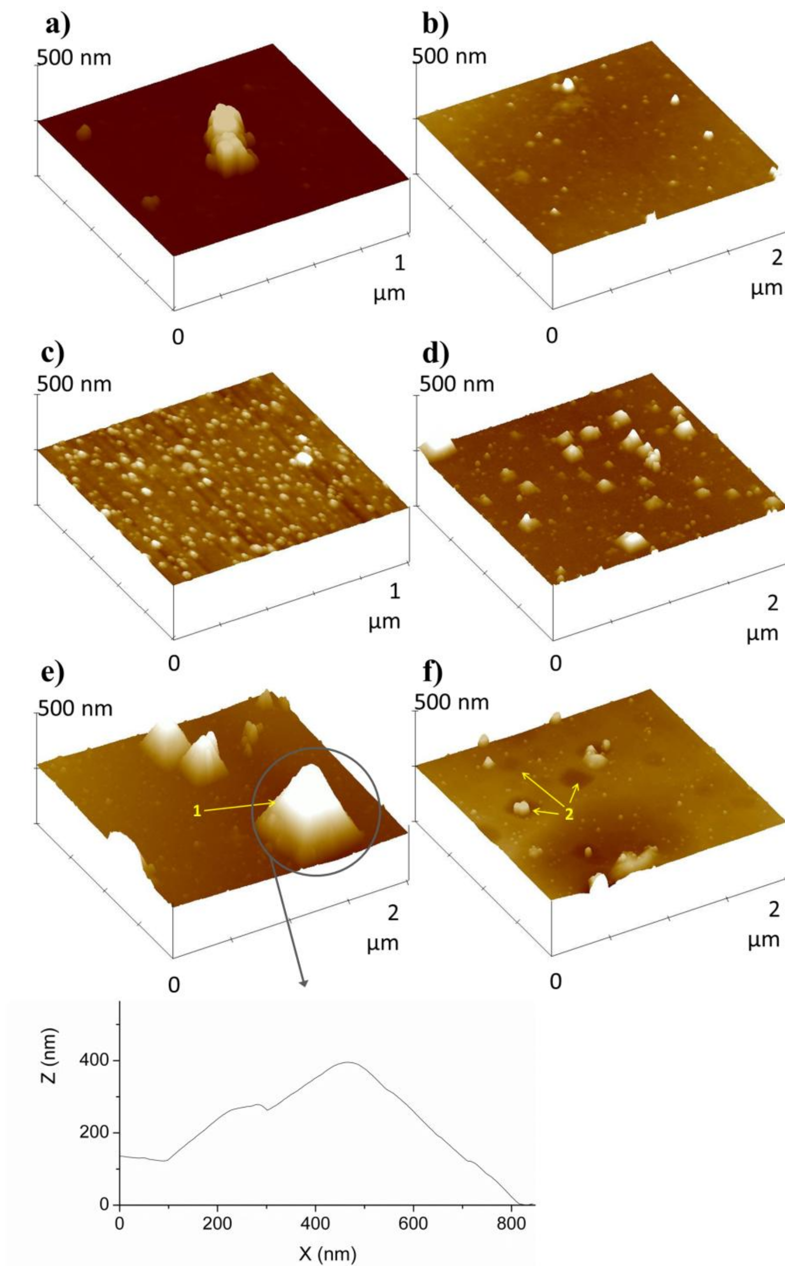

Figure 6.8. AFM 3D images of FZ (100) shiny etched Si samples textured at 85 °C during: a) and b), 30 s; c) 1min; d) 1.5 min; e) 3 min; f), 5 min.

6.3.2 AFM analysis on multiple-step textured wafer

For this experiment a 1 x 1 cm^2 sample was cut and mounted on a metal disc before being textured in order to trace the roughness evolution of the same sample after several

texturing steps. Some marks were done on the sample with the aim of scanning approximately the same area in each AFM measurement. However, contrarily to case of the SEM analysis, by the AFM technique concrete features could not be found and traced, but the measurements are done in the same area of about 80 μm x 80 μm after subsequent etching steps. It should be noticed that HF dip previously to the AFM imaging in order to eliminate the native oxide layer could not be carried out as the sample was mounted in a metal disc. The texturing steps were realized at 85°C in the same 1 wt% Na_2CO_3 and 0.2 wt% $NaHCO_3$ solution.

Figure 6.9 shows the roughness evolution of the sample through the AFM images. The initial non-textured sample, corresponding to a FZ shiny etched wafer with native oxide, shows a relatively high roughness (see Table 6.1).

Table 6.1. Root mean square (RMS) roughness calculated on 1 x 1 μm scanned area [9] of the re-textured sample after the different cumulative reaction times.

Texturing cumulative time	0 s	30 s	1 min	2 min	7 min
RMS roughness	11.82	5.69	5.83	6.85	8.19

However, the roughness is decreased after the first 30 seconds of reaction, and then is again increased during the reaction time.

The images of the 1μm x 1μm images suggest that the native oxide is etched during the first seconds of the reaction, smoothing the sample. After this, some grains more or less homogeneously distributed in size appear. The grains grow with reaction time and crowd together. In the case of the re-texturing experiments, the reaction presents lower velocity, as mentioned before, and the aspect of the surface does not show significant changes during the reaction time. Attending to the 25 μm x 25 μm images, some depressions present in the surface are accentuated with the reaction time, as shown by the higher contrast of the images for higher reaction time. The small pyramids observed in the 1 minute and 2 minutes 25 μm x 25 μm images turn into pits. The slow change in the aspect of the multiple-step textured surface in this case points out that the observed evolution cannot be taken as representative of the $Na_2CO_3/NaHCO_3$ evolution at the process conditions established in Chapter 5. However, the smoothness of the initially oxidized surface and the gathering of the structures in larger grains with the reaction time are worth to be noticed.

[9] Calculated with the software WSXM [85].

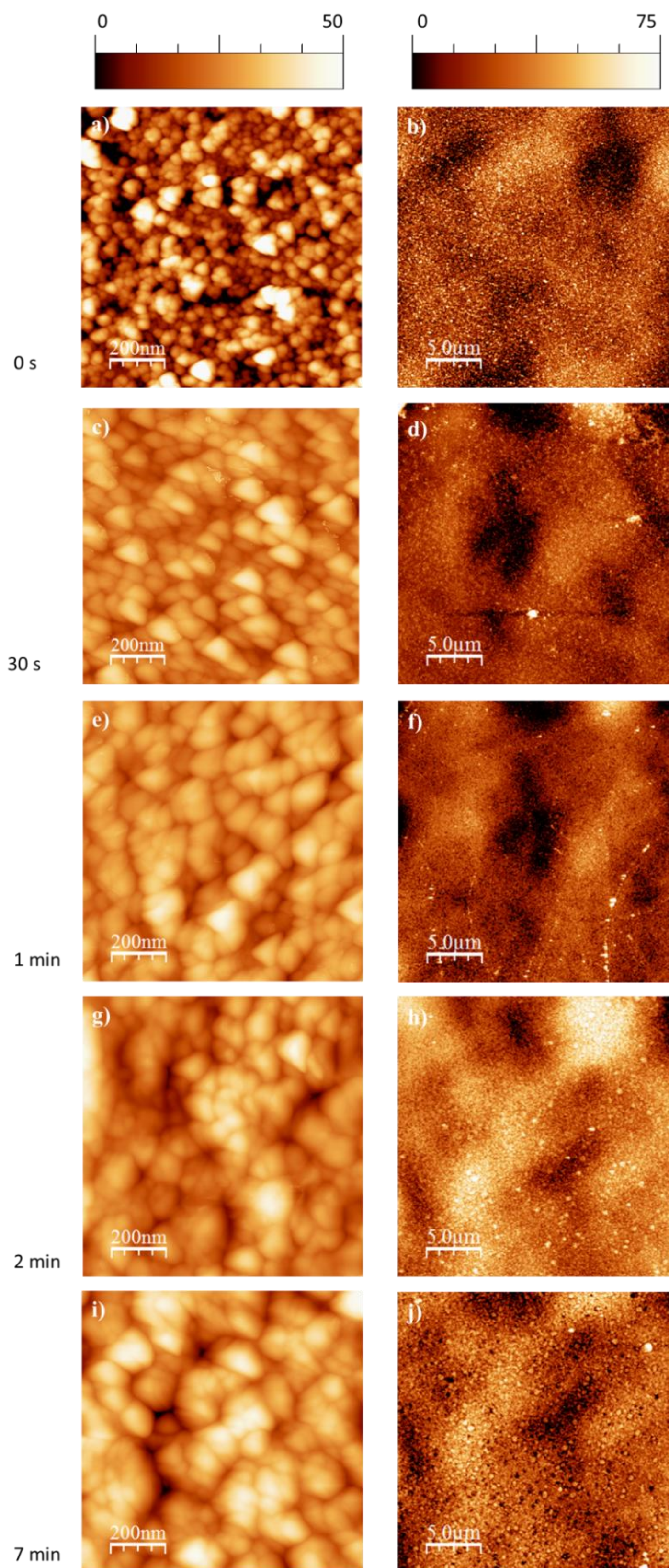

Figure 6.9. AFM 2D images of the same sample textured at cumulative times of: a), b) 0 s; c), d) 30 s; e), f) 1 min; g), h) 2 min; i), j) 7 min. The left column of images corresponds to scanned areas of 1µm x 1µm and the right column to scanned areas of 25µm x 25µm.

6.4 Conclusions

In this chapter the evolution of pyramid formation on (100) Si with the $Na_2CO_3/NaHCO_3$ solution has been experimentally studied by means of SEM and AFM.

At short reaction times, the texturization proceeds in different manners for the highly rough and defected as cut Cz Si and the shiny etched FZ Si. However, as shown in chapter 5, after several minutes of reaction, the surface does not show significant differences. The process shows an isotropic component during the first seconds/minutes of reaction (depending on the material), and during this period the native oxide layer and/or defected surface is removed. From the first stages of the process, well defined pyramids with size in the nanometric range have been observed.

About the origin of pyramid nucleation, the experiments done in this thesis give evidences, according to different hypothesis exposed in the bibliography, for defect nucleation [104], hydrogen bubbles influence [105], and reaction product masking [103, 97], showing that the initiation of pyramid formation can be originated by a mixture of different factors.

The formation evolution of individual structures could be traced by re-texturing of the same sample and SEM analysis, showing the coexistence during all the reaction time of pyramid formation and disappearance by layer by layer etching, and integration of pyramids during this process to form larger structures with reaction time.

7 $Na_2CO_3/NaHCO_3$ textured solar cells. Influence of the textured surface on solar cell parameters

In this chapter, different aspects of the $Na_2CO_3/NaHCO_3$ textured surface in relation to the solar cell processing and solar cell parameters have been analysed. Firstly, different surface morphologies produced by $Na_2CO_3/NaHCO_3$ texturization have been passivated and its influence on the surface recombination evaluated. Secondly, the influence of the $Na_2CO_3/NaHCO_3$ textured surface on crucial solar cell processing steps as the formation of the emitter and deposition of thin films is studied. Finally, phosphorous diffused screen printed industrial-like solar cells textured with the new ultra-low concentration $Na_2CO_3/NaHCO_3$ solution proposed in this thesis are presented and analysed.

7.1 Influence of $Na_2CO_3/NaHCO_3$ texturization on surface recombination

The texturization of silicon induces surface nanoroughness, as seen previously in chapter 5. This leads to an increase of the surface defect density, which increases surface recombination [66]. The morphology of two different textured surfaces and its influence on the passivation effect of an amorphous silicon passivation layer are analysed. n-type FZ substrates have been used and passivated by amorphous hydrogenated silicon. The texturization processes on n-FZ substrates are also of interest for heterojunction solar cells with amorphous silicon emitters.

As substrate material, 4 inch n-type FZ wafers with 1 Ω·cm resistivity were used. Subsequently, they were textured with two different processes (A and B) based on high concentration $Na_2CO_3/NaHCO_3$ solutions in order to obtain different structures. Non-textured wafers were taken as reference (labelled as R). Then the textured wafer were cleaned by means of the RCA process and, after being immersed in 1 vol% HF, they were both side passivated with a 20 nm a-Si:H layer following the procedure described in section 4.1.2. After the passivation, the minority carrier lifetime maps of the samples were determined by micro-wave photoconductance decay (μW-PCD). QSSPC measurements were also performed in the transient mode in order to evaluate the light injection dependence of the minority carrier lifetime of the samples.

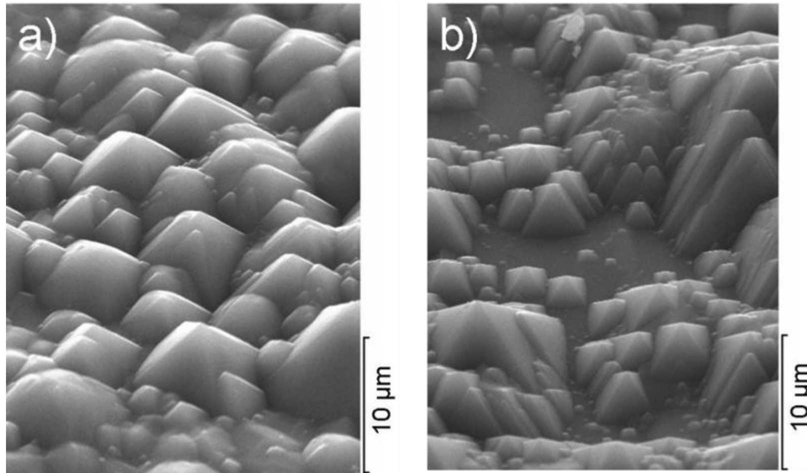

Figure 7.1. SEM images of the surface morphology of: a) texturization A; b) texturization B.

Figure 7.1 shows the surface morphology resulting from the two texturization processes A and B. Process A presents a homogeneous texturing with pyramids of 5 µm height while in process B the structures are irregularly distributed in size and non-textured areas appear in the sample. The height of the pyramids produced by process B is in the range of 2 to 15 µm.

Figure 7.2 shows the AFM images of the reference and textured samples after RCA cleaning and HF dip. It is worth mentioning that the images corresponding to the textured samples are obtained on the walls of the pyramids, offering a more accurate result than the usual approximations of reproducing the roughness of the pyramid walls by texturing (111) silicon samples. The nanoroughness of the textured samples is much higher than the nanoroughness of the reference. It is observed that texturization A shows a higher nanoroughness with higher and more sharpened nanostructures than texturization B.

The transient photoconductance analysis of the passivated samples reveals minority carrier lifetimes (at an injection level of $5 \cdot 10^{15}$ cm^{-3}) of 1371 µs for the reference sample, and of 94 and 173 µs for the samples A and B respectively. The surface injection level dependent recombination velocity of the samples calculated from the effective minority carrier lifetimes measured by QSSPC is shown in Figure 7.3. A significant increase of the surface recombination is observed for the textured samples compared to the reference sample.

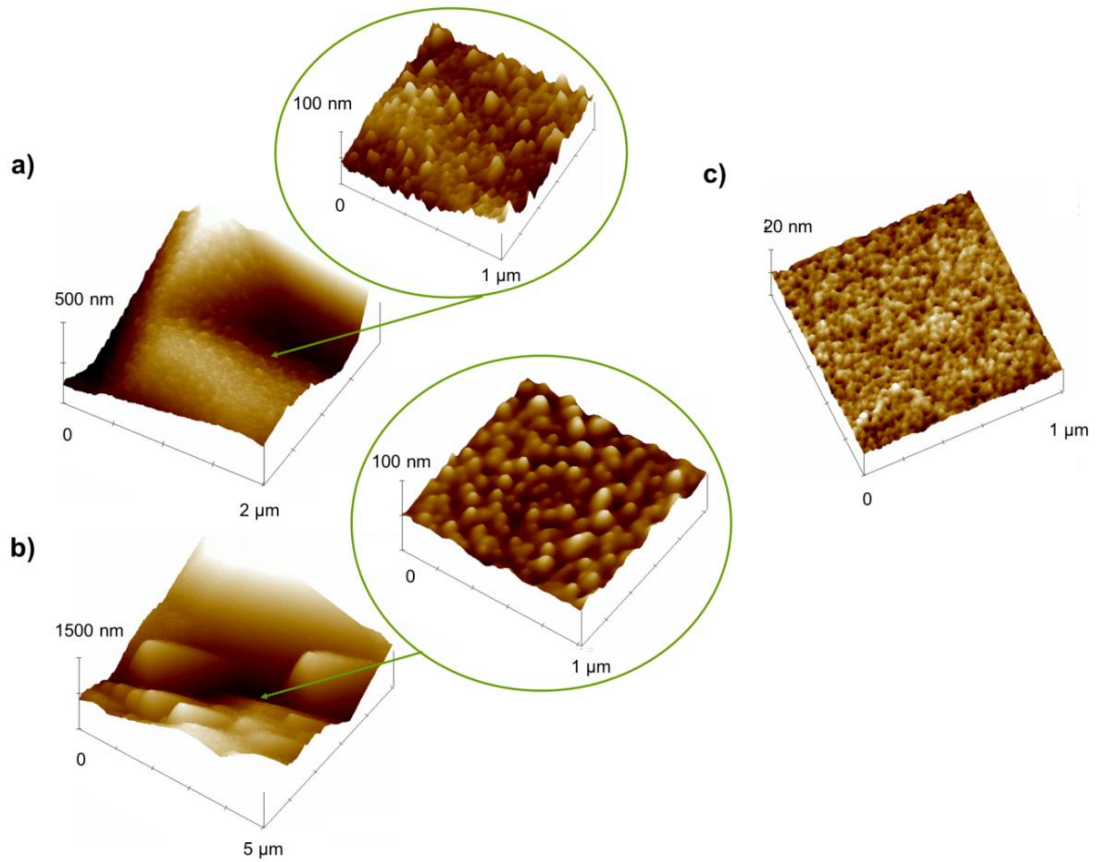

Figure 7.2. AFM images of the pyramidal textured surface: a) process A; b) process B and c) reference flat sample.

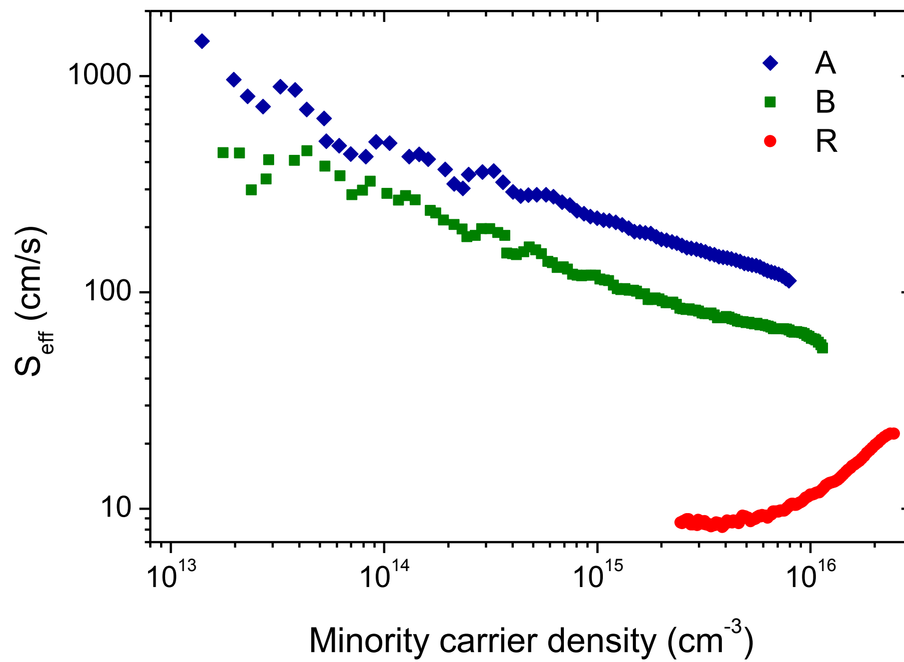

Figure 7.3. Effective surface recombination velocity of the passivated and the reference samples.

The pyramidal morphology decreases the passivating effect of a-Si because of the defects introduced by the texturization in the c-Si/a-Si interface [66]. Samples A and B present rough facets as shown in the AFM images. This nanoroughness increases the surface defect density [66], leading to higher surface recombination and therefore to lower minority carrier lifetime. The sample A shows a higher nanoroughness and therefore a higher surface recombination velocity compared to the sample B.

Furthermore, the sample B presents non-textured areas as observed in the SEM image, which could also contribute to its lower surface recombination compared to the sample A. These flatter surfaces would result in higher lifetimes. The decrease of the surface recombination with the increase of minority carrier density (Figure 7.3) is significantly pronounced for processes A and B. This effect could suggest a high quantity of defects on the surface of these samples. Defects on the surface and metallic impurities create energy levels within the bandgap, enhancing the recombination. Following the Shockley-Read-Hall model, at low injection level a decrease of surface recombination velocity with the increase of excess carrier density is expected [14]. This pronounced dependency of the effective minority carrier lifetime with the injection level suggests a higher defect density [114].

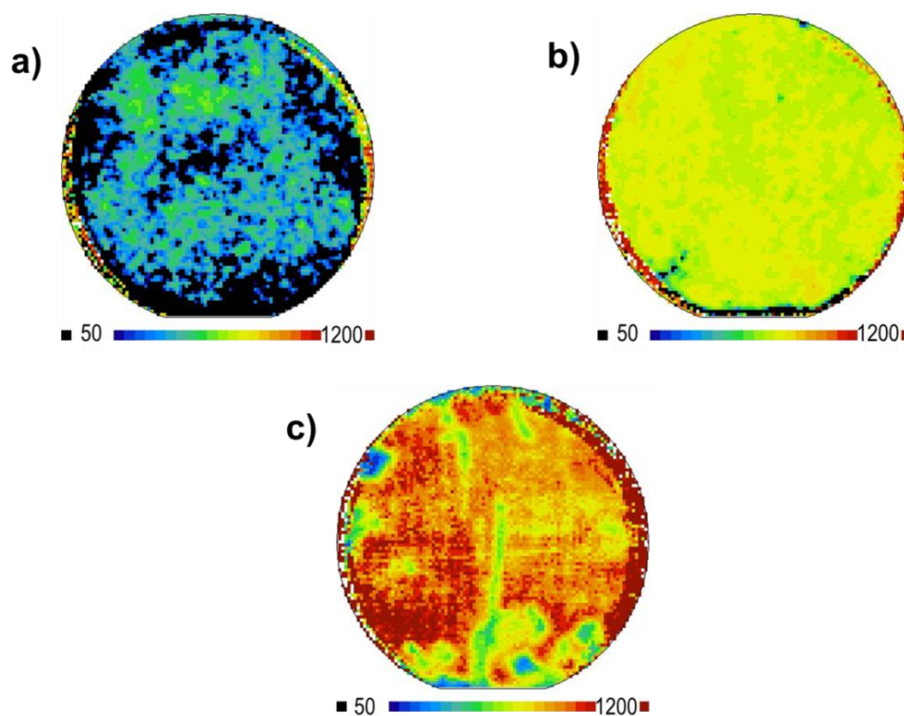

Figure 7.4. Minority carrier lifetime µW-PCD[10] topograms of the samples: a) process A; b) process B; c) reference flat sample. The scale is logarithmic.

[10] Measurement conditions: 1 mm resolution, intensity of $1.5 \cdot 10^{12}$ photons per laser pulse, 500 mSun bias light and 20 mV sensitivity.

Figure 7.4 shows the μW-PCD maps of the passivated samples. An inhomogeneous distribution of the lifetime over the surface of the textured wafers is observed. This is attributed to inhomogeneous morphologies, the higher lifetime areas correspond to less textured areas. The inhomogeneities on the lifetimes of the reference sample are attributed to surface contamination or defects introduced by the sample handling.

7.2 Deposition of layers and emitter formation on textured surfaces. Influence of $Na_2CO_3/NaHCO_3$ textured surfaces on solar cell processing

As described in chapter 4.1.2, in the solar cell production process there are different steps in which a layer is deposited on the silicon surface. The morphology of the silicon surface can affect the deposition of these layers, their thickness, conformality and coverage of the surface. The thickness of deposited layers varies for textured samples compared to flat samples for the same deposition conditions and time [115]. The influence of the pyramidally textured surface on the deposition time of an antireflection coating is an example. Given a deposition time for the PECVD of SiN_x, the resulting thickness is less for a textured surface than for a relatively flat saw damage etched surface, due to the higher surface area of the textured silicon. This affects the wavelength at which the minimum reflectance is observed (see Equation 4.3), and therefore the optical properties of the cells, and the deposition time for the optimum thickness of the ARC for textured cells should be adjusted. The same occurs for ITO (indium tin oxide) sputtered antireflection/conductive layers, for example.

The quality of the deposition on textured surfaces is also an important issue in the case of emitter [116, 117] and passivating layers [66, 118], since parameters of the solar cells as the minority carrier lifetime and the final voltage can be affected due to inhomogeneities in the layer continuity and thickness.

The interface between the silicon surface and the deposited layers as SiN_x and a-Si:H, and the diffused emitter have been analysed by FE-SEM (field emission scanning electron microscopy, see chapter 4.2.1), in order to observe the conformality and coverage of the surface of the layers, and the homogeneity of the layer thickness deposited over the pyramids. For this purpose, silicon samples with the mentioned layers, previously submitted to a saw damage etching or to the ultra-low concentration $Na_2CO_3/NaHCO_3$ texturization, have been cut and their cross section has been analysed. The results are shown in this section.

7.2.1 Emitter formation

For textured solar cells a lower V_{OC} is expected due to their higher surface area (see Equation 3.5). However, given certain conditions of temperature and time for the phosphorous diffusion, the different thickness and the different dopant concentration of

the emitter of textured solar cells would also have an influence on the V_{OC}. Thus, the emitter formation on textured cells should be optimized.

In order to study the variation of the emitter formation on textured solar cells compared to saw damage etched cells a batch of wafers has been saw damage etched or textured with the ultra-low concentration $Na_2CO_3/NaHCO_3$ solution prior to a chemical cleaning and phosphorous diffusion. Three different diffusions have been carried out at the same temperature T but with different diffusion times $t_1 < t_2 < t_3$, and the textured and saw damage etched wafers have been diffused simultaneously. Directly after the PSG removal, the sheet resistance of the emitter has been measured by the four point probe technique. Details about the phosphorous diffusion, chemical cleaning and PSG removal can be obtained in section 4.1.2. The sheet resistance has been measured directly after PSG removal.

Afterwards, the samples have been cut for FE-SEM observation. With FE-SEM and by means of SE (secondary electron) dopant contrast image, it is possible to distinguish electrically active dopant species in semiconductors [119, 120]. The n-doped areas appear darker than the p-dopes areas [121]. The fundamentals and mechanism of this effect are described and discussed in the literature [119, 121].

The resulting dopant contrast images of the emitter of the saw damage etched and textured samples at different diffusion times are shown in Figure 7.5. The emitter formed on the textured surface is in average remarkably thinner than in the saw damage etched surface (see also Table 7.1). The emitter formed on the pyramids appears deeper on the top of the pyramids and shallower on the valleys, having an intermediate thickness on the facets. This is in agreement with other authors who have also observed this effect [117, 122]. As expected, the emitter thickness increases with diffusion time. However, the difference between emitter thicknesses of saw damage and textured surface is decreased with increasing diffusion time. Thus, the ratio of the emitter thickness on saw damage etched surface to the thickness on textured surface is 2.2 for t_1, 1.9 for t_2, and 1.0 for t_3.

With the longest diffusion time t_3, two effects are observed: the thickness of the layer is more homogeneous over the pyramid profile, being the thickness on the top, the valleys and the facets more similar than for the shorter diffusion times t_1 and t_2; and the thickness of the emitter of the textured surface is nearly the same than the thickness of the emitter of the saw damage etched surface.

The difference between the measured sheet resistances (Table 7.1) of saw damage etched and textured wafers also decreases with the increasing diffusion time, being the average value of sheet resistance lower for the textured surface. As well, for the diffusion time t_3, the average value of sheet resistance is similar for both saw damage etched and textured surface.

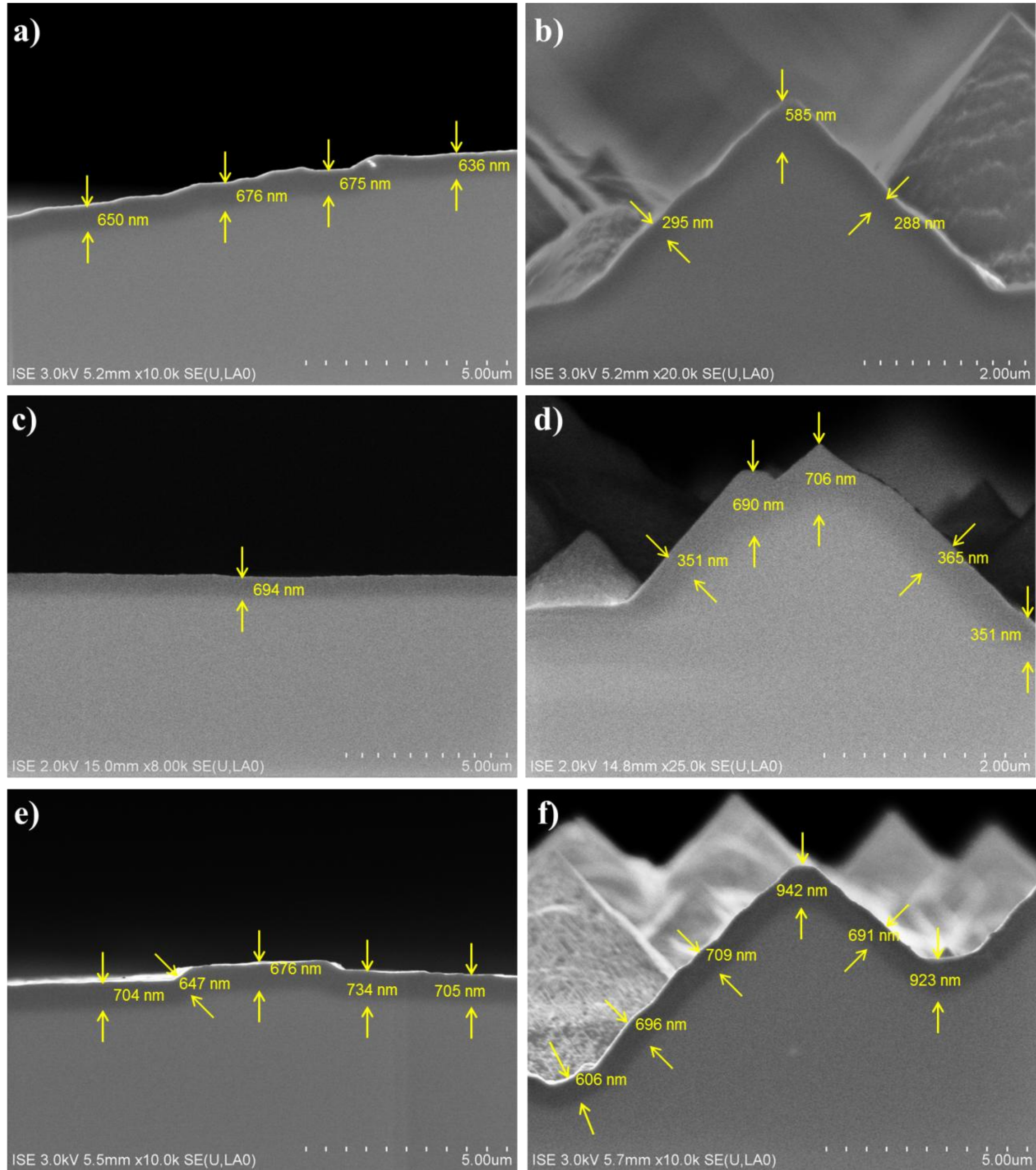

Figure 7.5. FE-SEM doping contrast images of the cross-section of silicon wafers submitted to saw damage etching or ultra-low concentration Na_2CO_3/$NaHCO_3$ texturization and to phosphorous diffusion at different times $t_1 < t_2 < t_3$: a) saw damage etched, t_1; b) textured, t_1; c) saw damage etched, t_2; d) textured, t_2; e) saw damage etched, t_3; f) textured, t_3.

A decrease of the real open circuit voltage on the textured samples compared to saw damage etched samples is expected due to the higher recombination of textured samples caused by (i) a larger surface area, (ii) possible different response to passivation of {111} facets compared to {100} planes, and (iii) stress induced effects on passivation layers at the top and valleys of the pyramids [118]. An additional decrease caused by the inhomogenous and shallower emitter should be considered. Taking into account the

emitter thickness and sheet resistance measured on the samples, the open circuit voltage has been calculated for a flat surface with the program PC1D [30] and it is shown in Table 7.1. It should be noticed that the calculation does not take into account the texturization and its associated influence on surface recombination and current increase, showing only the influence of emitter thickness and sheet resistance resulting on textured surface on the open circuit voltage. Due to the effect of a shallower emitter the open circuit voltage is decreased on the textured samples. However, for the longer diffusion time t_3 the expected voltage on an equivalent flat surface is the same for the emitter formed on the textured sample compared to the saw damage etched sample.

Table 7.1.Emitter characteristics and calculated open circuit voltage on equivalent flat surface (a flat surface with the same surface area) for the different diffusion times on saw damage etched and textured samples.

Diffusion time	**Average sheet resistance (ohm/sq)**		**Approximated emitter thickness (nm)**		**Expected V_{OC} on equivalent flat surface (mV)**[**]	
	Saw damage etched	Textured	Saw damage etched	Textured[*]	Saw damage etched	Textured
t_1	58.2	55.3	659	295	0.688	0.670
t_2	51.9	50.7	694	351	0.685	0.670
t_3	45.7	45.5	705	699	0.680	0.680

[*]Measured on the (111) facets. [**]Calculated with PC1D[11] [30] for the case of a flat surface with emitter characteristics as produced on the saw damage etched and textured wafers which are shown in the table.

From the results presented above it can be concluded that the differences on the emitter characteristics on textured samples compared to flat samples, and differences on emitter thickness on the top of the pyramid compared to the valleys can be attenuated by applying longer diffusion times at a given temperature. However, the doping profile should be investigated in to order to study the emitter formation on the pyramids in more detail. To obtain the appropriate emitter characteristics the temperature and time of the diffusion should be optimized [68]. For textured cells the temperature and diffusion time should be optimized compared to flat cells, being possible to achieve similar emitter characteristics.

[11] Parameters used: Thickness: 200 µm. p-type background doping: 10^{16} cm^{-3}. Front diffusion: sheet resistance and junction depth from the table. Files have been obtained from the program for wavelength dependent absorption coefficient, refractive index and light excitation. The rest of the parameters have been kept as default. Note that the effect of the textured surface has not been introduced; therefore effects as surface recombination due to the textured surface are disregarded.

7.2.2 SiN_x deposition

As mentioned before, the deposition of passivating and antireflection layers is crucial in solar cell production. The most used antireflection/passivating coating in screen printed diffused crystalline solar cells is SiN_x, which acts both as antireflection and passivating layer.

For the observation of the SiN_x layer deposited on textured samples, two FZ silicon wafer textured with 1 wt% Na_2CO_3 / 0.2 wt% $NaHCO_3$ solution and 20 wt% Na_2CO_3 / 4 wt% $NaHCO_3$ solution, respectively were submitted to a wet chemical cleaning and to the deposition of SiN_x by means of PECVD. Afterwards, the samples were submitted to a thermal treatment corresponding to the *firing* process in order to submit the SiN_x layer to the same conditions than in the final solar cell. The results of the cross section FE-SEM images of the samples showing the layer and its interface over the pyramids are shown in Figure 7.6.

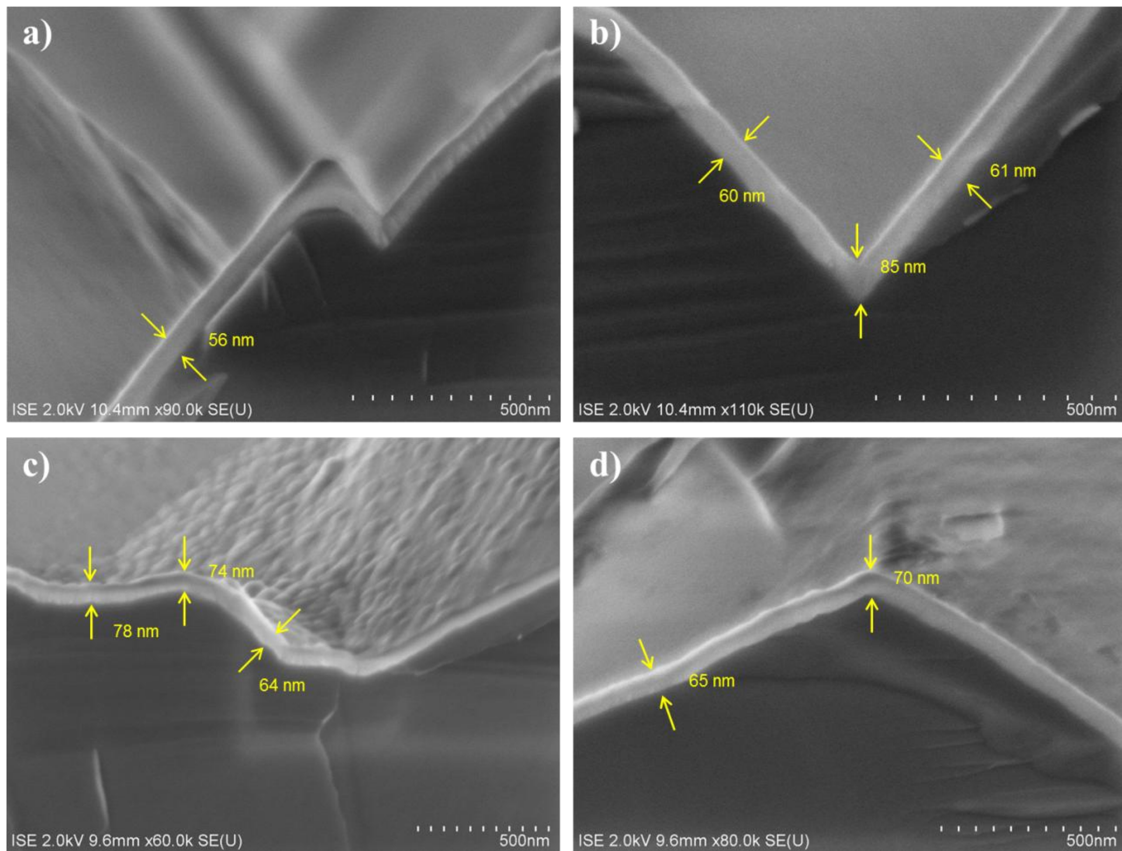

Figure 7.6. FE-SEM cross section images of textured samples with PECVD deposited layer of SiN_x: a) and b) samples textured with 1 wt% Na_2CO_3 / 0.2 wt% $NaHCO_3$ solution; c) and d) samples textured with 20 wt% Na_2CO_3 / 4 wt% $NaHCO_3$ solution.

The deposited SiN_x layer follows the pyramidal profile, showing a good conformality and coverage of the surface in the samples textured with both, the ultra-low

concentration and the high concentration Na_2CO_3/$NaHCO_3$ solutions, as seen in the FE-SEM images. The layer thickness is quite homogeneous over the pyramidal profile, with maximum variations of layer thickness on the facets approximately 15 nm, having a slightly higher layer thickness on the pyramid valleys (Figure 7.6 b).

A high surface nanoroughness is observed on the walls of the pyramids formed with the 20 wt% Na_2CO_3 / 4 wt% $NaHCO_3$ solution and coated with the SiN_x layer (Figure 7.6 c), while this is not observed on the samples textured with the 1 wt% Na_2CO_3 / 0.2 wt% $NaHCO_3$ solution. This confirms the AFM results presented in chapter 5.1 (Figure 5.4), and shows the conformality of the SiN_x deposition.

7.2.3 a-Si:H deposition

a-Si:H/c-Si heterojunction solar cells have attracted in the last years the attention of researchers and industry [123]. The high passivation effect of a-Si:H comparing to other layers [124] and the possibility of reaching high voltages in the a-Si:H/c-Si junction [125] are responsible of this fact, as well as the lower process temperature comparing to conventional diffused solar cell processes.

An intrinsic a-Si:H layer has been deposited by means of PECVD on FZ wafers textured with 1 wt% Na_2CO_3 / 0.2 wt% $NaHCO_3$ solution and 20 wt% Na_2CO_3 / 4 wt% $NaHCO_3$ solution after being cleaned by the RCA process [67]. The details of the deposition process are described elsewhere [76].

Figure 7.7 shows the FE-SEM images of the cross-section of the samples textured with the 1 wt% Na_2CO_3 / 0.2 wt% $NaHCO_3$ solution (Figure 7.7 a and b) and the samples textured with the 20 wt% Na_2CO_3 / 4 wt% $NaHCO_3$ solution (Figure 7.7 c and d) coated with a PECVD intrinsic a-Si:H layer. In the samples textured with the new ultra-low concentration solution a good coverage and conformality of the layer can be observed. The approximately 14 nm thick layer appears less clear at the valleys than at the top of the pyramid, suggesting that valleys can be critical areas regarding to deposition of a-Si thin layers. Python et al. [126] studied the PECVD deposition of thin microcrystalline silicon films on V-shaped surfaces, and observed a lack of electron signal on cross-sectional silicon samples on the valleys of these structures. They relate the lower SEM signal to less dense material areas and suggest as a cause a shadowing effect due to the morphology which affects the growth of the layer, together with a low ad-atom diffusion. This leads to the formation of microcracks in the case of microcrystalline Si layer deposited on V-shaped morphologies [126]. In the amorphous silicon deposited layers shown here this is not observed, however it should be taken into account that the resolution of the micrographs is not high enough for such observation.

The a-Si:H layer could not be clearly detected on the sample textured with high concentration Na_2CO_3/$NaHCO_3$ solution. Again, a high nanoroughness can be observed on the walls of the pyramids of the high concentration textured samples. The fact that

the a-Si:H layer cannot be clearly distinguished could be related to the above mentioned effect of lower electron signal from less dense layers deposited on rougher surfaces [126]. This suggests a poor coverage of the high roughness surface after the deposition process. However, the lack of signal can be also attributed to the microscope specific conditions, and further investigations with higher resolution methods (e.g. transmission electron microscopy) should be carried out in order to analyse the deposition of thin layers on this high roughness textured surface.

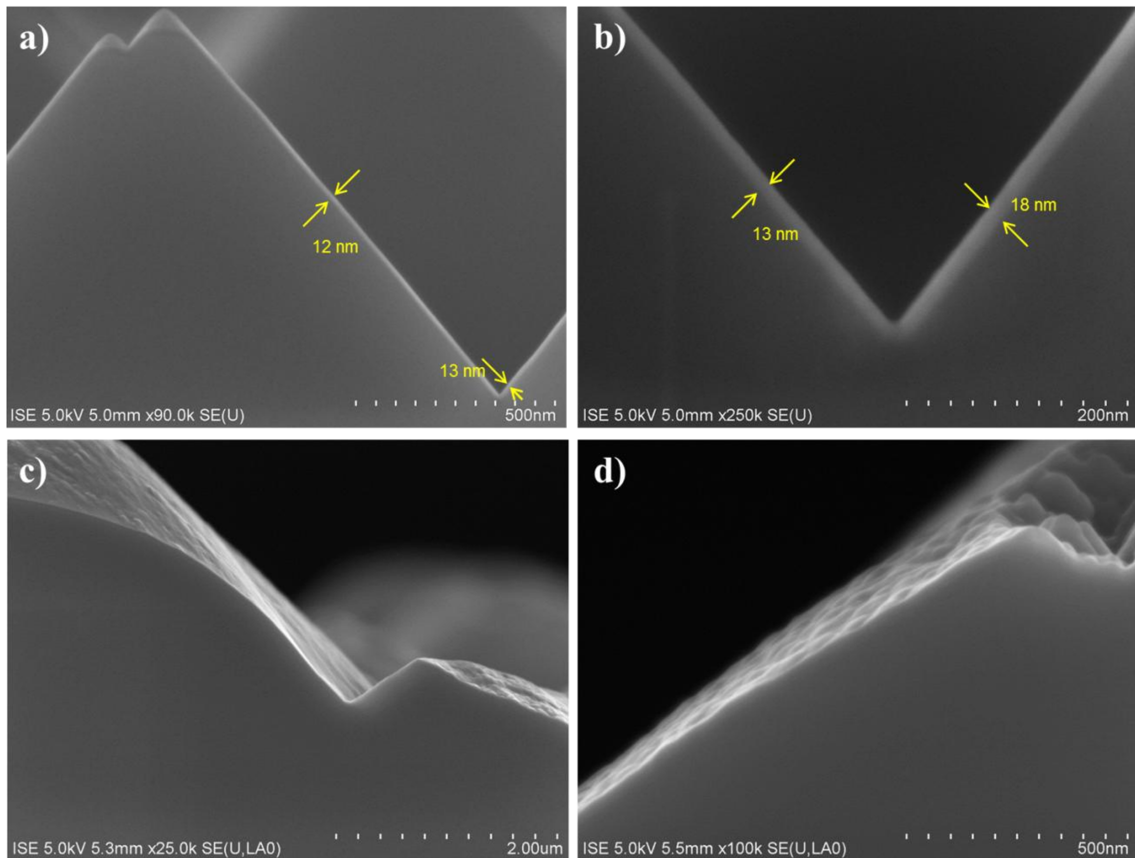

Figure 7.7. FE-SEM cross section images of textured samples with PECVD deposited layer of a-Si:H: a) and b) samples textured with 1 wt% Na_2CO_3 / 0.2 wt% $NaHCO_3$ solution; c) and d) samples textured with 20 wt% Na_2CO_3 / 4 wt% $NaHCO_3$ solution.

7.3 Ultra-low concentration Na_2CO_3/$NaHCO_3$ textured solar cells

Monocrystalline p-type (100) Cz silicon wafers (1.0-3.0 Ω·cm) were textured during 20 minutes with the high concentration S20/4 and the new proposed ultra-low concentration S1/0.2 solution.

- **Solution S20/4**: 20 wt% Na_2CO_3 / 4 wt% $NaHCO_3$ solution.
- **Solution S1/0.2**: 1 wt% Na_2CO_3 / 0.2 wt% $NaHCO_3$ solution.

The textured samples were characterized by means of SEM and AFM and their front reflectance was measured. The results are shown and discussed in chapter 5.1 (SEM results shown in Figure 5.1, AFM results shown in Figure 5.4, and reflectance spectra shown in Figure 5.2) and they are summarized in Table 7.2:

Table 7.2. Summary of the results of the characterization of the Cz silicon samples textured with S20/4and S1/0.2 solutions.

Texturization	SEM Pyramid size	AFM Nanoroughness	% $SWR_{400-1100}$
S20/4	10 µm width 3 µm height	High	23.0
S1/0.2	4 µm width 2 µm height	Low	19.5

Afterwards, a batch of screen printed phosphorous diffused solar cells was produced following the process described in section 4.1.2 with the textured wafers.

The result of the reflectance of the samples after the silicon nitride antireflection coating deposition is shown in Figure 7.8. The minimum reflectance is slightly shifted for the S20/4 textured sample compared to the S1/0.2 sample due to the influence of the surface area on the final thickness of the deposited layer. The $SWR_{400-900}$ was 3.6 and 3.7%, respectively.

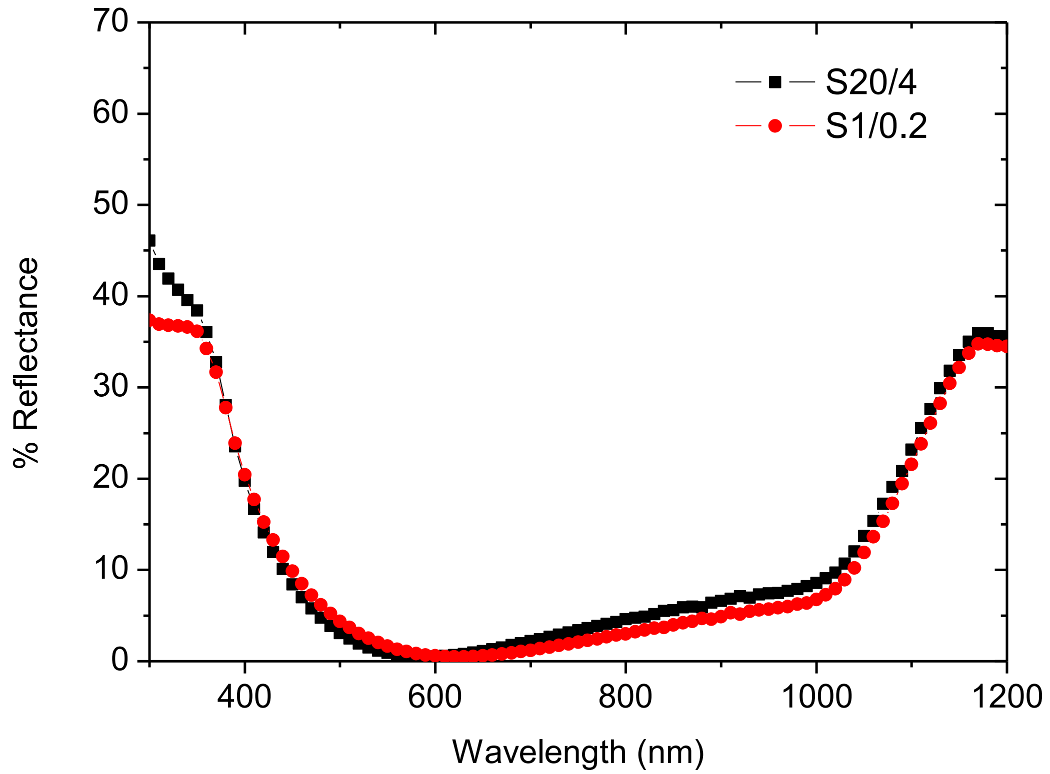

Figure 7.8. Reflectance curve of the samples textured S20/4 and S1/0.2 solutions with SiN_x ARC.

The electrical parameters of the solar cells were determined at 25° C from dark and illuminated *I-V* curve measurements using a solar simulator that provides AM1.5G illumination with an intensity of 1000 W/m^2. They are summarized in Table 7.3 and Table 7.4 and the illuminated and dark *I-V* curves are shown in Figure 7.9 and Figure 7.10 respectively.

Table 7.3. Electrical parameters of the textured solar cells extracted from the illuminated I-V curve (cell area = 96.04 cm^2).

Texturization	J_{sc} (mA/cm^2)	V_{oc} (mV)	*Eff* %	*FF* %
S20/4	33.8	600.9	15.4	75.5
S1/0.2	34.9	608.7	16.5	77.5

Table 7.4. Electrical parameters of the textured solar cells extracted from the fitting of the dark I-V curve to the two-diode model (cell area = 96.04 cm^2). n_1 and n_2 were fixed with the values of 1 and 2 respectively.

Texturization	R_S (ohm·cm^2)	R_P (ohm·cm^2)	J_{01} (mA/cm^2)	J_{02} (mA/cm^2)
S20/4	0.710	281642	$2.86 \cdot 10^{-12}$	$3.75 \cdot 10^{-8}$
S1/0.2	0.436	110338	$1.97 \cdot 10^{-12}$	$1.80 \cdot 10^{-8}$

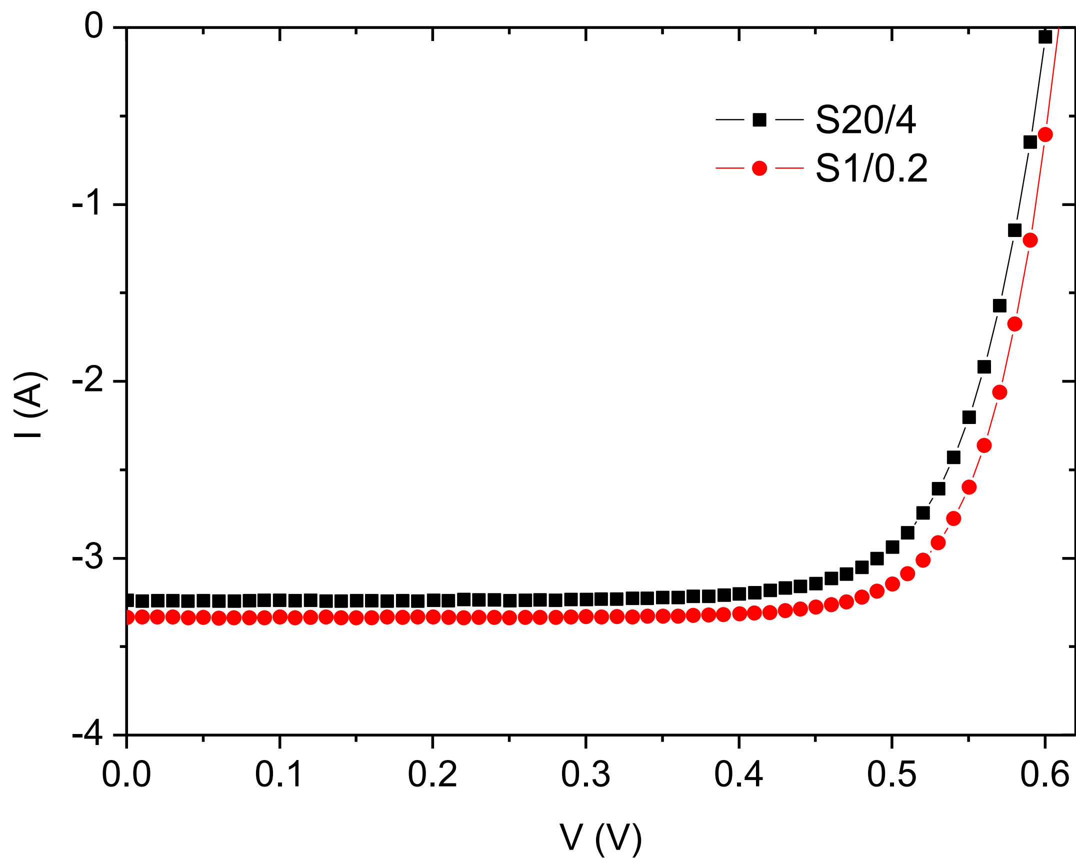

Figure 7.9. Illuminated I-V curves of the solar cells textured with S20/4 and S1/0.2 solutions.

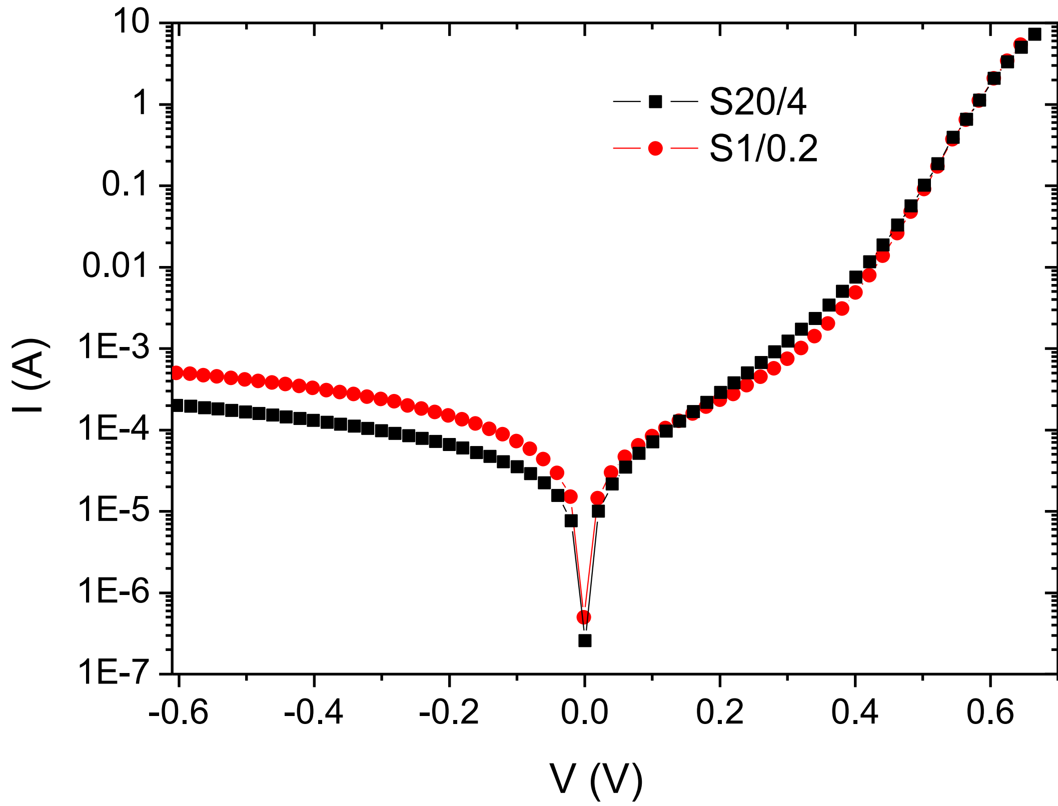

Figure 7.10. Dark I-V curves of the solar cells textured with S20/4 and S1/0.2 solutions.

A higher J_{SC} is observed for the S1/0.2 textured solution. However the increase in the J_{SC} does not only correspond to a decrease in the front reflection, according to the low difference in the $SWR_{400-900}$ after SiN_x deposition reported above. Thus, attention should be drawn to the series resistance R_S and V_{OC} exhibited by the S1/0.2 textured cell. The series resistance is not high enough to affect the J_{SC} for any of the cells (R_S should reach values over 10 Ωcm^2 to decrease I_{SC} [127]). Also an enhanced light trapping of the S1/0.2 texturization (not detected in the front reflection measurements) can contribute to its higher J_{SC}.

On the other hand, despite of that the solar cells do not seem to suffer from shunt problems, as shown by the high value of R_P and the results of a thermography analysis performed, the shunt resistance is lower for the S1/0.2 cell.

The higher V_{OC} of the cell S1/0.2 compared to the cell S20/4 can be attributed to the lower dark saturation current density J_{01}, and to the lower recombination current in the space charge region J_{02} of the S1/0.2 cell. This can be related to the smoother surface and lower nanoroughness of the walls of the pyramids of the new ultra-low texturization, reducing surface defects and facilitating the passivation of the surface, what enhances the V_{OC}.

The cell S1/0.2 shows also a larger *FF*, which is related to the previously exposed fact of a lower J_{02} and to its lower R_S. A higher J_{02} can be caused, despite by a higher recombination in the space charge region, by a non-uniform distributed series resistance [128]. The CELLO characterization of the cell confirms that an inhomogeneous series resistance can be the cause in the case of the cell textured with the S20/4 solution, as it is discussed below.

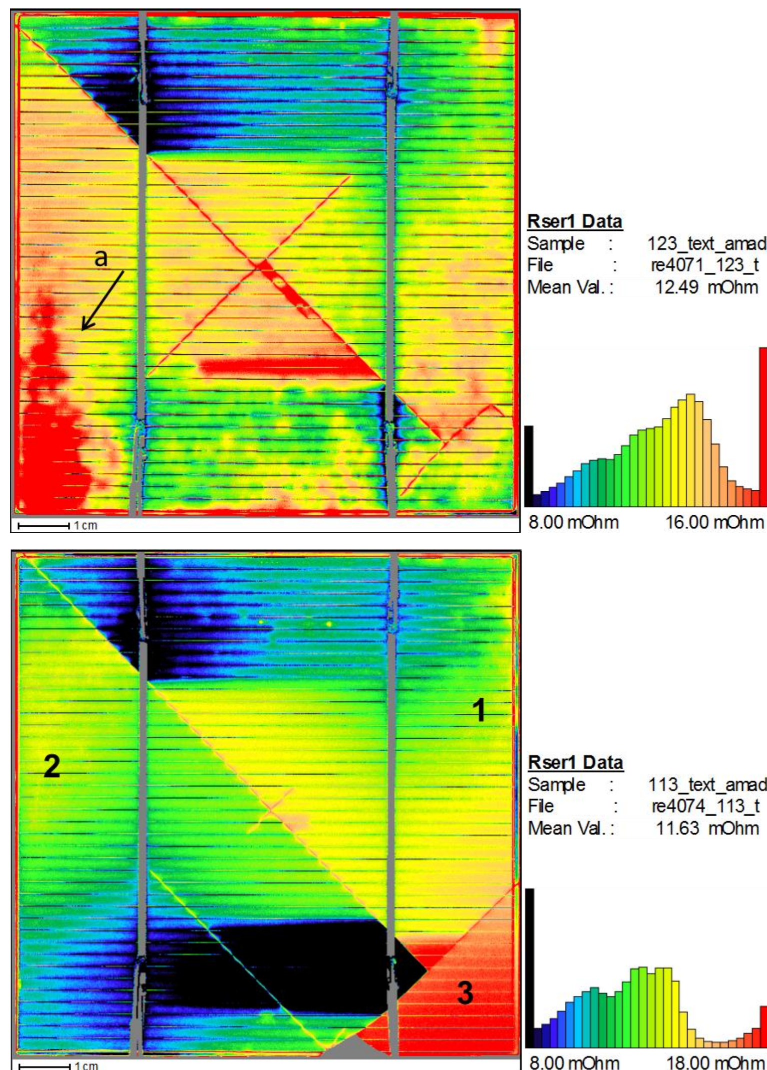

Figure 7.11. Series resistance Standard CELLO map. Cell textured with the S20/4 solution (top) and cell textured with S1/0.2 solution (bottom). Note: straight lines on both maps indicate handling induced cracks. Their effect on the series resistance is not of interest for our discussion.

A map of the values of R_S over the cell area performed by the CELLO technique [92, 94] is shown in Figure 7.11 for the S1/0.2 and the S20/4 textured cells. A series resistance problem can be observed for the S20/4 textured cell, which shows inhomogeneities in the R_S values and areas of high R_S (marker a). This can be attributed to a firing problem, due to larger pyramids for the S20/4 textured cell compared to the

S1/0.2 textured cell, which does not show such problem. A high emitter-grid finger contact resistance at the high R_S areas is suggested by the CELLO analysis. This can be caused by local differences in the temperature on the wafer surface during the firing process. The different surface area can lead to different thermal budget on the cell surface causing differences in the firing process (notice that both cells have been submitted to the same firing process). Thus, the firing process should be optimized for the S20/4 textured cells. The pyramid size is already known as a determining factor on the performance of textured solar cells [129]. The smaller pyramidal size of the S1/0.2 textured surface gives a benefit regarding to the processing of the solar cells as it facilitates the firing process and the formation of the electrical contacts, which can be a cause for the lower R_S and larger FF of the S1/0.2 cell. Also, a different emitter thickness and sheet resistance due to the different surface morphology (as discussed in section 7.2.1) of the S20/4 solar cell could influence the contact resistance.

By means of CELLO characterization, another interesting feature of the textured cells is observed. The maps of the linear response at I_{SC} to a short wavelength laser (405 nm) (Figure 7.12), show much higher (around 10%) average short circuit currents for the S1/0.2 textured cell. Despite of the fact that this CELLO measurement is not reflection corrected; the reflectance of both cells S20/4 and S1/0.2 at the wavelength of the laser (405 nm) is similar, as shown in the reflectance curve of the SiN_x coated samples (Figure 7.8). Therefore, the effect of differences on the front reflection on these maps is excluded. Low photocurrent areas around the busbars and around the grid fingers are observed in the map of the S20/4 solar cell (Figure 7.12, marker a). This can be caused by the incorporation of impurities from the Ag paste used in the screen printing into the junction during the firing [130, 131], which would increase the recombination in the space charge region [131], decreasing the obtained current. This would explain the observed higher J_{02} for the S20/4 cell. The coincidence of the observation of this problem on the bottom half of the cell S20/4, the same area where the R_S problem is observed, support the idea of local differences on the thermal budget within the surface of the S20/4 cell. An increased temperature in some areas could enhance the etching through of Ag crystallites and impurities. Jiang et al. [130] have found a damage of the junction due to an over-firing. They observed that Ag crystallites penetrate into the emitter (without creating shunts) by etching through the junction, but driving the junction into the bulk silicon, modifying the emitter thickness and concentration in some areas. Jiang et al. [130] suggest a mechanism of the junction damage based on Si recrystallization from Ag-Si melting mixture. This process also increases the contact resistance. On the other hand, Hoenig et al. [131] attribute the increased recombination in the space charge region caused by the firing process to the glass frit components as PbO and Bi_2O_3 which etch through the silicon and reach the junction.

A better front side response of the cell S1/0.2 could also be related to a lower surface recombination. The lower nanoroughness observed by AFM for the S1/0.2 textured surface is expected to decrease the surface recombination compared to the higher

nanoroughness of the S20/4 textured surface. The characteristics of the emitter of the cells could also have an influence. Further investigations and measurements should be performed to separate these effects from the clear effect of the over-firing observed, by accurate evaluation of the surface recombination of both textured surfaces S1/0.2 and S20/4.

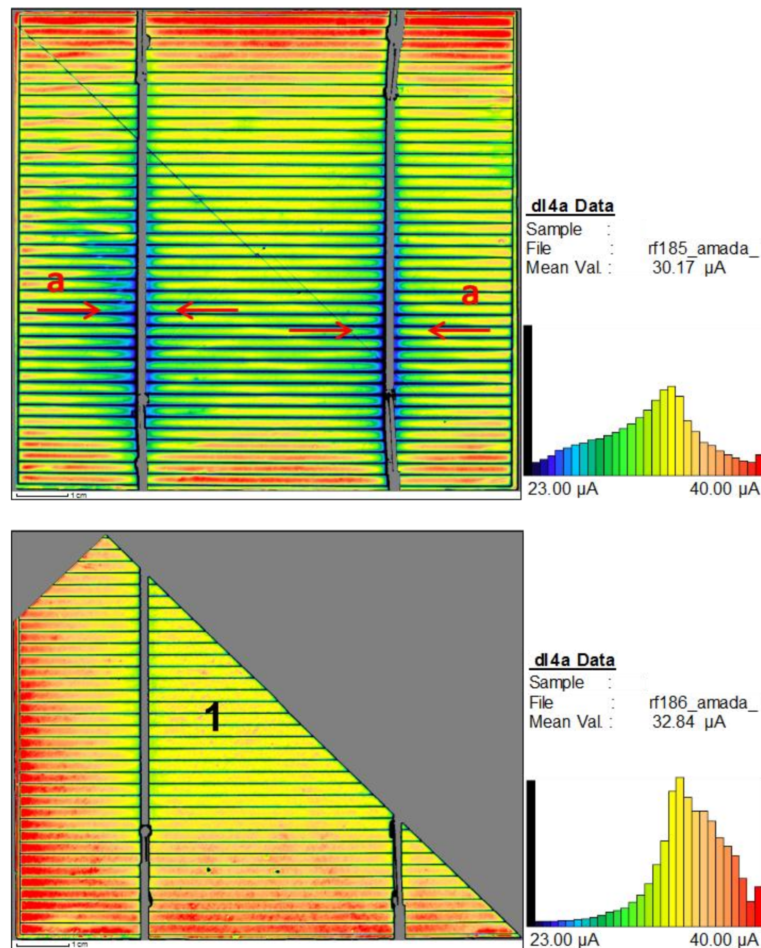

Figure 7.12. dI_{SC} CELLO map measured using a laser with a wavelength of 405 nm. Cell textured with the S20/4 solution (top) and cell textured with S1/0.2 solution (bottom). Note: the part of the cell S1/0.2 measured is the part labelled also as no. 1 in the R_S CELLO map of Figure 7.11, as the cell broke into three pieces due to the handling induced cracks.

The external and internal quantum efficiency curves of the cells have been determined and are shown in Figure 7.13. The cell textured with the S1/0.2 solution presents not only higher *EQE*, as expected due to its lower reflection curve, but also a higher *IQE*. The *IQE* is especially higher at short wavelengths in the case of the ultra-low solution textured cell, which agrees the conclusions extracted from the CELLO dI_{SC} maps. As shown in the dI_{sc} CELLO map measured with the 405 nm laser, a degradation of the junction caused by impurities from the silver paste which affects the space charge region recombination is observed. An improved passivation of the S1/0.2 front surface

compared to the S20/4 solution textured sample could also be suggested. This can be attributed to the lower roughness of the pyramid walls (see Figure 5.4), which could result in lower surface recombination velocity. The different formation of the emitter depending on the different surfaces morphologies, as shown in section 7.2.1, can also play a role. Thicker emitters can led to higher emitter recombination since the minority charge carriers have more probabilities to be generated and recombined within the emitter, but prevent on the other hand from shunt formation during the screen printing process [68]. The thickness and phosphorous concentration of the emitter can vary for the two different textured morphologies having an effect in the recombination within the emitter.

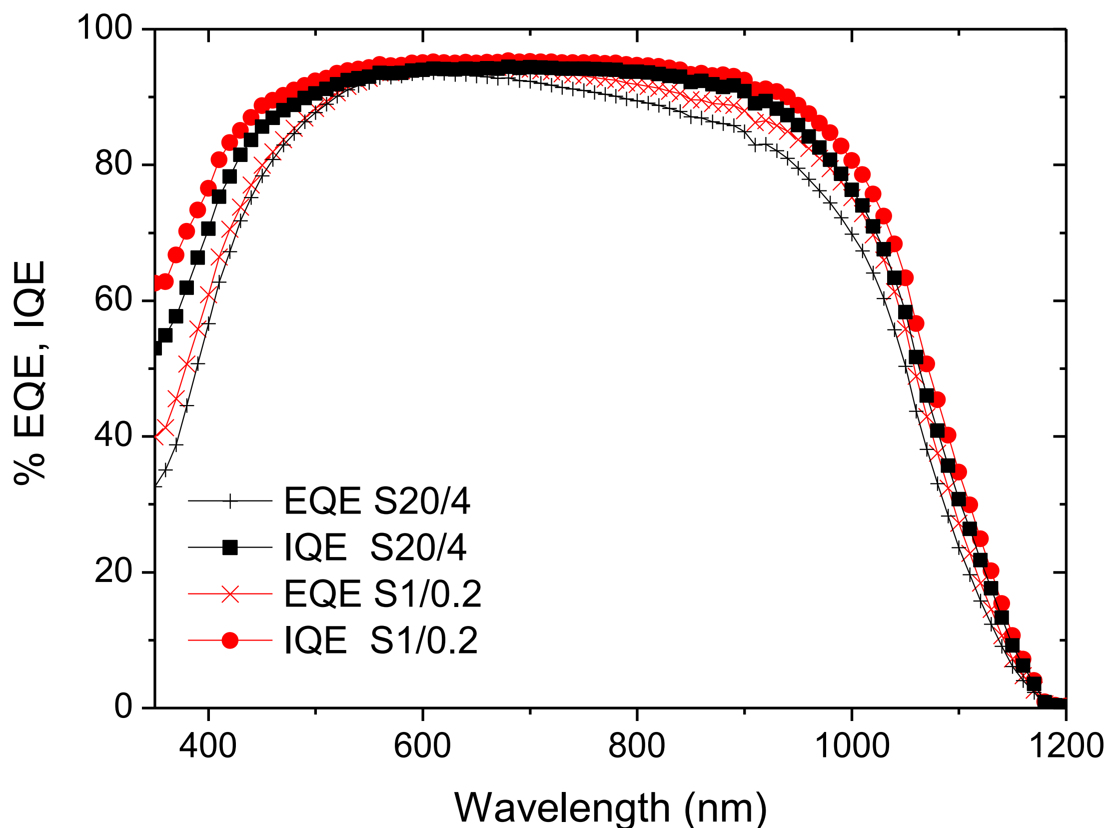

Figure 7.13. EQE and IQE curves of the solar cells textured with S20/4 and S1/0.2 solutions.

At long wavelengths, the *EQE* and *IQE* are also higher for the S1/0.2 compared to the S20/4 cell. A reason for this higher *IQE* at long wavelengths can be a lower back surface recombination for the S1/0.2 due to the lower nanoroughness observed on its pyramid facets. The significantly higher *IQE* for the S1/0.2 solution textured cell between 900 and 1050 nm can account for an enhanced light trapping of the textured cell, indicating enhanced absorption of long wavelength photons, and showing another advantage of the use of the ultra-low solution. It should be noticed that the *IQE* describes the ratio of the quantity of photons converted to electron-hole pairs which have been successfully collected to the quantity of photons which enter the cell (non-

front reflected). Once excluded the front reflection, the *IQE* at long wavelengths describes the fraction of photons entering the cell which are not recombined and do not pass through the back side of the cell, but back reflected and photoconverted. Therefore, the *IQE* at long wavelengths can be related to the light trapping of the cells.

7.4 Conclusions

In this chapter the use of $Na_2CO_3/NaHCO_3$ textured silicon for solar cells has been studied. For this purpose, the influence of the texturization morphology of the textured surface on the surface recombination velocity and the suitability of the textured silicon to be used as the substrate for the emitter formation and deposition of passivation and antireflection coatings have been evaluated. The proposed ultra-low concentration $Na_2CO_3/NaHCO_3$ process has been proved to be a feasible and efficient texturization method to be applied in industrial screen printed solar cells with phosphorous diffused emitter.

The surface recombination is, as expected, increased by the texturization. The analysis of two different textured surfaces shows that the different nanoroughness and micromorphology lead to different surface recombination. It has been possible to measure the nanoroughness directly on the pyramid facets. A lower nanoroughness measured on the pyramid wall is related to a lower surface recombination velocity.

The formation of the emitter on the ultra-low concentration $Na_2CO_3/NaHCO_3$ textured surfaces analysed by FE-SEM has shown thinner emitter thickness in textured surfaces compared to flat surfaces. The expected voltage for textured cells is decreased not only due to the higher surface area of the cell, but due to the characteristics of the thinner emitter formed. Also differences in the emitter thickness are observed at the valleys of the pyramids with respect to the thickness at the top of the pyramids. These differences in emitter thicknesses on the valleys compared to the top decrease by applying longer diffusion times. The extended time of the diffusion process also approximates the thickness of the emitter on the textured surface to the thickness of the emitter on the flat surface, being expected in this case similar open circuit voltages. The diffusion process for textured surfaces should be optimized for a desired emitter thickness and resulting sheet resistance, being possible to have emitters homogeneous in thickness, and with similar characteristics compared to flat surfaces, modifying the diffusion time and temperature.

The ultra-low concentration $Na_2CO_3/NaHCO_3$ textured surfaces has been shown to be compatible with the deposition of SiN_x and very thin (~15 nm) a-Si:H layers.

The screen printed solar cells produced with the new ultra-low concentration $Na_2CO_3/NaHCO_3$ texturization process show higher efficiency (16.5 %) compared to the solar cells produced by the high concentration $Na_2CO_3/NaHCO_3$ texturization (15.4 %). This enhanced efficiency can be attributed to different effects: the smaller size of

the pyramids which facilitates the solar cell processing together with a lower surface nanoroughness which favours the front side passivation and therefore the voltage and an improved light trapping effect which enhances the short circuit current. The high concentration $Na_2CO_3/NaHCO_3$ textured cell shows a high and inhomogeneously distributed series resistance due to a non-optimum firing, affecting J_{02}, which is increased. Also a possible degradation of the cell junction from the Ag paste of the grid is observed and attributed to the non-optimum firing. These problems are not observed for the ultra-low concentration $Na_2CO_3/NaHCO_3$ textured solar cell.

8 Summary and conclusions

In this thesis the texturization of monocrystalline (100) silicon by means of $Na_2CO_3/NaHCO_3$ has been studied with the aim of applying the texturing process to solar cells processing. After exposing the principles and fundamentals of silicon solar cells and silicon texturization, and the experimental methods employed, the experimental results of this work have been presented.

A novel $Na_2CO_3/NaHCO_3$ texturization process for the surface structuring of the monocrystalline silicon substrate, aimed to improve the silicon optical characteristics to be used in solar cells, has been proposed in this thesis. The proposed process consists in the wet chemical texturization of (100) oriented silicon with a new solution which has been designated as *ultra-low concentration $Na_2CO_3/NaHCO_3$ solution* containing of 1 wt% Na_2CO_3 and 0.2 wt% $NaHCO_3$ in deionised water. This solution is 12 times more diluted compared to the minimum concentrations found in the bibliography [61], and 20 times more diluted compared to the optimum established previously by our group [10]. The use of this process presents the following operation advantages:

- no additives like IPA are required, contrarily to NaOH or KOH based processes
- the lower concentration of chemicals compared to previously established $Na_2CO_3/NaHCO_3$ processes allows saving costs and simplifies a possible implementation in the industry since problems with precipitation of salts are avoided
- the process temperature at semi-industrial scale is 80-85 ºC, lower than the temperature of $Na_2CO_3/NaHCO_3$ texturization processes found in the literature [10, 61]
- the texturing solution can be reused several times
- it can be applied to different (100) silicon substrates, n- and p-type, as cut and shiny etched, Cz and FZ grown Si

The resulting morphology obtained with the ultra-low concentration $Na_2CO_3/NaHCO_3$ solution presents values of standard weighted reflectance (from 400 to 1100 nm) below 12 %, and smaller and more sharpened pyramids than the high concentration texturization process.

It has been possible to measure the nanoroughness by AFM directly on the pyramid near {111} oriented facets, showing that the ultra-low concentration $Na_2CO_3/NaHCO_3$ solution produces smoother facets, which is advantageous regarding to the mitigation of the surface recombination velocity.

Despite of the chemical concentration of the solution, different influencing parameters of the process, as the process temperature or the initial roughness of the substrate, have been studied. The initial roughness of the substrate has no significant influence on the morphology resulting from the texturization with the ultra-low concentration $Na_2CO_3/NaHCO_3$ solution, except for the case of n-Cz as cut Si, which shows slightly different characteristics regarding to the final morphology and reflectance.

A first estimation of the lifetime of the ultra-low concentrated solution was performed. The solution can be cooled down to room temperature and be reused at least eight times, and at least 46 wafers can be textured with 12 l of solution. However, further experiments should be carried out to know the maximum lifetime of the solution and to check the reproducibility of the process results after several reuses.

The ultra-low concentration $Na_2CO_3/NaHCO_3$ solution has been used to study the mechanism of pyramid formation on (100) silicon by means of AFM and SEM. During the first stages of the reaction, there exists an isotropic component of the process, and the morphology evolves differently for different initial surfaces. However, after several minutes of reaction different initial surfaces show similar morphologies. The nucleation of pyramids on the (100) silicon surface can be attributed to the following factors: defect nucleation, hydrogen bubbles, and reaction product masking. The pyramids are formed and disappear by layer by layer etching while some stabilized pyramids grow in size at the expense of neighbouring pyramids, having as a result a micrometric pyramidal-structured surface after several minutes.

The proposed ultra-low concentration $Na_2CO_3/NaHCO_3$ solution has been applied to a solar cell process as texturization step showing that this texturization process is not only compatible with operation requirements but with the resulting solar cell standards. The influence of the $Na_2CO_3/NaHCO_3$ texturing on solar cell processing steps, as formation of phosphorous doped emitter layer, passivation, and deposition of thin layers, has been studied. The FE-SEM SE dopant contrast image analysis shows differences in the emitter thickness of textured surfaces compared to saw damage etched surfaces, and within textured surfaces. The differences in the emitter thickness between the valleys and the tops of the pyramids are diminished for longer diffusion times, approaching also the sheet resistance of textured and saw damage etched surfaces and the expected V_{OC} on equivalent flat surfaces (disregarding the expected decrease on V_{OC} for textured surfaces due to its higher surface area or higher surface defect density). For the deposition of thin films of SiN_x and a-Si:H by means of PECVD a good coverage and conformality of the layer can be observed for the ultra-low concentration $Na_2CO_3/NaHCO_3$ textured surface.

The comparison of p-Cz phosphorous diffused and screen printed silicon solar cells produced with the high concentration and the new ultra-low $Na_2CO_3/NaHCO_3$ concentration solutions demonstrate an enhanced solar cell performance for the ultra-low $Na_2CO_3/NaHCO_3$ concentration process. The solar cell textured with the ultra-low

concentration $Na_2CO_3/NaHCO_3$ solution presents improved solar cell electrical parameters (*Eff*: 16.5 %, I_{SC}: 34.9 mA/cm^2, V_{OC}: 608.7 mV, *FF*: 77.5 %). The wavelength dependent *IQE* of the textured solar cells suggest a lower surface recombination and an enhanced light trapping for the cell textured with the ultra-low concentration $Na_2CO_3/NaHCO_3$ solution. Furthermore CELLO measurements performed on the textured cells show series resistance problems probably due to a non-optimized firing process for the high concentration $Na_2CO_3/NaHCO_3$ textured cell, while this is not observed for the ultra-low concentration $Na_2CO_3/NaHCO_3$ textured cell. The enhanced response of the ultra-low concentration $Na_2CO_3/NaHCO_3$ textured surface developed in this work is related to the smaller size of the pyramids to the solar which benefit cell processing and probably to the lower facets nanoroughness, compared to the high concentration $Na_2CO_3/NaHCO_3$ textured surface, which shows a low photocurrent at short wavelengths due to a junction degradation by impurity during the firing process. The here proposed texturization method is a promising candidate to be implemented in the industry.

Resumen y conclusiones

En la presente tesis se ha estudiado la texturización de silicio monocristalino (100) mediante disoluciones acuosas de Na_2CO_3/$NaHCO_3$ con el fin de aplicar dicho proceso a la producción de células fotovoltaicas. Tras la exposición de los principios y fundamentos relativos al funcionamiento de las células fotovoltaicas y la texturización de silicio, y de los métodos experimentales usados en este trabajo, se presentan los resultados experimentales de esta tesis.

En esta tesis se propone un método novedoso y original de texturización basado en disoluciones acuosas de Na_2CO_3/$NaHCO_3$ para la texturización de substratos de silicio monocristal con el objetivo de mejorar sus características ópticas para ser usado en la producción de células fotovoltaicas. El método propuesto consiste en la texturización química en disolución acuosa de silicio (100) con una novedosa disolución que se ha denominado *ultra-low concentration* $Na_2CO_3/NaHCO_3$ (por su extremadamente baja concentración de reactivos) y que contiene 1 % de Na_2CO_3 y 0.2 % de $NaHCO_3$ en peso en agua desionizada. Esta disolución contiene 12 veces menor cantidad de reactivos químicos que la disolución con la mínima concentración que puede encontrarse en la bibliografía [61], y 20 veces menor cantidad de reactivos que la disolución óptima establecida previamente por nuestro grupo [10]. Este nuevo proceso presenta varias ventajas a nivel operativo:

- no se requieren aditivos como, por ejemplo, isopropanol
- la menor concentración de reactivos químicos en comparación a los anteriores procesos basados en Na_2CO_3/$NaHCO_3$ permite una importante reducción de costes y simplifica la implementación de la texturización mediante Na_2CO_3/$NaHCO_3$ en la industria, ya que se evitan problemas como la precipitación de sales en los equipos derivados de la alta concentración de los reactivos
- la temperatura del proceso a escala semi-industrial es de 80-85 ºC, menor que la temperatura de procesos anteriores basados en Na_2CO_3/$NaHCO_3$ descritos en la literatura [10, 61]
- la disolución texturizante puede ser reusada varias veces consecutivas
- el proceso se puede aplicar a diferentes tipos de substratos de silicio (100): Si tipo n y tipo p, Si *as cut* y pulido, Si tipo Cz y FZ.

La morfología del silicio resultante de la texturización con la nueva disolución *ultra-low concentration* $Na_2CO_3/NaHCO_3$ presenta valores de reflectancia estándar ponderada con el espectro solar (entre 400 y 1100 nm) por debajo del 12 %, y pirámides más pequeñas

y definidas en su forma que las obtenidas mediante los anteriores procesos con disoluciones de alta concentración de $Na_2CO_3/NaHCO_3$.

Ha sido posible medir la nanorugosidad de la superficie del silicio directamente en las facetas cuasi {111} que constituyen las caras de las pirámides mediante AFM, demostrando que la disolución *ultra-low concentration* $Na_2CO_3/NaHCO_3$ produce facetas de menor nanorugosidad en comparación con el proceso a alta concentración, lo que resulta beneficioso a la hora de reducir la velocidad de recombinación superficial de los portadores de carga generados.

Además de la concentración de reactivos químicos en la disolución, se han estudiado diversos parámetros que influyen en el proceso, como la temperatura del proceso o la rugosidad inicial del substrato. Se ha demostrado que la rugosidad inicial no ejerce una influencia significativa en el resultado final mediante la texturización con *ultra-low concentration* $Na_2CO_3/NaHCO_3$, excepto para el caso de Si Cz tipo n, que presenta características de morfología y reflectancia ligeramente diferentes tras la texturización.

Se ha realizado una primera estimación del tiempo de vida de la disolución *ultra-low concentration* $Na_2CO_3/NaHCO_3$. La disolución se puede enfriar a temperatura ambiente y ser reusada al menos ocho veces, siendo texturizadas al menos 46 obleas con 12 l de disolución. Sin embargo, deben realizarse más experimentos para conocer de manera más exacta el tiempo de vida máximo de la disolución y comprobar la reproducibilidad del proceso después de varios usos de la disolución.

La disolución *ultra-low concentration* $Na_2CO_3/NaHCO_3$ se ha aplicado al estudio del mecanismo de formación de las pirámides en silicio (100), estudio realizado mediante AFM y SEM. Durante las etapas iniciales se ha observado que existe un componente isotrópico de la reacción y la morfología evoluciona de manera diferente en distintos tipos de substratos con distintas características iniciales. Sin embargo, después de varios minutos de reacción los substratos con distintas características iniciales presentan morfologías similares. Se ha determinado que la nucleación de pirámides en superficies de silicio (100) puede atribuirse a los siguientes factores: nucleación debida a defectos en el cristal, burbujas de hidrógeno, y productos de reacción que actúan como máscara. Las pirámides se forman y desaparecen posteriormente por un mecanismo de *decapado*, mientras algunas pirámides se estabilizan y crecen en tamaño a expensas de las pirámides vecinas, resultando en una superficie estructurada con pirámides micrométricas después de varios minutos.

La nueva la disolución *ultra-low concentration* $Na_2CO_3/NaHCO_3$ propuesta se ha aplicado a un proceso de producción de células fotovoltaicas en el paso de texturización, demostrando que el proceso de texturización diseñado es compatible no sólo con los requerimientos de operación del proceso de producción de células, sino con los estándares de calidad de las células fotovoltaicas resultantes del proceso. Se ha estudiado la influencia de la texturización mediante $Na_2CO_3/NaHCO_3$ en los pasos de fabricación de células fotovoltaicas como la formación del emisor, la pasivación

superficial y la deposición de capas finas. El análisis de contraste de imagen de electrones secundarios mediante FE-SEM realizado muestra que hay diferencias en el espesor del emisor de fósforo formado en superficies texturizadas en comparación con el emisor formado en superficies planas. Dentro de la superficie texturizada también existen diferencias en el espesor del emisor en los valles y picos de las pirámides. Se observa que las diferencias en el espesor en valles y picos disminuyen con el uso de procesos de difusión de fósforo de mayor duración en tiempo, aproximándose además la resistencia de capa final de las superficies difundidas texturizadas y planas y el voltaje en circuito abierto esperado en una superficie plana de equivalente área superficial (sin contar con la reducción de voltaje esperada en células texturizadas debido al incremento de área superficial). Se ha observado una buena cobertura de la superficie y buena conformalidad de las capas finas de nitruro de silicio y silicio amorfo depositadas mediante PECVD en superficies texturizadas con la disolución *ultra-low concentration* $Na_2CO_3/NaHCO_3$.

La comparación de células fotovoltaicas fabricadas en silicio Cz tipo p con emisor de fósforo difundido y metalización realizada mediante *screen printing*, producidas con el anterior proceso de texturización mediante $Na_2CO_3/NaHCO_3$ a alta concentración y el nuevo proceso *ultra-low concentration* $Na_2CO_3/NaHCO_3$ demuestra que las células producidas con el nuevo proceso *ultra-low concentration* $Na_2CO_3/NaHCO_3$ presentan mejores propiedades y mejor funcionamiento. Los parámetros eléctricos de las células texturizadas con la disolución *ultra-low concentration* $Na_2CO_3/NaHCO_3$ resultan mejorados (*Eff*: 16.5 %, I_{SC}: 34.9 mA/cm^2, V_{OC}: 608.7 mV, *FF*: 77.5 %). La eficiencia cuántica interna dependiente de la longitud de onda de los fotones incidentes sugiere una menor recombinación superficial y mayor efecto *light trapping* (captura de luz) para la célula texturizada con la disolución *ultra-low concentration* $Na_2CO_3/NaHCO_3$. Además, la caracterización CELLO realizada en las células producidas muestra problemas de alta resistencia serie en la célula texturizada mediante la disolución de $Na_2CO_3/NaHCO_3$ a alta concentración, que probablemente se deba a un proceso de formación de los contactos no óptimo, mientras que en el caso de la célula texturizada con la disolución *ultra-low concentration* $Na_2CO_3/NaHCO_3$ el problema de resistencia serie no se observa. La mejor respuesta de la superficie texturizada mediante la disolución *ultra-low concentration* $Na_2CO_3/NaHCO_3$ desarrollada en esta tesis al proceso de producción de células fotovoltaicas se relaciona con el menor tamaño de las pirámides formadas y probablemente con la menor nanorugosidad de las facetas de las pirámides en comparación con la superficie texturizada mediante la disolución de $Na_2CO_3/NaHCO_3$ a alta concentración, que muestra baja fotocorriente a bajas longitudes de onda debido a una degradación de la unión n-p debido a impurezas introducidas durante el proceso de *firing*. El método de texturización propuesto en esta tesis en un candidato prometedor para ser implementado a nivel industrial.

References

[1] O. Edenhofer, R. Pichs-Madruga, Y. Sokona, K, Seyboth, P, Matschoss, S. Kadner, T, Zwickel, P, Eickemeier, G, Hansen, S, Schloemer, C, von Stechow, *Renewable Energy Sources and Climate Change Mitigation. Special Report of the Intergovernmental Panel on Climate Change*, IPCC, Cambridge University Press, 2012, USA.

[2] G. Masson, M. Latour, D. Biancardi, C. Winneker, *Global Market Outlook for Photovoltaics until 2016*, European Photovoltaic Industry Association, 2012.

[3] A. Jäger-Waldau, *PV Status Report 2011: Research, Solar Cell Production and Market Implementation of Photovoltaics*, European Commission DG JRC, 2011.

[4] *Solar Photovoltaics Competing in the Energy Sector. On the road to competitiveness*, European Photovoltaic Industry Association, 2011.

[5] C. A. Wolden, J. Kurtin, J. B. Baxter, I. Repins, S. E. Shaheen, J. T. Torvik, A. A. Rockett, V. M. Fthenakis, E. S. Aydil, *Photovoltaic manufacturing: Present status, future prospects, and research need*, J. Vac. Sci. Technol. A 29 (2011) 030801.

[6] *International Technology Roadmap for Photovoltaic (ITRPV) Results 2011*, SEMI PV Group, 2012.

[7] T. Markvart, L. Castañer, *Practical Handbook of Photovoltaics: Fundamentals and Applications*, Elsevier, 2003, UK.

[8] A. Luque, S. Hegedus, *Handbook of photovoltaic science and engineering*, John Wiley & Sons Ltd., 2003, UK.

[9] Y. Nishimoto, K. Namba, *Investigation of texturization for crystalline silicon solar cells with sodium carbonate solutions*, Sol. Energy Mater. Sol. Cells 61 (2000) p. 393.

[10] N. Marrero, B. González-Díaz, R. Guerrero-Lemus, D. Borchert, C. Hernández-Rodríguez, *Optimization of sodium carbonate texturization on large-area crystalline silicon solar cells*, Sol. Energy Mater. Sol. Cells 91 (2007) p. 1943.

[11] A. Goetzberger, J. Knobloch,B. Voss. *Crystalline Silicon Solar Cells*, John Wiley & Sons Ltd., 1998, UK.

[12] P. Würfel, *Physics of solar cells. From principles to new concepts*, Wiley-VCH

Verlag, 2005, Germany.

[13] W. Shockley, W. T. Read, Jr., *Statistics of the Recombinations of Holes and Electrons*, Phys. Rev. 87 (1952) p. 835.

[14] G. Aberle, *Crystalline silicon solar cells. Advanced Surface passivation and analysis,* Centre for Photovoltaic Engineering. University of New South wales, 1999, Australia.

[15] W. G. J. H. M. van Sark, L. Korte, F. Roca, *Physics and technology of amorphous-crystalline heterostructure silicon solar cells*, Springer-Verlag Berlin Heidelberg, 2011, Germany.

[16] H. Angermann, W. Henrion, A. Röseler, M. Rebien, *Wet-chemical passivation of Si(111)- and Si(100)-substrates*, Mater. Sci. Eng. B 73 (2000) p. 178.

[17] H. Angermann, W. Henrion, M. Rebien, A. Röseler, *Wet-chemical passivation and characterization of silicon interfaces for solar cell applications*, Sol. Energy Mater. Sol. Cells 83 (2004) p. 331.

[18] F. Duerinckx, J. Szlufcik, *Defect passivation of industrial multicrystalline solar cells basedon PECVD silicon nitride*, Sol. Energy Mater. Sol. Cells 72 (2002) p. 231.

[19] J. S. Kang, D.K. Schroder, *Gettering in silicon*, J. Appl. Phys. 65 (1989) p. 2974.

[20] I. Périchaud, *Gettering of impurities in solar silicon,* Sol. Energy Mater. Sol. Cells 72 (2002) p. 315.

[21] A. Uhlir, *Electrolytic Shaping of Germanium and Silicon*, Bell System Tech. J. 35 (1956) p. 333.

[22] J. M. Crishal, A. L. Harrington, *A selective etch for elemental silicon*, Electrochem. Soc. Extended Abstract, Spring Meeting, Los Angeles (1962) Abstr. 89, p. 202.

[23] R. M. Finne, D. L. Klein, *A water soluble amine complexing agent system for etching silicon*, J. Electrochem. Soc. 114 (1967) p. 965.

[24] D.B. Lee, *Anisotropic etching of silicon*, J. App. Phys. 40 (1969) p. 4569.

[25] H. G. Rudenberg, B. Dale, Radiant Energy Transducer, US Patent 3, 150, 999, 17 February 1961.

[26] J. Haynos, J. Allison, R. Arndt, A. Meulenberg, *The COMSAT nonreflective silicon solar cell: a second generation improved cell*, Proceedings of International Conf. on Photovoltaic Power Generation, Hamburg (1974) p. 487.

[27] F. Restrepo, C.E. Backus, *On black cells or the tetrahedral texturing of a silicon surface*, IEEE Trans. Electron Devices 23 (1976) p. 1195.

[28] M. A. Green, *Self-consistent optical parameters of intrinsic silicon at 300 K including temperature coefficients*, Sol. Energy Mater. Sol. Cells 92 (2008) p. 1305.

[29] S. C. Baker-Finch, K. R. McIntosh, *Reflection of normally incident light from silicon solar cells with pyramidal texture*, Prog. Photovolt: Res. Appl. 19 (2011) p. 406.

[30] P. A. Basore, D. A. Clugston, PC1D version 5.9. Copyright © 2003. University of New South Wales.

[31] M. A. Green, *Limits on the open-circuit voltage and efficiency of silicon solar cells imposed by intrinsic auger processes*, IEEE Trans. Electron Devices 31 (1984) p. 671.

[32] R. J. Roedel, P.M. Holm, *The design of anisotropically etched III-V solar cells*, Solar Cells 11 (1984) p. 221.

[33] P. Campbell, M. Green, *Light trapping properties of pyramidally textured surfaces*, J. Appl. Phys. 62 (1987) p. 243.

[34] A. W. Smith, A. Rohatgi, *Ray tracing analysis of the inverted pyramid texturing geometry for high efficiency silicon solar cells*, Sol. Energy Mater. Sol. Cells 29 (1993) p. 37.

[35] S. C. Baker-Finch, K. R. McIntosh, *One dimensional photogeneration profiles in silicon solar cells with pyramidal texture*, Prog. Photovolt: Res. Appl. 20 (2012) p. 51.

[36] J. C. Zolper, S. Narayanan, S. R. Wenham, M. A. Green, *16.7 % efficient, laser textured, buried contact polycrystalline silicon solar cell*, Appl. Phys. Lett. 55 (1989) p. 2363.

[37] M. Schnell, R. Ludemann, S. Schaefer, *Plasma surface texturization for multicrystalline silicon solar cells*, Proceedings of the 28th IEEE Photovoltaic Specialists Conference, Anchorage (2000) p.367.

[38] T. Hattori, *Ultraclean surface processing of silicon wafers. Secrets of VLSI manufacturing*, Springer-Verlag Berlin Heidelberg, 1998, Germany.

[39] K. A. Reinhardt, W. Kern, *Handbook of silicon wafer cleaning technology*, 2nd Ed., William Andrew Inc., 2008, USA.

[40] M. Hofmann, J. Rentsch, R. Preu, *Dry plasma processing for industrial crystalline silicon solar cell production*, Eur. Phys. J. Appl. Phys. 52 (2010) p.

11101.

[41] S. M. Rossnagel, J. J. Cuomo, W. D. Westwood, *Handbook of plasma processing technology: fundamentals, etching, deposition and surface interactions*, Noyes Publications, 1990, USA.

[42] W. N.G. Hitchon, *Plasma processes for semiconductor fabrication*, Cambridge University Press, 1999, UK.

[43] K. R. Williams, R. S. Muller, *Etch rates for micromachining processing*, Journal of Microelectromechanical Systems, 5 (1996) p. 256.

[44] Y. Saito, T. Kosuge, *Honeycomb-textured structures on crystalline silicon surfaces for solar cells by spontaneous dry etching with chlorine trifluoride gas*, Sol. Energy Mater. Sol. Cells 91 (2007) p. 1800.

[45] S. Q. Xiao, S. Xu *Plasma-aided fabrication in Si-based photovoltaic applications: an overvi*ew, J. Phys. D: Appl. Phys. 44 (2011) 174033.

[46] D. S. Ruby, S. H. Zaid, S. Narayanan, *Plasma-texturization for multicrystalline silicon solar cells*, Proceedings of the 28th IEEE Photovoltaic Specialists Conference, Anchorage (2000) p.75.

[47] M. D. Abbott, P. J. Cousins, F. W. Chen, J.E. Cotter, *Laser-induced defects in crystalline silicon solar cells*, Proceedings of the 31st IEEE Photovoltaic Specialists Conference, Orlando (2005) p. 1241.

[48] M. D. Abbott, P. J. Cousins, *Optical and electrical properties of laser texturing for high-efficiency solar cells*, Prog. Photovolt: Res. Appl. 14 (2006) p. 225.

[49] K. B. Nayak, V. V. Iyengar, M. C. Gupta, *Efficient light trapping in silicon solar cells by ultrafast-laser-induced self-assembled micro/nano structures*, Prog. Photovolt: Res. Appl. 19 (2011) p. 631.

[50] D.H. Macdonald, A. Cuevas, M.J. Kerr, C. Samundsett, D. Ruby, S. Winderbaum, A. Leo, *Texturing industrial multicrystalline silicon solar cells*, Solar Energy 76 (2004) p. 277.

[51] P. Panek, M. Lipinski, J. Dutkiewicz, *Texturization of multicrystalline silicon by wet chemical etching for silicon solar cells*, Journal of Materials Science 40 (2005) p. 1459.

[52] H. Robbins, B. Schwartz, *Chemical etching of silicon. I. The system HF,* HNO_3*, and* H_2O, J. Electrochem. Soc. 106 (1959) p. 505.

[53] H. Robbins, B. Schwartz, *Chemical etching of silicon. II. The system HF,* HNO_3*, and* H_2O*, and* $HC_2H_3O_2$, J. Electrochem. Soc. 107 (1960) p. 108.

[54] G. Zhang, *Electrochemistry of silicon and its oxide*, Kluwer Academic Pub, New York, 2001, USA.

[55] M. Mehregany, S.D. Senturia, *Anisotropic etching of silicon in hydrazine*, Sensors and Actuators 13 (1988) p. 375.

[56] U. Gangopadhyay, S.K. Dhungel, A.K. Mondal, H. Saha, J. Yi, *Novel low-cost approach for removal of surface contamination before texturization of commercial monocrystalline silicon solar cell*s, Sol. Energy Mater. Sol. Cells 91 (2007) p. 1147.

[57] H. Seidel, L. Csepregi, A. Heuberger, H. Baumgärtel, *Anisotropic etching of crystalline silicon in alkaline solutions I. Orientation dependence and behavior of passivation layers,* J. Electrochem. Soc. 137 (1990) p. 3612.

[58] E.D. Palik, H.F. Gray, P.B. Klein, *A Raman study of etching silicon in aqueous KOH*, J. Electrochem. Soc. 130 (1983) p. 956.

[59] E. D. Palik, V. M. Bermudez, O. J. Glembocki, *Ellipsometric study of orientation-dependent etching of silicon in aqueous KOH*, J. Electrochem. Soc. 132 (1985) p. 871.

[60] P. Allongue, V. Costa-Kieling, H. Gerischer, *Etching of silicon in NaOH solutions. II. Electrochemical studies of n-Si (111) and (100) and mechanism of the dissolution*, J. Electrochem. Soc. 140 (1993) p. 1018.

[61] W. Sparber, O. Schultz, D. Biro, G. Emanuel, R. Preu, A. Poddey, D. Borchert, *Comparison of texturing methods for monocrystalline silicon solar cells using KOH and* Na_2CO_3, Proceedings of the 3rd World Conference on Photovoltaic Energy Conversion, Osaka (2003) p. 1372.

[62] I. Melnyk, E. Wefringhaus, M.McCann, A. Helfricht, A. Hauser, P. Fath, Na_2CO_3 *as an alternative to NaOH/IPA for texturisation of monocrystalline silicon*, Proceedings of the 19th European Photovoltaic Solar Energy Conference, Paris (2004) p.1091.

[63] B. Vallejo, M. González- Mañas, J. Martínez-López, M.A. Caballero, *On the texturization of monocrystalline silicom with sodium carbonate solutions*, Solar Energy 81 (2007) p. 565.

[64] H. Li, W. Liu, A. Liu, F. Qiao, Z. Hua, Y. Liu, *Metal grids-based texturization of monocrystalline silicon wafers for solar cells*, Sol. Energy Mater. Sol. Cells 94 (2010) p. 942.

[65] H. Angermann, J. Rappich, L. Korte, I. Sieber, E. Conrad, M. Schmidt, K. Hübener, J. Polte, J. Hauschild, *Wet –chemical passivation of atomically flat and structured silicon substrates for solar cell application*, Appl. Surf. Sci. 254

(2008) p. 3615.

[66] H. Angermann, L. Korte, J. Rappich, E. Conrad, I. Sieber, M. Schmidt, K. Hübener, J. Hauschild, *Optimisation of electronic interface properties of a-Si:H/c-Si hetero-junction solar cells by wet-chemical surface pre-treatment*, Thin Solid Films 516 (2008) p. 6775.

[67] W. Kern, D. Puotinen, *Cleaning solutions based on hydrogen peroxide for usee in silicon semiconductor technology*, RCA Rev. 31 (1970) p. 187.

[68] A. Bentzen, *Phosphorus diffusion and gettering in silicon solar cells*, PhD thesis, 2006, University of Oslo.

[69] A. Bentzen, A. Holt, J. S. Christensen, B. G. Svensson, *High concentration in-diffusion of phosphorus in Si from a spray-on source*, J. Appl. Phys. 99 (2006) 064502 .

[70] S. Peters, *Rapid thermal processing of crystalline silicon materials and solar cells*, PhD thesis, 2004, University of Konstanz.

[71] R. Hezel, R. Schörner, *Plasma Si nitride-A promising dielectric to achieve high-quality silicon MIS/IL solar cells*, J. Appl. Phys. 52 (1981) p. 3076.

[72] M. J. Kerr, A. Cuevas, *Recombination at the interface between silicon and stoichiometric plasma silicon nitride*, Semicond. Sci. Technol. 17 (2002) p. 166.

[73] A. G. Aberle, T. Lauinger, J. Schmidt, R. Hezel, *Injection level dependent surface recombination velocities at the silicon plasma silicon nitride interface*, Appl. Phys. Lett. 66, (1995) p. 2828.

[74] T. Lauinger, J. Schmidt, A. G. Aberle, R. Hezel, *Record low surface recombination velocities on 1 Ωcm p-silicon using remote plasma silicon nitride passivation*, Appl. Phys. Lett. 68 (1996) p. 1232.

[75] S. Keipert-Colberg, *Multikristalline Siliziumsolarzellen mit Siliziumoxid-Siliziumnitrid-Rückseitenpassivierung*, PhD thesis, 2010, University of Kiel.

[76] J. Ziegler, A. Montesdeoca-Santana, D. Platt, S. Hohage, R. Guerrero- Lemus, D. Borchert, *Influences of p-and n-doped Czochralski base material on the performance of silicon based heterojunction solar cells*, Jpn. J. Appl. Phys. 51 (2012) 10NA03.

[77] G. Schubert, F. Huster, P. Fath, *Physical understanding of printed thick-film front contacts of crystalline Si solar cells. Review of existing models and recent developments*, Sol. Energy Mater. Sol. Cells 90 (2006) p. 3399.

[78] A. Mette, *New concepts for front side metallization of industrial silicon solar cells*, PhD thesis, 2007, University of Freiburg.

[79] J. Szlufcik, S. Sivoththaman, J. F. Nijs, R. P. Mertens, R. Van Overstraeten, *Low-cost industrial technologies of crystalline silicon solar cells*, Proceedings of the IEEE, 85 (1997) p. 711.

[80] R. Brendel, *Thin-film crystalline silicon solar cells: physics and technology,* Wiley-VCH Verlag, 2003, Germany.

[81] H. Lüth, *Solid surfaces, interfaces and thin films*, Springer-Verlag Berlin Heidelberg, 1993, Germany.

[82] J. Goldstein, D.E. Newbury, D.C. Joy, C.E. Lyman, P. Echlin, E. Lifshin, L. Sawyer, J.R. Michael, *Scanning Electron Microscopy and X-ray Microanalysis*, 3rd Ed., Springer Netherlands, 2005, Netherlands.

[83] K. Shimizu, T. Mitani, *New Horizons of Applied Scanning Electron Microscopy*, Springer-Verlag Berlin Heidelberg, 2010, Germany.

[84] A. Montesdeoca-Santana, J. Ziegler, S. Lindekugel, E. Jiménez-Rodríguez, S. Keipert-Colberg, S. Müller, C. Krause, D. Borchert, R. Guerrero-Lemus, *A comparative study on different textured surfaces passivated with amorphous silicon*, Physica Status Solidi C 8 (2011) p. 747.

[85] I. Horcas, R. Fernández, J. M. Gómez-Rodríguez, J. Colchero, J. Gómez-Herrero, A. M. Baró, *WSXM: A software for scanning probe microscopy and a tool for nanotechnology*, Rev. Sci. Instrum. 78, (2007) 013705.

[86] M. Kunst, G. Beck, *The study of charge carrier kinetics in semiconductors by microwave conductivity measurements*, J. Appl. Phys. 60 (1986) p. 3558.

[87] R. Sinton, A. Cuevas, *Contactless determination of current-voltage characteristics and minority-carrier lifetimes in semiconductors from quasi-steady-state photoconductance data*, Appl. Phys. Lett. 69 (1996) p. 2510.

[88] A.G. Aberle, J. Schmidt, R. Brendel, *On the data analysis of light-biased photoconductance decay measurements*, J. Appl. Phys. 79 (1996) p. 1491.

[89] R. Sinton, D. Macdonald, *WCT-120 Photoconductance Lifetime Tester. User Manual*, Sinton Consulting, Inc. 2006.

[90] A. Cuevas, D. Macdonald, *Measuring and interpreting the lifetime of silicon wafers*, Solar Energy 76 (2004) p. 255.

[91] G. S. May, C.J. Spanos, *Fundamentals of Semiconductors Manufacturing and Process Control*, John Wiley & Sons Inc., 2006, USA.

[92] J. Carstensen, G. Popkirov, J. Bahr, H. Föll, *CELLO: an advanced LBIC measurement techniquefor solar cell local characterization*, Sol. Energy Mater. Sol. Cells 76 (2003) p. 599.

[93] J. Carstensen, A. Schütt, G. Popkirov, H. Föll, CELLO measurement technique for local identification and characterization of various types of solar cell defects, Phys. Status Solidi C 8 (2011) p. 1342.

[94] J. Carstensen, A. Schütt, H. Föll, *CELLO local solar cell resistance maps: Modeling of data and correlation to solar cell efficiency*, Proceedings of the 22nd European Photovoltaic Solar Energy Conference, Milan (2007) p. 337.

[95] W. M. Haynes, *CRC Handbook of Chemistry and Physics*, 92nd Edition, Internet Version 2012.

[96] H. Seidel, *The mechanism of anisotropic, electrochemical silicon etching in alkaline solutions*, Solid-State Sensor and Actuator Workshop, IEEE 4th Technical Digest., Hilton Head Island (1990) p. 86.

[97] U. Schnakenberg, W. Benecke, P. Lange, *TMAHW etchants for silicon micromachining*, Proceedings of the 6th International Conference on Solid-State Sensors and Actuators, Tech. Dig. Transducers 91, San Francisco (1991) p. 815.

[98] J. D. Hylton, R. Kinderman, A. R. Burgers, W. Sinke, P.M.M.C. Bressers, *Uniform Pyramid Formation on Alkaline-etched Polished Monocrystalline (100) Silicon Wafers*, Prog. Photovolt: Res. Appl. 4 (1996) p. 435.

[99] R. Barrio, N. González, J. Cárabe, J.J. Gandía, *Texturisation of Cz and FZ monocrystalline-silicon wafers for a-Si/c-Si heterojunction solar cells*, Proceedings of the 25th European Photovoltaic Solar Energy Conference, Valencia (2010) p.1621.

[100] G. Chen, I. Kashkoush, *Effect of Pre-Cleaning on Texturization of c-Si Wafers in a KOH/IPA Mixture*, 216th ECS Meeting, ECS Trans., 25, Vienna (2009) p. 3.

[101] U. Schnakenberg, W. Benecke, B. Löchel, *NH_4OH-based etchants for silicon micromachining*, Sens. Actuators, A 21-23 (1990) p.1031.

[102] E. Vazsonyi, K. De Clercq, R. Einhaus, E. Van Kerschaver, K. Said, J. Poortmans, J. Szlufcik, J. Nijs, *Improved anisotropic etching process for industrial texturing of silicon solar cells*, Sol. Energy Mater. Sol. Cells 57 (1999) p. 179.

[103] E. D. Palik, O.J. Glembocki, I. Heard, Jr., P. S. Burno, L.Tenerz, *Etching roughness for (100) silicon surfaces in aqueous KOH*, J. Appl. Phys. 70 (1991)

p. 3291.

[104] Y. K. Bhatnagar, A. Nathan, *On pyramidal protrusions in anisotropic etching of <100> silicon*, Sens. Actuators, A 36 (1993) p. 233.

[105] H. Schröder, E. Obermeier, A. Steckenborn, *Micropyramidal hillocks on KOH etched {100} silicon surfaces: formation, prevention and removal*, J. Micromech. Microeng. 9 (1999) p. 139.

[106] S.Tan, H. Han, R. Boudreau, M. L. Reed, *Process induced hillock defects on anisotropically etched silicon*, Proceedings of the IEEE Workshop on Micro Electro Mechanical Systems, Oiso (1994) p.229.

[107] M. Elwenspoek, *On the mechanism of anisotropic etching of silicon*, J. Electrochem. Soc. 140 (1993) p. 2075.

[108] A. Hein, O. Dorsch, E. Obermeier, *Effects of metallic impurities on anisotropic etching of silicon in aqueous KOH-solutions*, Proceedings of the 1997 International Conference on Solid-State Sensors and Actuators, Tech. Dig. Transducers 97, Chicago (1997) p. 687.

[109] K. P. Rola, I. Zubel, *Investigation of Si (h k l) surfaces etched in KOH solutions saturated with tertiary-butyl alcohol*, J. Micromech. Microeng. 21 (2011) 115026.

[110] E. van Veenendaal, K. Sato, M. Shikida, A. J. Nijdam, J. van Suchtelen, *Micro-morphology of single crystalline silicon surfaces during anisotropic wet chemical etching in KOH: velocity source forests*, Sens. Actuators, A 93 (2001) p. 232.

[111] M. A. Gosalvez, R.M. Nieminen, P. Kilpinen, E. Haimi, V. Lindroos, *Anisotropic wet chemical etching of crystalline silicon: atomistic Monte-Carlo simulations and experiments*, Appl. Surf. Sci. 178 (2001) p. 7.

[112] M. A. Gosálvez, R. M. Nieminen, *Surface morphology during anisotropic wet chemical etching of crystalline silicon*, New Journal of Physics 5 (2003) 100.1.

[113] A. J. Nijdam, *Anisotropic wet-chemical etching of silicon. Pits, peaks, principles, pyramids and particles*, PhD thesis, 2001, University of Twente.

[114] A. Cuevas, M. Stocks, D. Mcdonald, R. Sinton, *Applications of the quasi-steady-state photoconductance technique*, Proceedings of the 2nd World Conference on Photovoltaic Solar Energy Conversion, Vienna (1998) p. 1623.

[115] K. Watanabe, N. Matsuki, H. Fujiwara, *Ellipsometry characterization of hydrogenated amorphous silicon layers formed on textured crystalline silicon substrates*, Appl. Phys. Express 3 (2010) 116604.

[116] P. J. Cousins, J.E. Cotter, *Minimizing lifetime degradation associated with thermal oxidation of upright randomly textured silicon surfaces*, Sol. Energy Mater. Sol. Cells 90 (2006) p. 228.

[117] Y. W. Ok, A. Rohatgi, Y. H. Kil, S. E. Park, D. H. Kim, J. S. Lee, C. J. Choi, *Abnormal dopant distribution in $POCl_3$-diffused n^+ emitter of textured silicon solar cells*, IEEE Electron Device Lett. 32 (2011) p. 351.

[118] S. C. Baker-Finch, K. R. McIntosh, *The Contribution of Planes, Vertices, and Edges to Recombination at Pyramidally Textured Surfaces*, IEEE Journal of Photovoltaics, 1 (2011) p. 59.

[119] R. Turan, D. D. Perovic, D. C. Houghton, *Mapping electrically active dopant profiles by field-emission scanning electron microscopy*, Appl. Phys. Lett. 69 (1996) p. 1593.

[120] S. L. Elliott, R. F. Broom, C. J. Humphreys, *Dopant profiling with the scanning electron microscope - A study of Si*, J. Appl. Phys. 91 (2002) p. 9116.

[121] C. P. Sealy, M. R. Castell, P.R. Wilshaw, *Mechanism for secondary electron dopant contrast in the SEM*, J. Electron Microsc. 49 (2000) p. 311.

[122] C. Voyer, T. Buettner, R. Bock, D. Biro, R. Preu, *Microscopic homogeneity of emitters formed on textured silicon using in-line diffusion and phosphoric acid as the dopant source*, Sol. Energy Mater. Sol. Cells 93 (2009) p. 932.

[123] T. Mikio, K. Kunihiro, T. Sadaji, B. Toshiaki, S. Hitoshi, M. Masashi, U. Kenji, N. Noboru, K. Seiichi, O. Osamu, *HITTM cells—high-efficiency crystalline Si cells with novel structure*, Prog. Photovolt: Res. Appl. 8 (2000) p. 503.

[124] S. Dauwe, J. Schmidt, R. Hezel, *Very low surface recombination velocities on p- and n-type silicon wafers passivated with hydrogenated amorphous silicon films*, Proceedings of the 29th IEEE Photovoltaic Specialists Conference, New Orleans (2002) p. 1246.

[125] M. Taguchi, A. Terakawa, E. Maruyama, M. Tanaka, *Obtaining a Higher V_{oc} in HIT Cells*, Prog. Photovolt: Res. Appl. 13 (2005) p. 481.

[126] M. Python, O. Madani, D. Dominé, F. Meillaud, E. Vallat-Sauvain, C. Ballif, *Influence of the substrate geometrical parameters on microcrystalline silicon growth for thin-film solar cells*, Sol. Energy Mater. Sol. Cells 93 (2009) p. 1714.

[127] P. P. Altermatt, G. Heiser, A. G. Aberle, A. Wang, J. Zhao, S. J. Robinson, S. Bowden, M. A. Green, *Spatially Resolved Analysis and Minimization of Resistive Losses in High-eficiency Si Solar Cells*, Prog. Photovolt: Res. Appl. 4

(1996) p. 399.

[128] A. S. H. van der Heide, A. Schönecker, J. H. Bultman, W. C. Sinke, *Explanation of high solar cell diode factors by non-uniform contact resistance*, Prog. Photovolt: Res. Appl. 13 (2005) p. 3.

[129] J.M. Kim, Y.K. Kim, *The enhancement of homogeneity in the textured structure of silicon crystal by using ultrasonic wave in the caustic etching process*, Sol. Energy Mater. Sol. Cells 81 (2004) p. 239.

[130] C.-S. Jiang, Z. G. Li, H. R. Moutinho, L. Liang, A. Ionkin, M. M. Al-Jassim, *Real-space microscopic electrical imaging of n1-p junction beneath front-side Ag contact of multicrystalline Si solar cells*, J. Appl. Phys. 111 (2012) 083704.

[131] R. Hoenig, A. Kalio, J. Sigwarth, F. Clement, M. Glatthaar, J. Wilde, D. Biro, *Impact of screen printing silver paste components on the space charge region recombination losses of industrial silicon solar cells*, Sol. Energy Mater. Sol. Cells 106 (2012) p. 7.

List of symbols and abbreviations

A	Area
AFM	Atomic force microscopy
AM1.5G	Standard global solar spectrum with air mass coefficient of 1.5
ARC	Antireflection coating
CELLO	Solar cell local characterization
CFP	Conventional furnace process
Cz	Czochralski
DFM	Dynamic force mode
D_n	Electron diffusion coefficient
D_p	Hole diffusion coefficient
E_a	Activation energy
E_C	Edge energy of the conduction band
EDP	Ethylenediamine/pyrocatechol
E_F	Fermi energy
Eff	Efficiency
E_g	Gap energy
EQE	External quantum efficiency
E_V	Edge energy of the valence band
FE-SEM	Field emission scanning electron microscopy
FF	Fill factor
FZ	Float Zone
G	Generation rate
I	Electric current
I_{mp}	Current at maximum power
IPA	Isopropyl alcohol

IQE	Internal quantum efficiency
I_R	Light intensity of reference beam in the spectrometer
I_S	Light intensity of sample beam in the spectrometer
J	Current density
J_0	Dark current density
J_L	Photogenerated current density
J_n	Electron current density
J_p	Hole current density
J_r	Current density from recombination in space charge region
J_{sc}	Short circuit current density
k	Boltzmann constant, $8.617332 \cdot 10^{-4}$ eV/K
L_n	Electron diffusion length
L_p	Hole diffusion length
n	Electron concentration in the n-region
N_A	Acceptor concentration
N_C	Effective density of states in the conduction band
N_D	Donor concentration
n_i	Intrinsic carrier density
N_{ph}	Photon flux per unit area
N_V	Effective density of states in the valence band
OCP	Open circuit potential
p	Hole concentration in the p-region
P	Electrical power
P_i	Incident light power
PSG	Phosphorous silicate glass
q	Elementary charge
$QSSPC$	Quasi-steady-state photoconductance

R	Reflectance, resistance
r	Etching rate
R_g	Gas constant, 8.31442 J/K·mol
R_P	Parallel resistance
R_S	Series resistance
R_{Sh}	Sheet resistance
S	Surface recombination velocity
SE	Solar spectrum intensity, secondary electron (in chapter 7)
SEM	Scanning electron microscopy
STM	Scanning tunneling microscopy
SWR	Standard weighted reflection
T	Temperature
$TMAH$	Tetramethyl ammonium hydroxide
U	Recombination rate
U_S	Surface recombination rate
V	Voltage
V_D	Diffusion voltage
V_{mp}	Voltage at maximum power
V_{oc}	Open circuit voltage
W	Wafer thickness
w	Space charge region width
Δn	Excess electron density
Δn_S	Excess electron density at the surface
Δp	Excess hole density
ε	Electrical field
λ	Wavelength
$\mu W\text{-}PCD$	Microwave photoconductance decay

ρ Resistivity

τ Carrier lifetime

τ_{Auger} Auger lifetime

τ_{rad} Radiative lifetime

τ_{SRH} Shockley-Read-Hall lifetime

List of peer-reviewed publications

Publications included in this thesis

A. Montesdeoca-Santana, A. González Orive, A. Hernández Creus, B. González-Díaz, D. Borchert, R. Guerrero-Lemus*, Microscopic analysis of pyramids formation evolution with ultra-low concentrated* Na_2CO_3*/*$NaHCO_3$ *solution on (100) Si for solar cell application*, under revision in Microscopy and Microanalysis, 2012.

A. Montesdeoca-Santana, E. Jiménez-Rodríguez, B. González-Díaz, D. Borchert, R. Guerrero-Lemus, *Ultra-low concentration* Na_2CO_3*/*$NaHCO_3$ *solution for texturization of crystalline silicon solar cells*, Prog. Photovolt: Res. Appl. 20 (2012) p. 191.

A. Montesdeoca-Santana, J. Ziegler, S. Lindekugel, E. Jiménez-Rodríguez, S. Keipert-Colberg, S. Müller, C. Krause, D. Borchert, R. Guerrero-Lemus, *A comparative study on different textured surfaces passivated with amorphous silicon*, Phys. Status Solidi C 8 (2011) p. 747.

Publications not included in this thesis

J. Ziegler, A. Montesdeoca-Santana, D. Platt, S. Hohage, R. Guerrero-Lemus, D. Borchert, *Influences of p-and n-Doped Czochralski Base Material on the Performance of Silicon Based Heterojunction Solar Cells*, Jpn. J. Appl. Phys. 51 (2012) 10NA03.

A. Montesdeoca-Santana, B. González-Díaz, E. Jiménez-Rodríguez, J. Ziegler; J.J. Velázquez, S. Hohage, D. Borchert, R. Guerrero-Lemus, *Influence of stain etching on low minority carrier lifetime areas of multicrystalline silicon for solar cells*, Mater. Sci. Eng. B 176 (2011) p. 1541.

M. Rinio, A. Yodyunyong, S. Keipert-Colberg, D. Borchert, A. Montesdeoca-Santana, *Recombination in ingot cast silicon solar cells*, Phys. Status Solidi A 208 (2011) p. 760.

A. Montesdeoca-Santana, E. Jiménez-Rodríguez, B.González-Díaz, B. Díaz-Herrera, M. Rinio, D. Borchert, C. Hernández-Rodríguez, R. Guerrero-Lemus, *Phosphorous gettering in acidic textured multicrystalline solar cells*, Phys. Status Solidi C 8 (2011) p. 743.

B. Díaz-Herrera, E. Jiménez-Rodríguez, B. González-Díaz, A. Montesdeoca-Santana, J.J. Velázquez, R. Guerrero-Lemus, *Combined up conversion, down conversion and down shifting photo-luminescence of low cost erbium–ytterbium co-doped porous silicon produced by stain etching*, Thin Solid Films 519 (2011) p. 6110.

M. Rinio, A. Yodyunyong, S. Keipert-Colberg, Y. P. Botchak Mouafi, D. Borchert, A. Montesdeoca-Santana, *Improvement of multicrystalline silicon solar cells by a low temperature anneal after emitter diffusion*, Prog. Photovolt: Res. Appl. 19 (2011) p. 165.

R. Guerrero-Lemus, A. Montesdeoca-Santana, B. González-Díaz, B. Díaz-Herrera, J. J. Velázquez, C. Hernández-Rodríguez, E. Jiménez-Rodríguez, *Photoluminescence of monocrystalline and stain etched porous silicon doped with high temperature annealed europium*, J. Phys. D: Appl. Phys. 44 (2011) 335103.

A. Montesdeoca-Santana, E. Jiménez-Rodríguez, N. Marrero, B. González-Díaz, D. Borchert, R. Guerrero-Lemus, *XPS characterization of different thermal treatments in the ITO-Si interface of a carbonate-textured monocrystalline silicon solar cell*, Nucl. Instrum. Methods Phys. Res., Sect. B 268 (2010) p. 374.

Agradecimientos / Danksagung

Agradecimientos

La realización de la presente tesis ha sido posible gracias a la financiación del Programa de Formación de Personal Investigador del Ministerio de Ciencia e Innovación español, a través del proyecto ENE2007-60720/ALT; y del proyecto también dependiente de dicho Ministerio ENE-2010-14865/ALT.

Primeramente quisiera agradecer al Profesor Ricardo Guerrero Lemus, del grupo de Óptica de la Universidad de La Laguna, la oportunidad y la confianza que me ha ofrecido para trabajar en su grupo y realizar esta tesis, así como su apoyo y guía durante estos años.

Asimismo quisiera expresar al Dr. Dietmar Borchert mi gratitud por la acogida recibida en el centro que dirige, el Laboratory- and Servicecenter Gelsenkirchen del Fraunhofer Institute for Solar Energy Systems, en el que se ha realizado gran parte de los experimentos aquí presentados. Su hospitalidad, ayuda y consejo han sido fundamentales para el desarrollo de este trabajo.

Al Dr. Benjamín González y a Nuria Marrero, debo agradecerles el iniciarme a mi llegada al Grupo de Óptica de la Universidad de La Laguna en los secretos de la texturización de silicio. Y especialmente a Benjamín por haber estado siempre ahí para escucharme y aconsejarme.

De manera especial quiero agradecer a los compañeros con los que he trabajado durante los últimos años tanto en la Facultad de Física de la Universidad de La Laguna (ULL) como en el Laboratory- and Servicecenter Gelsenkirchen (LSC). A la Dra. Sinje Keipert-Colberg por su gran amistad y apoyo desde el primer día en que llegué a Gelsenkirchen y por tantas horas de oficina y laboratorio juntas. A mi amigo y compañero de doctorado Etaín Jiménez por su inestimable ayuda. No me puedo olvidar de mis compañeros del LSC, por hacer el día a día en el laboratorio más llevadero, por hacerme sentir como en casa, y sobre todo por los grandes esfuerzos que han hecho para que hoy día pueda pronunciar algunas palabras en su idioma: al Prof. Markus Rinio por tantos consejos y discusiones, a Martina Dörenthal por su ayuda con toda clase de papeles y burocracia en un idioma que me ha costado llegar a entender, a Petra Schäfer y Stefan Hohage por su ayuda y por el gran trabajo que realizan en el laboratorio, a Johannes Ziegler por su contribución en los experimentos sobre pasivación con silicio amorfo de esta tesis y por las divertidas discusiones en los descansos, y a Britt-Marie Meiners y Sven Holinski por su compañerismo. Y como no, a los estudiantes que han pasado por el laboratorio del LSC, especialmente a Christian Roters por su contribución a llevar a cabo parte de los trabajos de texturización, y a Patrick Botchak Mouafi por la realización de la metalización de las células aquí presentadas. También quisiera

agradecer a mis compañeros doctorandos de la planta sótano de la Facultad de Física de la ULL, por su amistad durante mis “estancias en Tenerife”, como dicen ellos: a Víctor, José, Carla, Leo, David, Sergio y Patricia. Y al Profesor Cecilio Hernández del grupo de Óptica, y a la empresa Dobon´s Technologies participante en el proyecto de investigación en el que se ha enmarcado este trabajo.

Esta tesis no hubiera sido posible sin el trabajo de los siguientes profesionales y compañeros que han colaborado de manera directa con la caracterización de los materiales estudiados: al Prof. Alberto Hernández y Alejandro González del Servicio de Microscopía de Fuerzas Atómicas de la ULL por las medidas AFM que han realizado con dedicación. A Juan Luis González del Servicio de Microscopía Electrónica de la ULL por tantas horas en el SEM y por su infinita paciencia y amabilidad. A Andreas Schütt y al grupo del Prof. Helmut Föll, Lehrstuhl für Allgemeine Materialwissenschaft de la Universidad Christian-Albrechts de Kiel, por las valiosas caracterización e interpretación CELLO de las células estudiadas y discusiones. A Jutta Zielonka del Fraunhofer ISE por las imágenes FE-SEM.

A mis amigos les agradezco el estar siempre ahí, aunque sea al otro lado del mail o el teléfono cuando estoy lejos.

Y por último, quisiera agradecer a mi familia, sin la que no hubiera podido llegar hasta aquí, por su apoyo y empuje en todo momento y por su compresión. A mis abuelos, mis padres, mi hermana y mi cuñado, y a Jan, por estar siempre a mi lado.

Danksagung

Die Erstellung dieser Arbeit wurde durch das Förderprogramm für Wissenschaftler über das Projekt ENE2007-60720/ALT sowie ENE-2010-14865/ALT des spanischen Ministerio de Ciencia e Innovación ermöglicht.

Bedanken möchte ich mich zuerst bei Prof. Ricardo Guerrero Lemus von der Arbeitsgruppe Optik der Universität La Laguna für die Möglichkeit und das Vertrauen, in seiner Gruppe arbeiten zu können, wie auch für seine Unterstützung und Hilfe während dieser Jahre.

Ich möchte Dr. Dietmar Borchert für die Aufnahme im von ihm geleiteten Labor- und Servicecenter Gelsenkirchen Fraunhofer ISE danken, wo ein Großteil der hier beschriebenen Experimente durchgeführt wurde. Seine Gastfreundschaft, seine Hilfe und sein Rat waren wesentlich für die Entwicklung dieser Arbeit.

Ich bedanke mich bei Dr. Benjamín González und Nuria Marrero für die Einführung in die Geheimnisse der Silizium-Texturierung während meiner Anfangszeit in der Arbeitsgruppe Optik der Universität La Laguna.

Im Besonderen möchte ich meinen Kollegen danken, mit denen ich in den letzten Jahren an der physikalischen Fakultät der Universität La Laguna (ULL) und am Labor- und Servicecenter Gelsenkirchen (LSC) zusammengearbeitet habe. Dr. Sinje Keipert-Colberg für ihre große Freundschaft und Unterstützung seit meinem ersten Tag in Gelsenkirchen, und für die vielen gemeinsamen Stunden in Büro und Labor. Meinem Doktorandenkollegen und Freund Etaín Jiménez für seine wertvolle Hilfe. Nicht zu vergessen meinen Kollegen vom LSC für die gute Arbeitsatmosphäre, dafür, dass sie mir das Gefühl gegeben haben, zu Hause zu sein und besonders für ihre Anstrengungen, sodass ich heute ein paar Worte in ihrer Sprache sprechen kann: Prof. Markus Rinio für so viele Diskussionen und Ratschläge, Martina Dörenthal für ihre Hilfe mit der Bürokratie in einer für mich schwierig zu verstehenden Sprache, Petra Schäfer und Stefan Hohage für ihre Hilfe und für die großartige Arbeit im Labor, Johannes Ziegler für seinen Beitrag zu den Experimenten zur amorphen Silizium-Passivierung in dieser Arbeit und die lustigen Diskussionen während der Pausen, und Britt-Marie Meiners und Sven Holinski für ihre Kameradschaft. Und natürlich den Studenten im LSC, insbesondere Christian Roters für seinen Beitrag bei der Texturierung und Patrick Botchak Mouafi für die Metallisierung der hier vorgestellten Zellen. Ich möchte mich auch bei meinen Doktorandenkollegen im Untergeschoss der physikalischen Fakultät der ULL für die schöne Zeit während meiner, wie sie sagen, „Gastaufenthalte“ in Teneriffa bedanken: Victor, José, Carla, Leo, David, Sergio und Patricia. Und bei Professor Cecilio Hernández von der Arbeitsgruppe Optik und der Firma Dobon Technologies, die an dem Forschungsprojekt teilnimmt, in dessen Rahmen diese Arbeit angefertigt wurde.

Diese Arbeit wäre nicht möglich gewesen ohne die Arbeit der Fachleute und Kollegen, die in direkter Weise an der Charakterisierung der hier untersuchten Materialien mitgewirkt haben. Mein Dank gilt Prof. Alberto Hernández und Alejandro González vom Rasterkraftmikroskopie-Service der ULL für die AFM Messungen, die sie mit Hingabe machten. Juan Luiz González vom Elektronenmikroskopie-Service der ULL für so viele Stunden am SEM und für seine unendliche Geduld und Liebenswürdigkeit. Andreas Schütt und der Arbeitsgruppe von Prof. Helmut Föll, Lehrstuhl für Allgemeine Materialwissenschaft der Christian-Albrechts-Universität zu Kiel, für die wertvolle CELLO Charakterisierung und Interpretation der untersuchten Zellen und für aufschlussreiche Diskussionen. Jutta Zielonka vom Fraunhofer ISE für die FE-SEM Bilder.

Meinen Freunden danke ich dafür, dass sie immer da sind, selbst wenn ich weit weg bin.

Zuletzt möchte ich meiner Familie danken, für ihre Unterstützung und Ermutigung zu jedem Zeitpunkt und für ihr Verständnis. Meinen Großeltern, meinen Eltern, meiner Schwester und meinem Schwager und Jan dafür, dass sie immer an meiner Seite sind.